DOT/FAA/AR-08/19

Air Traffic Organization
Operations Planning
Office of Aviation Research
and Development
Washington, DC 20591

Development and Validation of a Finite Element Simulation of a Vertical Drop Test of an ATR 42 Regional Transport Airplane

June 2008

Final Report

This document is available to the U.S. public through the National Technical Information Service (NTIS), Springfield, Virginia 22161.

U.S. Department of Transportation
Federal Aviation Administration

NOTICE

This document is disseminated under the sponsorship of the U.S. Department of Transportation in the interest of information exchange. The United States Government assumes no liability for the contents or use thereof. The United States Government does not endorse products or manufacturers. Trade or manufacturer's names appear herein solely because they are considered essential to the objective of this report. This document does not constitute FAA certification policy. Consult your local FAA aircraft certification office as to its use.

This report is available at the Federal Aviation Administration William J. Hughes Technical Center's Full-Text Technical Reports page: actlibrary.tc.faa.gov in Adobe Acrobat portable document format (PDF).

Technical Report Documentation Page

1. Report No.	2. Government Accession No.	3. Recipient's Catalog No.
DOT/FAA/AR-08/19		

4. Title and Subtitle	5. Report Date
DEVELOPMENT AND VALIDATION OF A FINITE ELEMENT SIMULATION OF A VERTICAL DROP TEST OF AN ATR 42 REGIONAL TRANSPORT AIRPLANE	June 2008
	6. Performing Organization Code
7. Author(s) Karen E. Jackson and Edwin L. Fasanella	8. Performing Organization Report No.
9. Performing Organization Name and Address Structural Dynamics Branch NASA Langley Research Center Hampton, VA 23681-2199	10. Work Unit No. (TRAIS)
	11. Contract or Grant No.
12. Sponsoring Agency Name and Address U.S. Department of Transportation Air Traffic Organization Operations Planning Federal Aviation Administration Office of Aviation Research and Development Washington, DC 20591	13. Type of Report and Period Covered Final Report
	14. Sponsoring Agency Code ANM-115

15. Supplementary Notes

The Federal Aviation Administration Airport and Aircraft Safety R&D Division COTR was Allan Abramowitz.

16. Abstract

This report documents a multiyear research project to develop a finite element model of a high-wing turboprop regional transport airplane, the ATR 42-300, to perform impact simulations using LS-DYNA®; to validate the simulations through correlation with test data obtained during a 30-feet per second (ft/sec) vertical drop test of the airplane; and to make modifications to the model to improve the level of correlation. A 30-ft/sec drop test of the ATR 42 airplane was performed on a concrete impact surface at the Federal Aviation Administration William J. Hughes Technical Center. The purpose of the test was to evaluate the structural response when subjected to a severe, but survivable, impact. The airplane was configured with crew and passenger seats, anthropomorphic test dummies, forward and aft luggage, instrumentation, and other ballast. The fuel tanks in the wing were filled with approximately 8700 pounds (lb) of water to represent the inertial properties of the fuel. The airplane weighed a total of 33,200 lb. The finite element model was developed from direct measurements of the airframe geometry. The seats, dummies, luggage, fuel, and other ballast were represented using concentrated masses. Comparisons were made of the structural deformation and failure of the airframe, as well as selected acceleration time history responses. Following the initial correlation studies, several modifications were made to improve the model including mesh refinement in areas that experience high loading, particularly the fuselage frames supporting the wing. For each of these modifications, test analysis correlations were performed to determine the influence on model accuracy.

17. Key Words	18. Distribution Statement
Crash simulation, High-wing regional transport airplane, Impact testing, Nonlinear finite element analysis	This document is available to the U.S. public through the National Technical Information Service (NTIS), Springfield, Virginia 22161.

19. Security Classif. (of this report)	20. Security Classif. (of this page)	21. No. of Pages	22. Price
Unclassified	Unclassified	81	

Form DOT F 1700.7 (8-72) Reproduction of completed page authorized

ACKNOWLEDGEMENTS

The authors acknowledge Gary Frings (retired), Allan Abramowitz, Tong Vu, and Tim Smith of the Federal Aviation Administration William J. Hughes Technical Center for their assistance with the model geometry development; for providing the test data, pre- and posttest photographs, and videos of the test; and for many helpful discussions and exchanges of information. We also recognize Allan Byars of Boeing Aircraft Company for many useful conversations regarding the modeling approach. We acknowledge the support of Alan Stockwell, Hasan Abu-Khajeel, and Peter Lively of Lockheed Martin Space Operations at the National Aeronautics and Space Administration (NASA) Langley Research Center for their assistance with model discretization and the NASA Structural Analysis. We acknowledge Sotiris Kellas, Nelson Seabolt, and George Palko for conducting the materials testing. Finally, we gratefully acknowledge Gabrielle Snyder for providing administrative support to keep our computers and LS-DYNA® up and running.

TABLE OF CONTENTS

			Page
EXECUTIVE SUMMARY			xiii
1.	INTRODUCTION		1
	1.1	Purpose	1
	1.2	Background	1
2.	EXPERIMENTAL PROGRAM		2
3.	MODEL DEVELOPMENT		6
4.	ORIGINAL MODEL: TEST ANALYSIS CORRELATION		9
	4.1	Comparison of Structural Deformation	9
	4.2	Comparison of Acceleration and Velocity Time History Response	11
	4.3	Comparison of Dog Bone Force Time History Responses	16
	4.4	Assessment of Test Analysis Correlation	17
5.	PARAMETRIC STUDY: VARYING FUEL LOADING		18
6.	MODIFIED ATR 42 MODEL		23
	6.1	Corrected Mesh Model	24
		6.1.1 Development of the Corrected Mesh Model	24
		6.1.2 Results of the Corrected Mesh Model	26
		6.1.3 Assessment of the Corrected Mesh Model	30
	6.2	Materials Testing	31
	6.3	Static and Dynamic Loads Analyses of the Wing Support Structure	33
		6.3.1 Development of a NASTRAN Model	33
		6.3.2 Results of the NASTRAN Static Loads Analysis	38
		6.3.3 Assessment of the NASTRAN Static Loads Analysis	43
		6.3.4 Development of an LS-DYNA Two-Frame Model	44
		6.3.5 Results of the Dynamic Load Analyses	45
		6.3.6 Parametric Study Using the LS-DYNA Two-Frame Model	50
		6.3.7 Assessment of the LS-DYNA Two-Frame Model	51
	6.4	Mesh Refinement Study	52
		6.4.1 Structural Deformation	54

6.4.2 Test and Analysis Correlation 57
6.4.3 Assessment of the Refined Mesh Model 62

7. DISCUSSION OF RESULTS 62

8. CONCLUSIONS 65

9. REFERENCES 67

LIST OF FIGURES

Figure		Page
1	Pretest Photograph of the ATR 42 Airplane, Raised to a Drop Height of 14 Feet	2
2	Floor Schematic	4
3	ATR 42 FS 25 and FS 27 Attachment Locations	5
4	ATR 42 Posttest Photograph Overall View	5
5	ATR 42 Posttest Photographs (a) Close-Up Exterior (b) Interior View	5
6	Geometry Model of the ATR 42 Airplane	6
7	Finite Element Model of the ATR 42 Airplane	8
8	Location of Point Elements in the Model	9
9	Structural Deformation of ATR 42 and Original LS-DYNA Model	10
10	Predicted Deformation at FS 25 and FS 27 at 0.00 and 0.25 sec	11
11	Time History Responses for the Left Outer Floor Track at FS 20	12
12	Time History Responses for the Right Outer Floor Track at FS 18	12
13	Time History Responses for the Right Side of the Cockpit Floor	13
14	Time History Responses for the Left Inner Floor Track at FS 29	13
15	Time History Responses for the Right Inner Floor Track at FS 35	14
16	Time History Responses for the Tail Section at FS 47	14
17	Time History Responses for the Left Sidewall at FS 18	15
18	Experimental and Analytical Time History Responses for the Ceiling at FS 26	16
19	Experimental and Predicted Dog Bone Force Time Histories	17
20	Wing Structural Deformations for Fuel-Loading Models	18
21	Deformation of FS 25 and FS 27 for Fuel-Loading Models	19
22	Displacement Time History Responses for Node 20931	20

23	Predicted Responses for the Left Outer Floor Track at FS 20 for Fuel-Loading Models	20
24	Predicted Responses for the Right Outer Floor Track at FS 18 for Fuel-Loading Models	21
25	Predicted Responses for the Left Inner Floor Track at FS 29 for Fuel-Loading Models	21
26	Predicted Responses for the Right Inner Floor Track at FS 35 for Fuel-Loading Models	22
27	Predicted Responses for the Ceiling at FS 26 for Fuel-Loading Models	22
28	Predicted Responses for the Tail at FS 47 for Fuel-Loading Models	23
29	Portion of a Finite Element Mesh Showing Several Nodal Discontinuities	24
30	Corrected Nodal Discontinuities	25
31	Picture of the Corrected Mesh Model	26
32	Acceleration and Velocity Responses at the Left Outer Floor Track at FS 20	27
33	Acceleration and Velocity Responses for the Right Outer Floor Track at FS 18	27
34	Acceleration and Velocity Responses for the Left Inner Floor Track at FS 29	28
35	Acceleration and Velocity Responses for the Right Inner Floor Track at FS 35	28
36	Acceleration and Velocity Responses for the Ceiling at FS 26	29
37	Acceleration and Velocity Responses for the Tail at FS 47	29
38	Triangular Elements in the Original and Corrected Mesh Models	30
39	Location of Potential Coupons to be Cut From Frame 25	31
40	Location of Potential Coupons to be Cut From the Web of Frame 25	31
41	Tensile Coupons Cut From Fuselage Frames 25 and 27	32
42	Tensile Test Setup	32
43	Stress Versus Strain Data for Aluminum Tensile Coupons	33
44	Front View of the Original Frame Model	34
45	Front View of the Refined Frame Model	35

46	Two-Frame Model Showing Attachments	36
47	Bracket and Fitting Attachment Method	36
48	Nodal Constraints in the Fore-Aft Direction	37
49	Predicted Force Responses for the Fuselage Frame at FS 25	38
50	Predicted Force Responses for the Fuselage Frame at FS 27	39
51	Initial Plasticity Locations in Upper Frames	40
52	Plastic Strain at the Point of Maximum Loading	40
53	Deformations and Plastic Strain in the Fuselage Frame for the Baseline Model	41
54	Progressive Deformations and Plastic Strains in the Fuselage Frame for the As-Tested Model	41
55	von Mises Stress Distribution of the Baseline Model at 2.0-in. Displacement	42
56	von Mises Stress Distribution of the As-Tested Model at 2.0-in. Displacement	43
57	Views of the LS-DYNA Two-Frame Model	44
58	LS-DYNA Two-Frame Model Showing the Locations of Nodal Constraints	45
59	Displacement Time History of a Node Located at the Bottom Center of the Upper Mass	46
60	Location of Initial Plasticity in the LS-DYNA Two-Frame Model	46
61	Fringe Plots of Effective Plastic Strain in the LS-DYNA Two-Frame Model	47
62	Model Picture and Predicted Contact Force Time Histories at FS 25 and FS 27	47
63	Total Vertical Force Responses of the Dog Bone and Frame Attachments at FS 25 and FS 27	48
64	Comparison of Plastic Strain at Equivalent Vertical Displacement	49
65	von Mises Stress Distributions in the NASTRAN and LS-DYNA Two-Frame Models	50
66	Results of the LS-DYNA Simulations at Three Impact Velocities	51
67	Refined Mesh Model of Fuselage Frames at FS 25, FS 26, and FS 27 With Attachments	53

68	Frame Attachments to the Bottom Skin of the Wing	53
69	Refined Mesh Model of the ATR 42 Airplane	54
70	Structural Deformation of ATR 42 and Refined Mesh LS-DYNA Model	55
71	Predicted Structural Deformation of the Original and Refined Mesh LS-DYNA Models	56
72	Test and Analysis Displacement Time History Responses of the Bottom Center of the Wing	57
73	Test Analysis Correlation Responses for the Left Outer Floor Track at FS 20	58
74	Test Analysis Correlation Responses for the Right Outer Floor Track at FS 18	58
75	Test Analysis Correlation Responses for the Right Side of the Cockpit Floor	59
76	Test Analysis Correlation Responses for the Left Inner Floor Track at FS 29	60
77	Test Analysis Correlation Responses for the Right Inner Floor Track at FS 35	60
78	Test Analysis Correlation Responses for the Center Tail Section at FS 47	61
79	Test Analysis Correlation Responses for the Left Sidewall at FS 18	61
80	Test Analysis Correlation Responses for the Bottom Center of the Wing at FS 26	62

LIST OF TABLES

Table		Page
1	Model Material Properties	7
2	Inertial Properties of Fuel-Loading Models	18
3	Comparison of the Original and Corrected Mesh Models With the ATR 42	26
4	Materials Characterization	33
5	Comparison of Inertial Properties	54
6	Percentage Difference in Test and Analysis Peak Acceleration	63

LIST OF ACRONYMS AND ABBREVIATIONS

Al	Aluminum
ATD	Anthropomorphic test dummy
CAD	Computer-aided design
CFC	Channel Filter Class
c.g.	Center of gravity
CPU	Central processing unit
FAA	Federal Aviation Administration
ft	Feet
ft/s	Feet per second
FS	Frame Station
FT	Floor track
g	Acceleration
HP	Hewlett Packard
Hz	Hertz
IAA	Inter-Agency Agreement
in.	Inch
in./sec	Inch-per-second
lb	Pound
NASA	National Aeronautics and Space Administration
NASTRAN	NAsa STtructural ANalysis
psi	Pounds per square inch
sec	Second
SMP	Shared memory processors
SPC	Single-point constraints
SPH	Smoothed Particle Hydrodynamic
Ti	Titanium

EXECUTIVE SUMMARY

This report describes a multiyear research project to develop and validate a numerical model of a vertical drop test of a regional transport airplane, the ATR 42-300. The objectives of the project were to develop a finite element model of the airplane, to execute the model to simulate a 30-foot per second (ft/sec) vertical drop test of the airplane, to perform an initial test analysis correlation, to conduct parametric assessments using the original model, and to evaluate model improvements such as incorporating updated material properties and performing a mesh refinement study. The simulations were executed using LS-DYNA®, a nonlinear explicit transient dynamic finite element code.

On July 30, 2003, the Federal Aviation Administration conducted a 30-ft/sec vertical drop test of the ATR 42-300 airplane. For the test, the airplane was configured with seats, anthropomorphic test dummies, mannequins, luggage in the forward and aft compartments, and 8700 pounds (lb) of water in the wings to represent the fuel loading. The total weight of the test article was 33,200 lb. A dominant feature of the airplane is the high wing, which is attached directly to two heavy fuselage frames at eight different locations, including four dog bone attachments. The airplane was instrumented with accelerometers, strain gages, load cells, pressure transducers, and string potentiometers. Of the channels available, eight were chosen for correlation with the model. During the test, the wing support frames failed allowing the wing to displace vertically into the fuselage cabin and to exhibit a forward (pitching) rotation.

The finite element model of the airplane contained 57,643 nodes and 62,979 elements, including 60,197 quadrilateral shell elements, 551 triangular shell elements, 526 beam elements, and 1,705 point elements. Material properties were obtained from material handbooks. An edge-constrained contact surface was added and an automatic contact definition was used. All nodes within the airplane model were assigned an initial velocity of 360 inches per second (in./sec) in the negative vertical direction. The initial analytical predictions correctly simulated the major damage mode seen during the test, which was the collapse and failure of the fuselage structure beneath the wing. These structural failures allowed the wing to displace vertically through the fuselage cabin. In general, a high level of agreement was obtained between the experimental and analytical data.

Following the initial model development and test analysis correlation, a parametric study was performed to evaluate the influence of varying fuel weight on the response of the heavy fuselage frames. Three cases were executed with full-fuel, half-fuel, and no-fuel loading. As expected, the full-fuel model exhibited the most deformation and damage of the fuselage frames, and the no-fuel model showed very little deformation and damage. Following the parametric study, a model improvement effort was initiated that included developing a corrected mesh model, incorporating experimentally determined material properties, performing static and dynamic loads analyses of the wing support structure, and conducting a mesh refinement study. Each model improvement was implemented separately, and comparisons were made with the original model and test. The mesh refinement study had the most influence on the level of correlation with accurate prediction of the maximum wing displacement.

1. INTRODUCTION.

1.1 PURPOSE.

This report describes the development of a full-scale finite element model of an ATR 42-300 regional transport airplane and validation of the model through test analysis correlation. The model was developed prior to the 30-foot per second (ft/sec) vertical drop test of the airplane; however, the initial test analysis correlations were performed posttest. Model validations, as described in this report, are necessary to gain confidence in the application of explicit transient dynamic finite element codes for crashworthy design and certification. In fact, the "validation of numerical simulations" was identified as one of five key technology shortfalls during the Workshop on Computational Methods for Crashworthiness that was held at the National Aeronautics and Space Administration (NASA) Langley Research Center in 1992 [1].

1.2 BACKGROUND.

In 1998, the U.S. Army Research Laboratory Vehicle Technology Directorate entered into an Inter-Agency Agreement (IAA) with the Federal Aviation Administration (FAA) William J. Hughes Technical Center, Atlantic City International Airport, New Jersey, for the purpose of validating crash simulations of airframe structures. As part of the IAA, finite element models were constructed of two 10-ft-long Boeing 737 fuselage sections, one outfitted with an auxiliary fuel tank mounted beneath the floor and the other with luggage filling the cargo hold and two different overhead stowage bins. Vertical drop tests of these two fuselage sections were performed at the FAA William J. Hughes Technical Center in 1999 and 2000, respectively [2 and 3]. These tests provided a valuable opportunity to evaluate the capabilities of computational tools for crash simulation through analytical and experimental correlation. Full-scale, three-dimensional finite element models of the B-737 fuselage sections were developed using MSC.Dytran® [4], a commercial explicit transient dynamic code, and simulations of the vertical drop tests were executed. The analytical predictions were successfully validated through extensive test analysis correlation, as documented in references 5 through 7.

In 2003, the IAA was extended for an additional 5 years and the model validation work entered a new phase with the development of a full-scale finite element model of the ATR 42-300 airplane. For this simulation, the model was developed using the preprocessing software package, MSC.Patran [8], and the model was executed using another commercial code, LS-DYNA® [9]. LS-DYNA is a general-purpose finite element code for analyzing the large deformation dynamic response of structures, including structures coupled with fluids. The main solution methodology is based on explicit time integration; however, an implicit solver is also available. A wide variety of contact definitions are available including self-contact, surface-to-surface contact, and node-to-surface contact. Spatial discretization is achieved by the use of eight-node solid elements, two-node beam elements, three- and four-node shell elements, truss elements, membrane elements, discrete elements, and rigid bodies. A variety of element formulations are available for each element type. Adaptive meshing is available for shell elements and is widely used in sheet metal stamping applications. LS-DYNA currently contains approximately 100 constitutive models and ten equations-of-state to cover a wide range of material behavior. Fluid-structure interaction problems are simulated using Arbitrary Lagrange-Euler coupling. Recently, a Smoothed Particle Hydrodynamic (SPH) method was added to provide additional hydrocode

capabilities. LS-DYNA is operational on a variety of computer systems, including mainframes, workstations, and personal computers, and can be executed using shared memory processors (SMP), or with multiple parallel processors. LS-DYNA has a large user base, especially in the area of automotive crashworthiness, and code enhancements and applications have been well funded over the past 10 years.

The FAA performed a 30-ft/sec vertical drop test of the ATR 42 airplane to determine the impact responses of the airframe, floor, floor tracks, seats, anthropomorphic test dummies (ATD), and high-wing fuel system. Current dynamic airplane seat certification criteria are based on empirical information obtained from prior airplane crash test data. The information did not include data that was representative of commuter-size airplanes. Consequently, this experiment was performed to supplement the existing basis for improved seat and restraint systems for commuter-category airplanes as defined in Title 14 of the Code of Federal Regulations Part 23. The experimental program, the model development process, the initial test analysis correlations, and the model modifications are presented in subsequent sections of this report.

2. EXPERIMENTAL PROGRAM.

On July 30, 2003, a 30-ft/sec vertical drop test of an ATR 42 airplane was conducted using the Dynamic Drop Test Facility located at the FAA William J. Hughes Technical Center. A pretest photograph of the test article, raised to the drop height of 14 feet (ft), is shown in figure 1. This twin-turboprop, high-wing, regional transport airplane was developed and manufactured through a joint effort by Aerospatiale in France and Aeritalia in Italy. The airplane has a wingspan of 81 ft, a seating capacity of between 42-50 passengers, a maximum cruise speed of 304 knots/hour, and a maximum gross takeoff weight of approximately 36,800 pounds (lb). The drop test was performed onto a concrete surface. The purpose of the test was to evaluate the dynamic structural response of the airplane when subjected to a severe, but survivable, impact. Particular attention was given to the seat and occupant responses.

Figure 1. Pretest Photograph of the ATR 42 Airplane, Raised to a Drop Height of 14 Feet

A schematic drawing of the floor of the airplane is shown in figure 2. The total weight of the airplane prior to the drop test was 33,200 lb. A large portion of the total weight was the 8700 lb of water added to the wing tanks to simulate fuel. In addition, 16 double-occupant airplane seats weighing 54 lb each and 3 single-occupant seats weighing 20 lb each were attached to floor tracks on the floor, as shown in figure 2. Seven ATDs and 16 mannequins, each weighing approximately 170 lb, were seated in various locations, as shown in figure 2. Ballast weights of 135 and 152 lb were added to some of the empty seats to represent the upper body mass of occupants. The forward and aft storage compartments were filled with 1450 and 739 lb of luggage, respectively. In addition to the ballast, two overhead stowage bins were mounted between Frame Station (FS) 30 and FS 34 on the right and left sides of the fuselage. The bins weighed 55 lb each (22-lb empty weight plus 33 lb of ballast in each bin). Two concentrated masses were added to the engine mounts on the wings, each weighing 1290 lb, to simulate the engines.

A dominant feature of this airplane is the high wing, which also serves as the roof of the cabin and is attached at eight locations to the heavy supporting fuselage frames at FS 25 and FS 27. The wing is secured in the interior of the fuselage by an attachment bracket located on each end of frames FS 25 and FS 27 (four locations) and a corresponding bracket on the wing. Outside the fuselage, a beam (hereafter known as a dog bone) was used to attach a mounting bracket on the wing to a corresponding bracket attached to one of four exterior locations on the left or right side of FS 25 or FS 27, approximately 60 inches (in.) above the floor. See figure 3 for corresponding attachment locations. The measured longitudinal position of the center of gravity (c.g.) of the fully loaded airplane is approximately half way between FS 25 and FS 26, as shown in figure 2. This measurement falls within the c.g. envelope specified by the airframe manufacturer, as indicated in the Weight and Balance Manual [10]. A complete description of the test article and experimental data obtained during the 30-ft/sec vertical drop test of the ATR 42 airplane can be found in reference 11.

The fuselage section was instrumented with accelerometers, strain gages, load cells, pressure transducers, and string potentiometers. Test data were collected at 10,000 samples per second using two data acquisition systems, one onboard and one external to the airplane. Of the channels available, eight acceleration responses were selected for correlation with the model. Of these eight responses, five were from accelerometers mounted on the floor of the fuselage cabin at locations shown in figure 2. In addition, accelerometers located in the tail section at FS 47, the left sidewall at FS 18, and the center of the bottom skin of the wing (ceiling) at FS 26 were also selected for comparison. These locations are not shown in figure 2.

A posttest photograph showing an overall exterior view of the airplane is shown in figure 4. The dominant damage mode to the airframe was the failure of the heavy fuselage frames located at FS 25 and FS 27. These frames supported the wing and their failure resulted in the wing displacing into the fuselage cabin. The aluminum structure that supported the wing was crushed and fractured. A posttest photograph showing a closer view of the wing and fuselage region is shown in figure 5(a). Further inspection of the airframe following the test indicated that the floor buckled and several of the seats failed, as shown in figure 5(b).

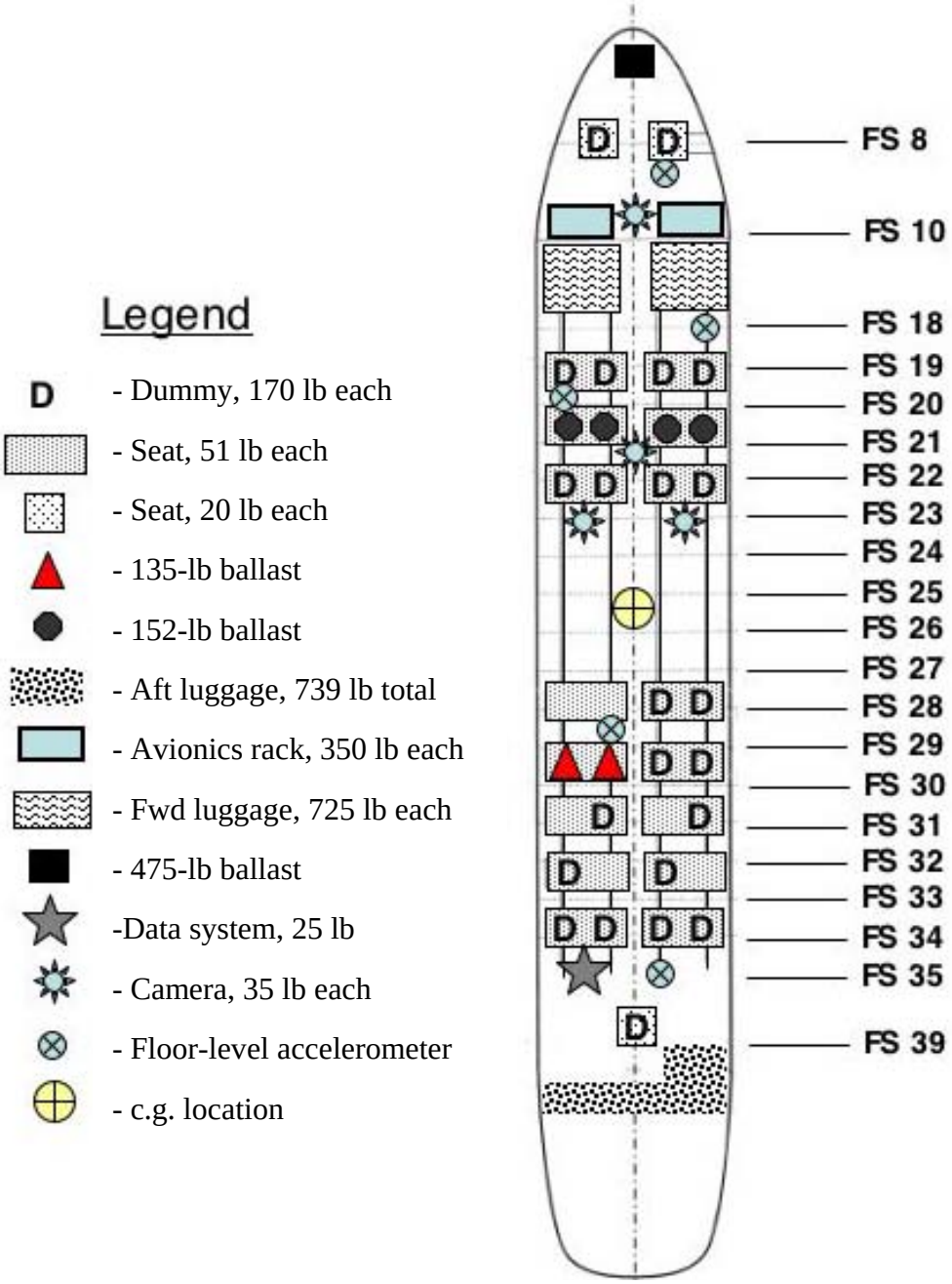

Figure 2. Floor Schematic

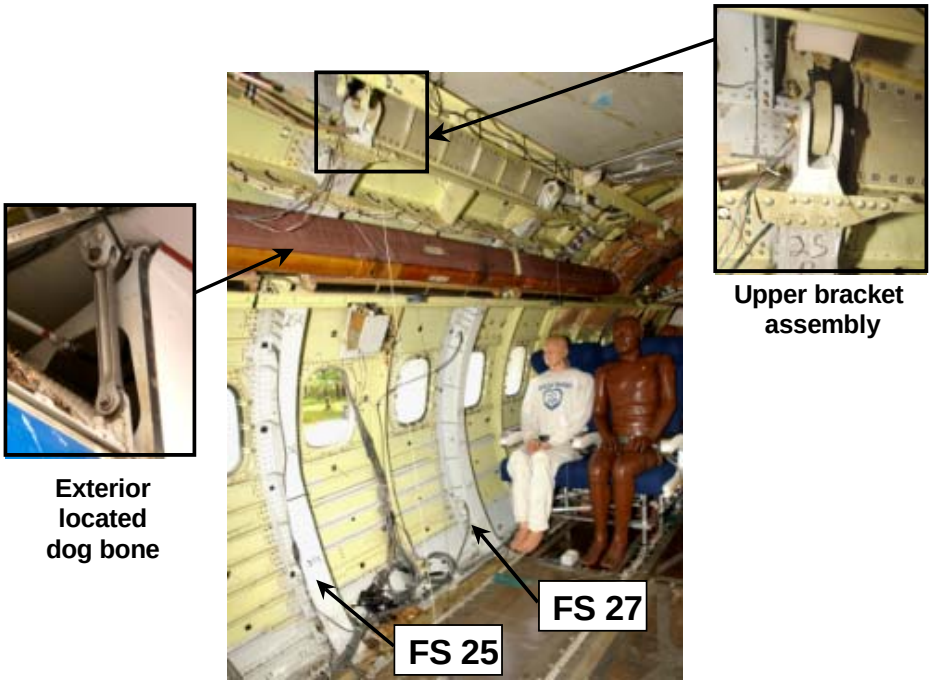

Figure 3. ATR 42 FS 25 and FS 27 Attachment Locations

Figure 4. ATR 42 Posttest Photograph Overall View

(a)

(b)

Figure 5. ATR 42 Posttest Photographs (a) Close-Up Exterior (b) Interior View

3. MODEL DEVELOPMENT.

The finite element model of the ATR 42 airplane was developed from geometric data gathered from direct measurements of the airplane, which were input into MSC.Patran database files. The geometric data were received from the FAA in six installments, each containing increasingly more detailed information about the shape and dimensions of the airframe. As each file was received, the new information was input into a master geometry file of the entire airplane. The final geometry model of the airplane, shown in figure 6, consisted of 25,917 points, 17,270 curves, and 17,768 surfaces. The geometry model was discretized into a finite element mesh, element and material properties were assigned, contact and initial velocity conditions were defined, and the model was executed to generate analytical predictions of structural deformation and acceleration time history responses. Additional information on the model development process can be found in reference 12.

The finite element model of the ATR 42 airplane, shown in figure 7, contained 57,643 nodes and 62,979 elements including 60,197 quadrilateral shell elements, 551 triangular shell elements, 526 beam elements, and 1,705 point elements.

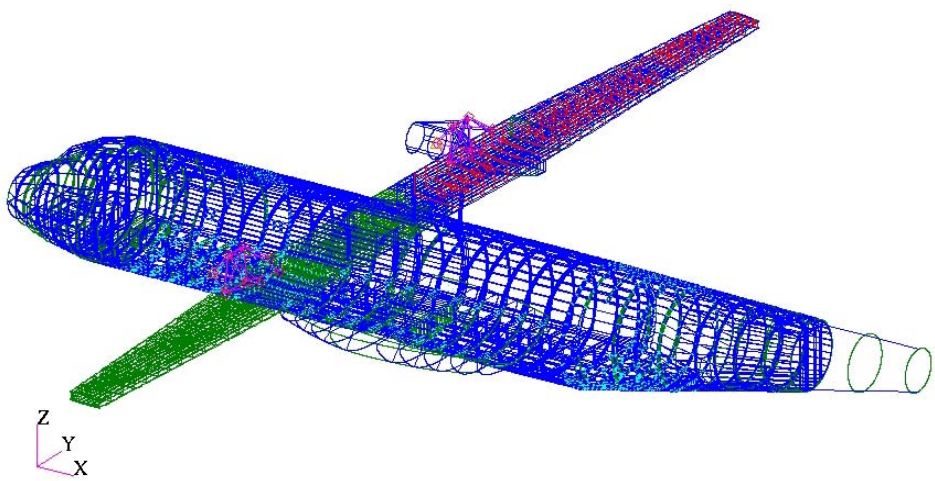

Figure 6. Geometry Model of the ATR 42 Airplane

An automatic contact (*CONTACT_AUTOMATIC_SINGLE_SURFACE) was specified for the model, which is a generic contact definition in LS-DYNA that prescribes that no node can penetrate through any surface in the model. An impact surface was created to represent the concrete pad beneath the drop tower. This surface was modeled as a 5-in.-thick aluminum (Al) plate, encompassing the total length and width of the airplane, as shown in figure 7. Four main material properties were defined in the model for Al-2024-T3, Al-7075-T6, Al-7050-T7452, and titanium (Ti) Ti-6Al-4V. The properties were defined using the MAT_PLASTIC_KINEMATIC card in LS-DYNA for a linear elastic-plastic material with input values for density, Poisson's ratio, Young's modulus, yield stress, hardening modulus, and an ultimate failure strain. The specific properties used in the model are shown in table 1. Most sheet metal parts, such as the outer skin, were assigned material properties of Al-2024-T3. The forged-metal parts (such as the fuselage frames, floor beams, and floor tracks) were assigned material properties of Al-7075-T6, except for the two heavy fuselage frames at FS 25 and FS 27 which were assigned properties of Al-7050-T7452. The dog bones used to attach the wing to the fuselage frames at FS 25 and

FS 27, were assigned material properties of titanium. The material property designation and mass of each component were obtained from the airplane manufacturer's Weight and Balance Manual [10] and the material property values were obtained from Military Handbook-5H [13].

The pictures of the model, shown in figure 7, were output from LS-PRE/POST [14], the pre- and postprocessing software package for LS-DYNA. A figure depicting the location of the point elements is shown in figure 8. Point elements were used to assign concentrated masses, representing the seats, occupants, luggage, fuel, engines, and other ballast, to nodes in the model. The mass of the fuel loading was distributed over the nodes forming the lower skin of the wing. The distribution was determined based on the amount of fuel supported by each element on the bottom skin of the wing.

All nodes in the airplane model were given an initial velocity of -360 in./sec (-30 ft/sec). For the impact surface, all edge nodes were fixed, i.e., constrained from translational and rotational motion. In addition, the nodes of the elements forming the wing attachment hardware, including the dog bones, were constrained to move in the vertical (z) direction only. These constraints were applied to ensure proper load transfer from the wing into the fuselage frames. The model was executed in LS-DYNA (version 970) for 0.25 second (sec) of simulation time, which required 130 hours of central processing unit (CPU) on a single processor Hewlett Packard (HP) workstation x4000. The initial time step was 6.54e-5 sec and the end time step was 6.83e-7 sec.

Table 1. Model Material Properties

Material	Young's Modulus (psi)	Poisson Ratio	Density (lb-sec^2/in.^{4})	Yield Stress (ksi)	Hardening Modulus (ksi)	Failure Strain (%)
Al-2024-T3	9.62e06	0.33	2.59e-4	35.25	119.9	14.63
Al-7075-T6	1.03e07	0.33	2.61e-4	52.22	145.3	4.49
Al-7050-T7452	1.04e07	0.33	2.64e-4	60.0	145.3	4.0
Ti-6Al-4V	1.71e07	0.31	4.24e-4	125.0	203.0	8.0

ksi = Thousand pounds per square in.
psi = Pounds per square in.

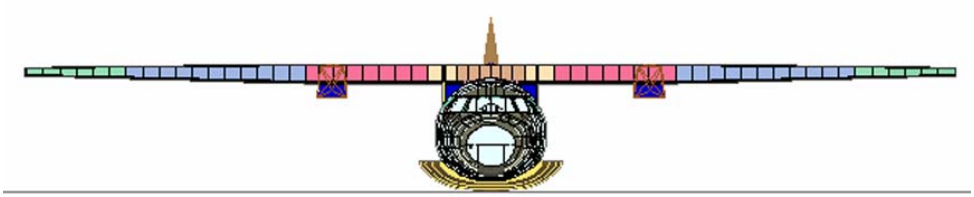

(a) Front view

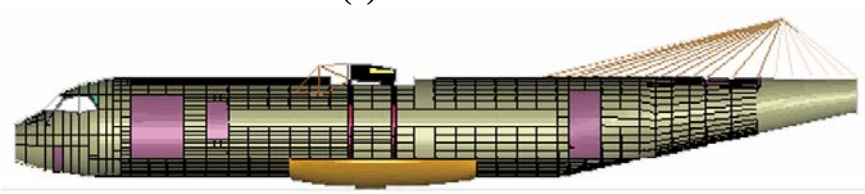

(b) Side view

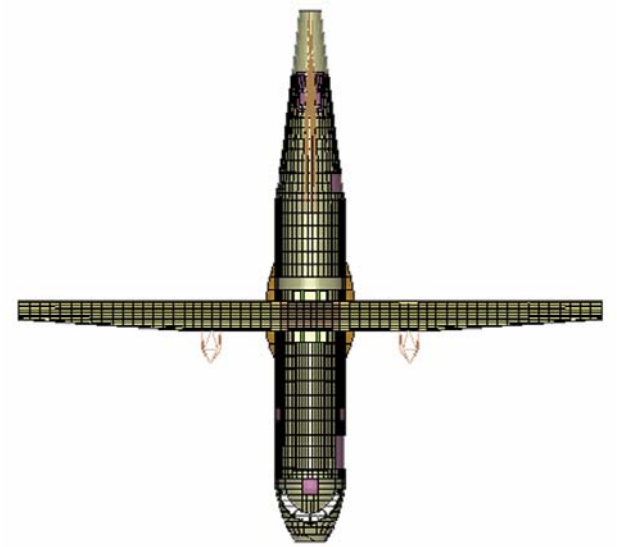

(c) Top view

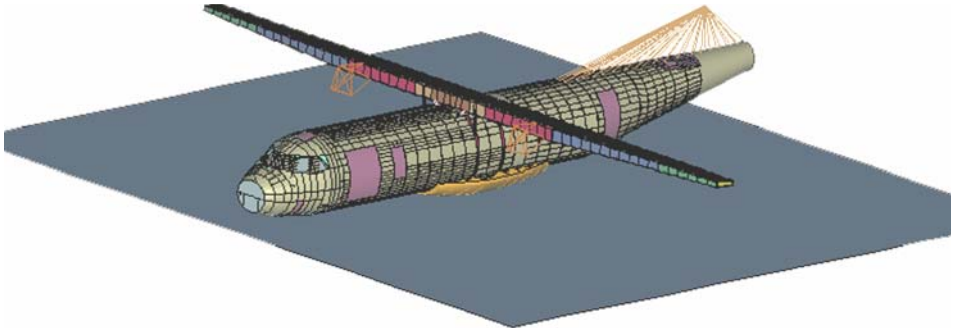

(d) Three-quarter view

Figure 7. Finite Element Model of the ATR 42 Airplane

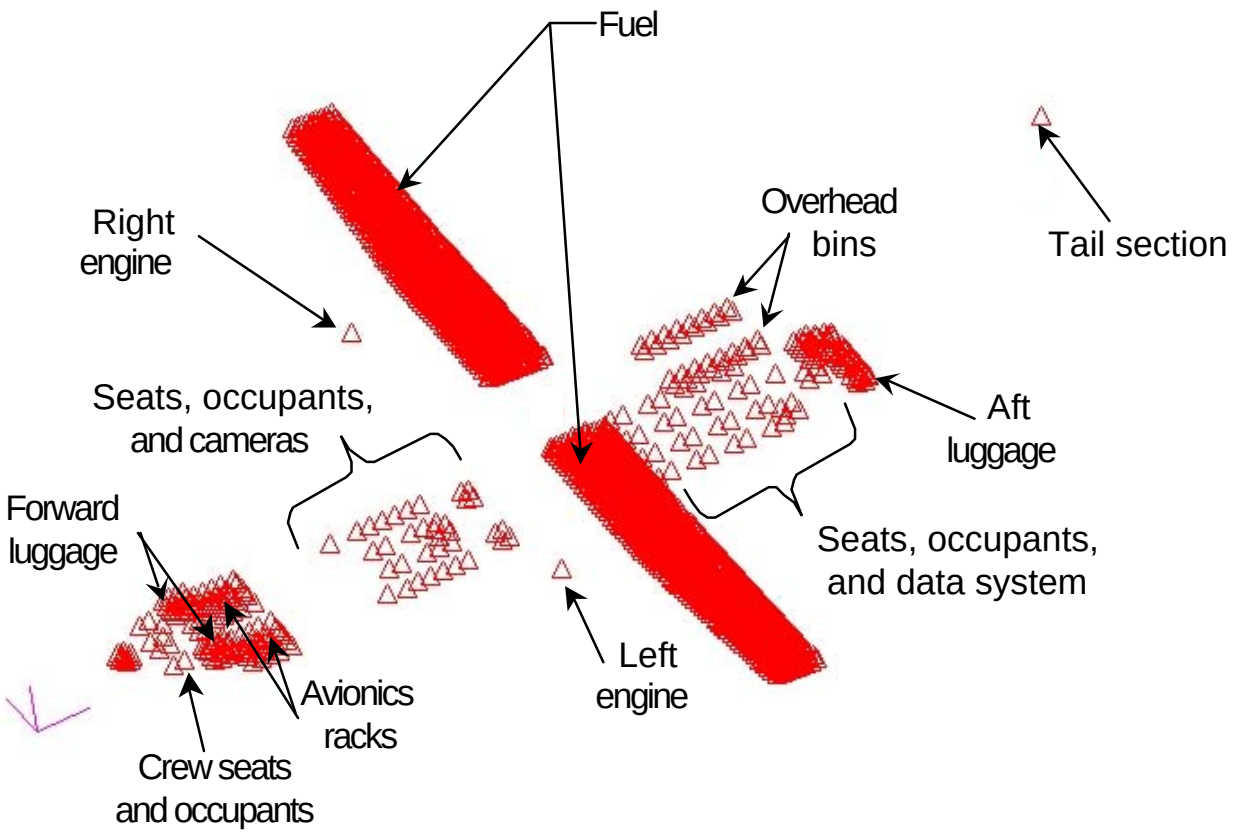

Figure 8. Location of Point Elements in the Model

As a quality check on the model, the total weight and longitudinal c.g. location of the model were compared with those of the test article. The weight of the airplane was 33,200 lb, and the total weight of the airplane model was 33,120 lb, just 80 lb lighter than the test article. The measured longitudinal c.g. position of the test article was 469.2 in. from the reference location. For the model, the longitudinal c.g. position was 471.5 in. from the reference location and within 3 in. of the experimental value.

4. ORIGINAL MODEL: TEST ANALYSIS CORRELATION.

Correlations between analytical predictions generated by the LS-DYNA simulation of the original model and the experimental data consist of comparisons of structural deformation and selected acceleration and velocity time history responses.

4.1 COMPARISON OF STRUCTURAL DEFORMATION.

Comparisons of test article and model deformations from 0.05 to 0.25 sec in 0.05-sec intervals are shown in figure 9. The pictures of model deformation were obtained from the postprocessing file, and the experimental pictures were captured from high-speed film. In general, the original model accurately predicts the structural deformation and failure behavior of the test article, including the collapse and failure of the fuselage frames beneath the wing. In the experiment, structural failure was initiated by fracture of the fuselage frames at FS 25 and FS 27 and is not

caused by failure of the dog bones. The same failure behavior is observed in the model, as shown in figure 10. This figure shows the predicted deformation of the fuselage frames at FS 25 and FS 27, along with the dog bones and the wing attachments, at the beginning and end of the simulation. In the model, the frames are highly deformed and fractured, and the dog bones remain intact. Note that in LS-DYNA, failed elements are removed from the model. The frame failures allow the wing to translate downward through the fuselage cabin. In addition to the vertical translation, the wing tips in the model also exhibit significant vertical deflection due to elastic bending of the wing. In the test, some oscillatory bending of the wing was observed; however, the tip displacement was considerably less than in the model. The actual wing also exhibited a forward (pitching) rotation immediately following impact, due to the forward placement of the simulated engines. However, the model does not capture this behavior, partially because the nodes in the elements used to attach the wing to the heavy fuselage frames were constrained to move vertically only.

Time (sec)	Test Article	LS-DYNA Simulation
0.05		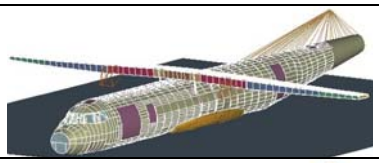
0.10		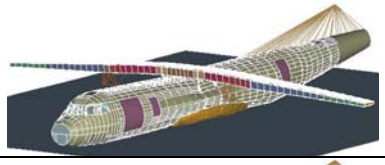
0.15		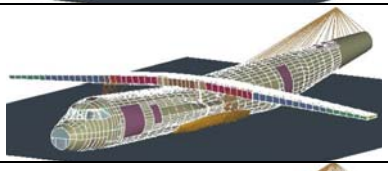
0.20		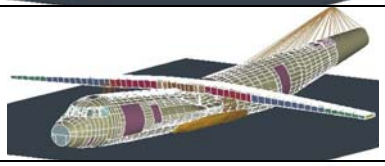
0.25		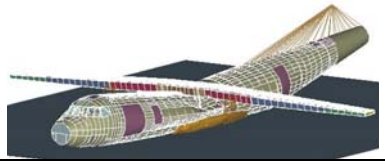

Figure 9. Structural Deformation of ATR 42 and Original LS-DYNA Model

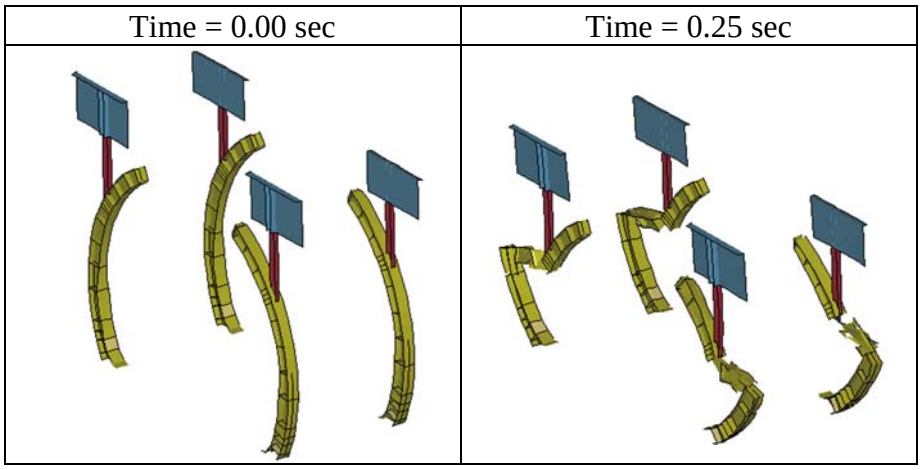

Figure 10. Predicted Deformation at FS 25 and FS 27 at 0.00 and 0.25 sec

4.2 COMPARISON OF ACCELERATION AND VELOCITY TIME HISTORY RESPONSE.

The raw experimental acceleration data were plotted versus time, integrated to obtain the velocity time history responses, and filtered using a low-pass digital filter based on the SAE J211/1 specifications [15]. A variety of cut-off frequencies were applied in an attempt to obtain a well-defined acceleration pulse, while at the same time not distorting the integrated velocity response. Distortion in the velocity response is determined by comparing the velocity time histories obtained by integrating the raw and filtered experimental acceleration data. A low-pass, cut-off frequency of 33.2 (hertz) Hz was selected because it generally met these criteria. This filter is equivalent to a Channel Filter Class (CFC) 20 filter [15]. All experimental and analytical acceleration time histories shown in this report are filtered using this cut-off frequency. Also, since minimal distortion was evident, the experimental and analytical velocity responses shown in this report were obtained by integrating the filtered acceleration data.

The experimental and analytical acceleration and velocity responses of the left outer floor track at FS 20 are shown in figure 11. For the test, the acceleration response exhibits two main peaks, as indicated in figure 11(a). The first acceleration peak (18 g) is smaller in magnitude than the second (28 g). At this location, the predicted acceleration response also exhibits two peaks; however, the first peak is higher in magnitude (28 g) than the second (17 g). The filtered experimental and analytical acceleration data were integrated to obtain the velocity responses plotted in figure 11(b). Both curves are closely matched up to 0.06 sec. After that time, the analytical velocity response crosses zero velocity at 0.075 sec and exhibits a rebound of about 34 in./sec. The experimental response flattens out after 0.06 sec and does not cross zero until 0.15 sec. The maximum rebound velocity exhibited by the experimental response is 30 in./sec.

The experimental and analytical acceleration and velocity responses of the right outer floor track at FS 18 are shown in figure 12. For this location, the peak acceleration values for the test and analysis are of the same magnitude, about 24 g. Also, the predicted velocity response closely matches the experimental response, i.e., both curves cross zero velocity at the same time (0.08 sec), though the experimental response exhibits a slightly higher rebound velocity of 50 in./sec.

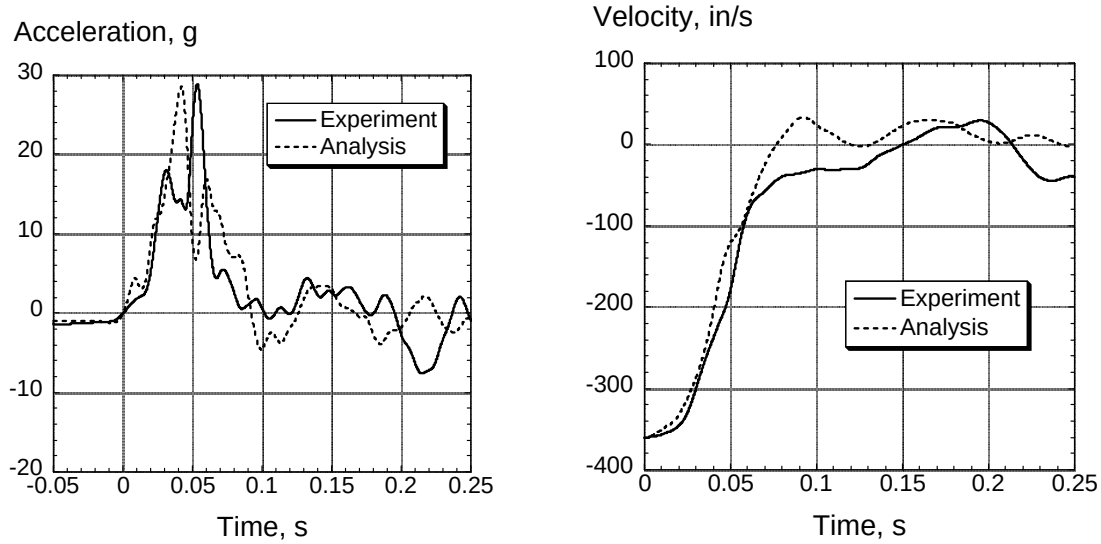

(a) Acceleration responses (b) Velocity responses

Figure 11. Time History Responses for the Left Outer Floor Track at FS 20

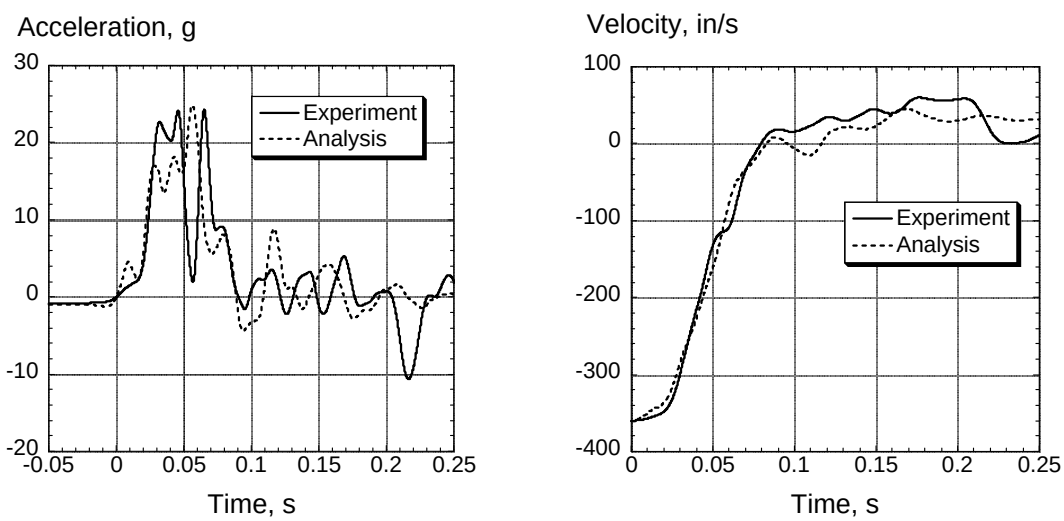

(a) Acceleration responses (b) Velocity responses

Figure 12. Time History Responses for the Right Outer Floor Track at FS 18

Next, the experimental and analytical acceleration and velocity responses of the right side of the cockpit floor are shown in figure 13. Again, the experimental acceleration response exhibits two peaks; however, in this case, the first peak (34 g) is higher in magnitude than the second (28 g). The predicted peak acceleration is 26 g. The experimental pulse is shorter in duration than the analytical response by about 0.02 sec, as indicated in the velocity plot of figure 13(b). However, both curves exhibit the same rebound velocity of 90 in./sec.

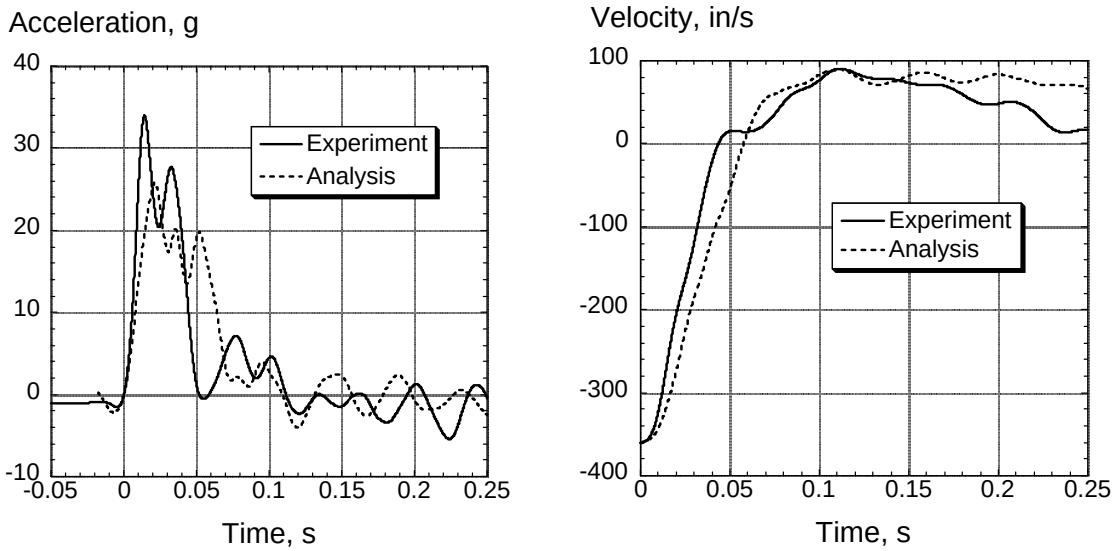

(a) Acceleration responses (b) Velocity responses

Figure 13. Time History Responses for the Right Side of the Cockpit Floor

The experimental and analytical acceleration and velocity responses of the left inner floor track at FS 29 and the right inner floor track at FS 35 are plotted in figures 14 and 15, respectively. The locations of these accelerometers are shown in figure 2. The accelerometer at FS 29 was located on the floor slightly to the rear of the fuselage frames supporting the wings, and the accelerometer at FS 35 was located on the floor at the very rear of the airplane. At these two locations, the filtered experimental acceleration responses exhibit high-amplitude, low-frequency responses, making it difficult to discern a well-defined acceleration pulse. In general, the predicted acceleration responses match the peak values and the pulse durations of the experimental acceleration responses at these two locations. The comparison of the velocity responses also indicates a high level of correlation, as shown in figures 14(b) and 15(b).

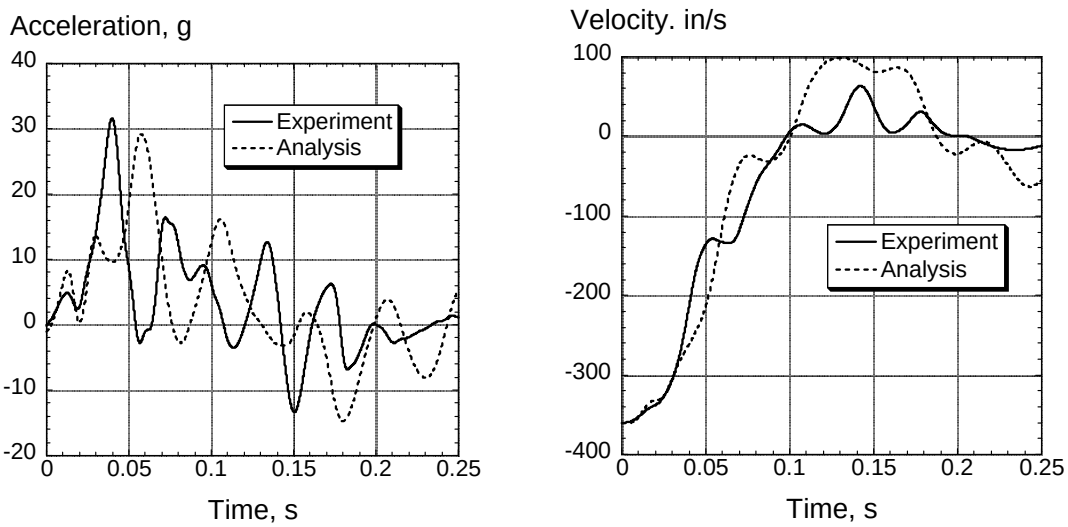

(a) Acceleration responses (b) Velocity responses

Figure 14. Time History Responses for the Left Inner Floor Track at FS 29

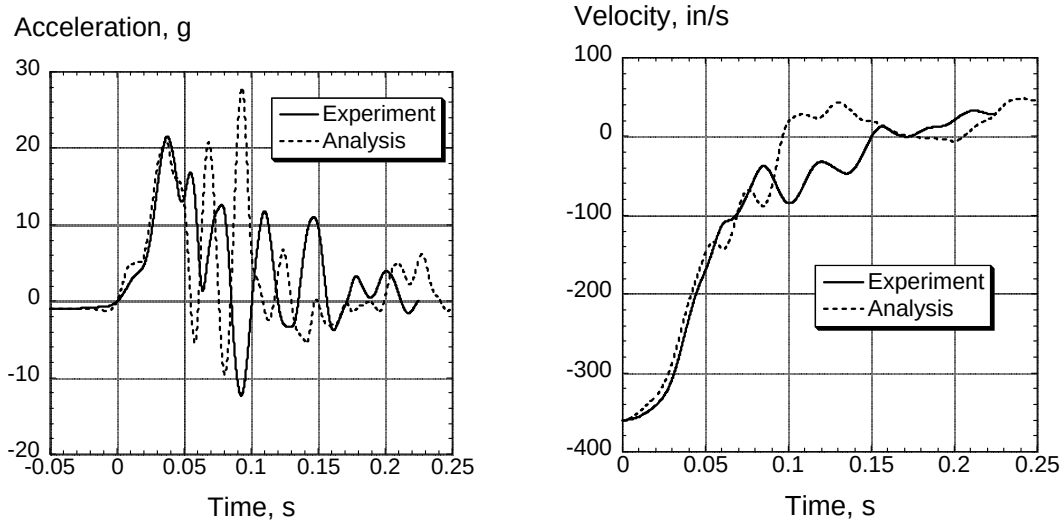

(a) Acceleration responses (b) Velocity responses

Figure 15. Time History Responses for the Right Inner Floor Track at FS 35

The experimental and predicted acceleration and velocity responses of the center of the tail section at FS 47 are plotted in figure 16. Unlike the floor acceleration responses, most of which had pulse durations of 0.1 sec or less, this acceleration response is 0.2 sec in duration. Both the experimental and analytical acceleration responses, shown in figure 16(a), exhibit a single pulse of approximately the same duration and magnitude. The experimental and analytical velocity responses, shown in figure 16(b), show nearly perfect agreement with both curves crossing zero velocity at nearly the same time (0.16 sec) and exhibiting a maximum rebound velocity of 147 in./sec at 0.21 sec.

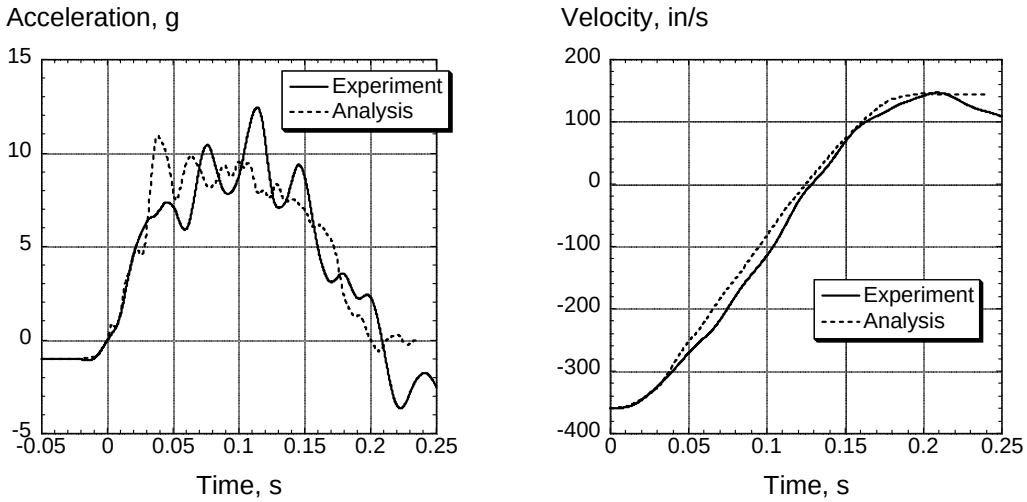

(a) Acceleration responses (b) Velocity responses

Figure 16. Time History Responses for the Tail Section at FS 47

The experimental and analytical acceleration and velocity responses of the left sidewall at FS 18 are plotted in figure 17. This accelerometer was located on the sidewall, approximately 12 in.

above the floor and was oriented in the vertical direction. The analytical acceleration response closely matches the magnitude of the test (peak acceleration of 26.5 g's for the analysis compared with 22.5 g's for the experiment). The velocity responses, shown in figure 17(b), are close to 0.075 sec, after which time the analytical curve crosses zero velocity at 0.08 sec and exhibits a maximum rebound velocity of 36 in./sec. However, the experimental response flattens out and does not cross zero velocity until 0.12 sec, after which it exhibits a prolonged rebound velocity of 60 in./sec, not seen in the analytical curve.

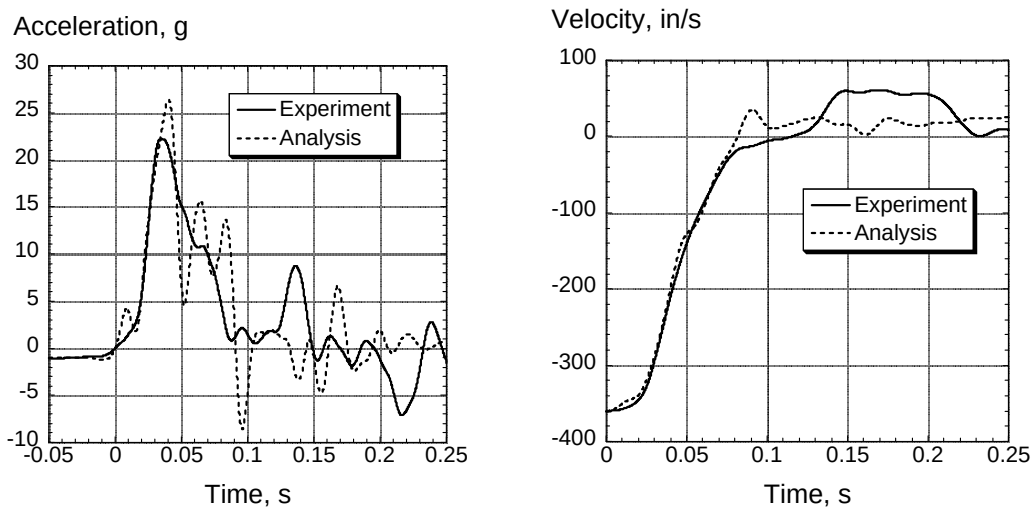

(a) Acceleration responses (b) Velocity responses

Figure 17. Time History Responses for the Left Sidewall at FS 18

The final time history comparison is shown in figure 18, in which the experimental and analytical acceleration and velocity responses for the ceiling at FS 26 are plotted. The filtered experimental and analytical acceleration data contain high-amplitude, low-frequency responses, as shown in figure 18(a). The predicted acceleration response overshoots the magnitude of the initial peak acceleration of the experimental response; however, it accurately captures the dip and subsequent rise in the experimental response that occurs at approximately 0.1 sec. At this accelerometer location, the analytical response appears to be reducing velocity more quickly than the experiment, as shown in figure 18(b). For example, at 0.04 sec, the experimental velocity is -289 in./sec, while the predicted velocity is -204 in./sec. Also, note that neither response has crossed zero velocity by 0.25 sec, indicating that the wing is still translating downward at the end of the simulation.

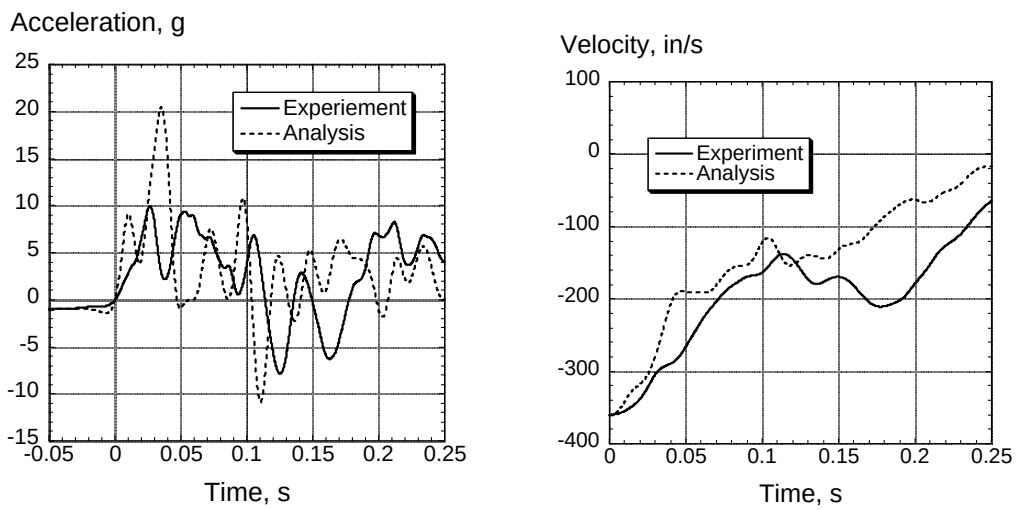

(a) Acceleration responses (b) Velocity responses

Figure 18. Experimental and Analytical Time History Responses for the Ceiling at FS 26

4.3 COMPARISON OF DOG BONE FORCE TIME HISTORY RESPONSES.

The dog bones were instrumented to measure axial load during the impact test. Analytical predictions of dog bone forces were generated for correlation with this data using the postprocessing software package LS-PRE/POST [14]. In the original model, all four dog bones were assigned to a single part definition. Using LS-PRE/POST, the dog bone part was posted and the S-plane feature was used to define a cutting plane at the lowest axial position. Since all four dog bones were posted, a total reaction force was generated using this method. For correlation with specific dog bone data, the total force was divided by four. It should be noted that this method provides only as many data points as there are d3plot files available; however, it is a quick and easy method for obtaining reaction forces.

The comparison of experimental and analytical force time histories for each of the four dog bones is shown in figure 19. Note that the analytical curves are identical for each dog bone, since the method used to generate the data was to divide the combined total force by four. Thus, the analytical curves in each plot represent the average force. Also, note that the analytical data show a sudden drop to zero force at approximately 0.125 sec. This drop is an artifact of the method used to generate the analytical force data and represents that the dog bones have passed completely through the cutting plane.

The level of agreement is quite remarkable, especially when considering the relatively simplistic method used to generate the analytical data. The left and right front dog bones exhibit a peak force of approximately 45,000 lb, as shown in figure 19(a) and (b), respectively. The analytical curves match both the magnitude and timing of the peak force. Note that the experimental responses of the left front and rear dog bones exhibit some signal anomalies. The peak forces for the rear dog bone specimens are lower than the front dog bone peak forces, as shown in figure 19(c) and (d), respectively. Actually, the peak force response of the right rear dog bone (20,000 lb) is significantly lower than the other three peak forces.

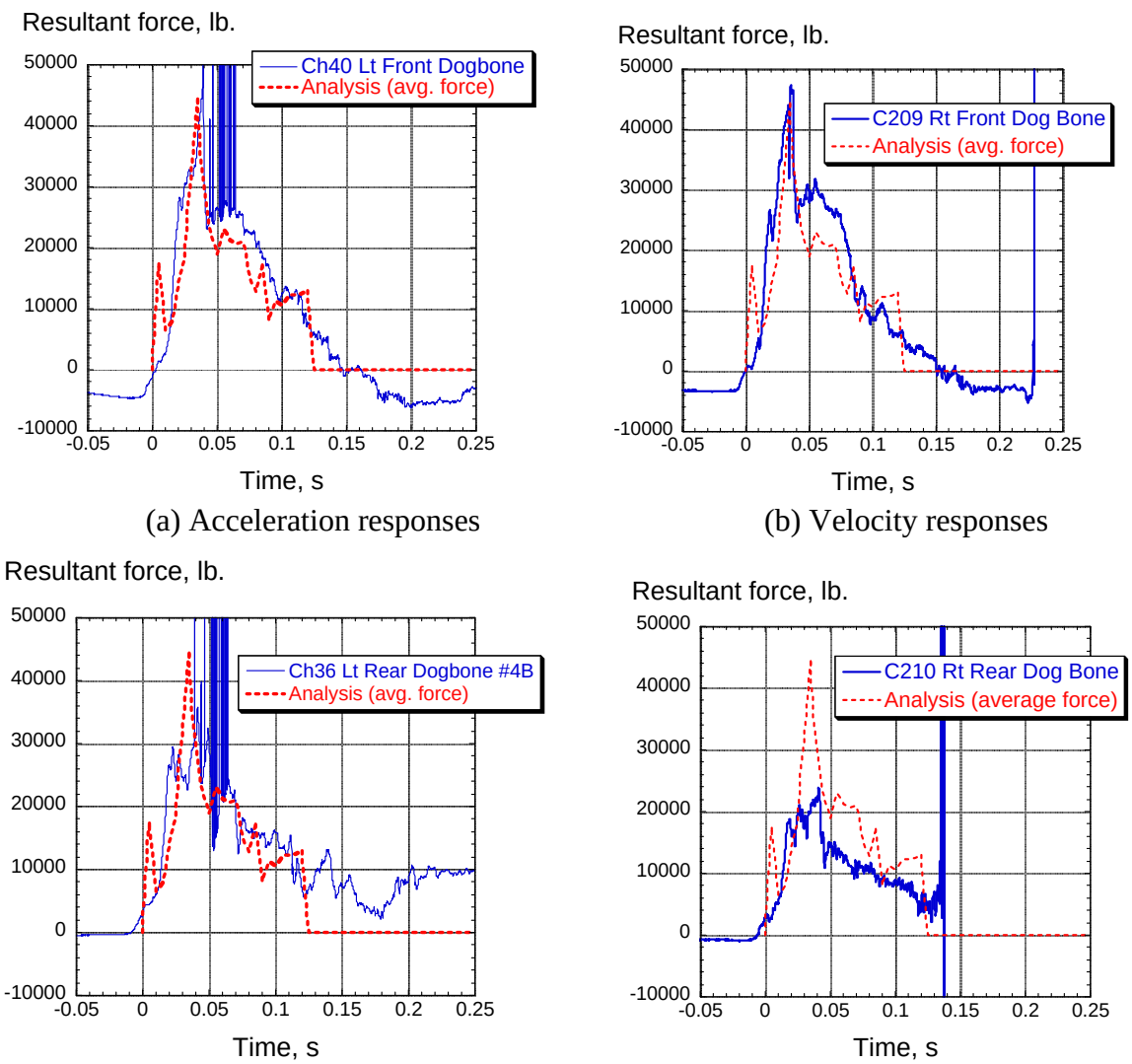

(a) Acceleration responses (b) Velocity responses

(c) Left rear dog bone (d) Right rear dog bone

Figure 19. Experimental and Predicted Dog Bone Force Time Histories

4.4 ASSESSMENT OF TEST ANALYSIS CORRELATION.

In general, reasonable agreement was obtained between the experimental and analytical data, especially when considering the complexity of the test article. The simulation accurately predicted the major structural failure, the collapse and failure of the fuselage frames supporting the wing structure. However, some differences in the experimental and analytical structural deformations were observed. In the model, the wing exhibited more bending than seen experimentally, resulting in higher wing-tip displacement. In the test, the wing exhibited a large forward (pitching) rotation, likely due to the forward location of the simulated engine masses. While the inertial properties of the simulated engines were represented in the model using concentrated masses, the model did not capture this pitch rotation of the wing. Another possible reason that the model failed to simulate this behavior was that nodal constraints were used to maintain a vertical orientation of the wing attachment structure, including the dog bones.

The model predicted the experimental acceleration, velocity, and force time histories quite well. The high level of agreement achieved for the floor-level acceleration responses is important in that these pulses are transmitted to the seats and occupants during a crash. Also, these data are needed to accurately assess dynamic seat criteria for regional transport airplane.

5. PARAMETRIC STUDY: VARYING FUEL LOADING.

A parametric study was conducted to examine the influence of varying fuel weight on the response of the heavy fuselage frames. Consequently, the original ATR 42 model was executed for two cases. For the first case, the fuel loading in the wing was reduced by half, from 8700 lb to 4350 lb. For the second case, the model was executed with no fuel loading. A comparison of the inertial properties of the three models, full-fuel, half-fuel, and no-fuel, are shown in table 2.

Table 2. Inertial Properties of Fuel-Loading Models

c.g. location	Full-Fuel Model (33,120 lb)	Half-Fuel Model (28,869 lb)	No-Fuel Model (24,519 lb)
x (in.)	471.5	470.1	468.0
y (in.)	0.24	0.28	0.33
z (in.)	142.6	138.4	132.7

A comparison of structural deformation for the three fuel-loading cases is shown in figure 20. The vertical displacement of the wing and the deformation of the fuselage are reduced as fuel loading is decreased. In addition, as fuel loading decreases, the oscillatory response of the wing increases.

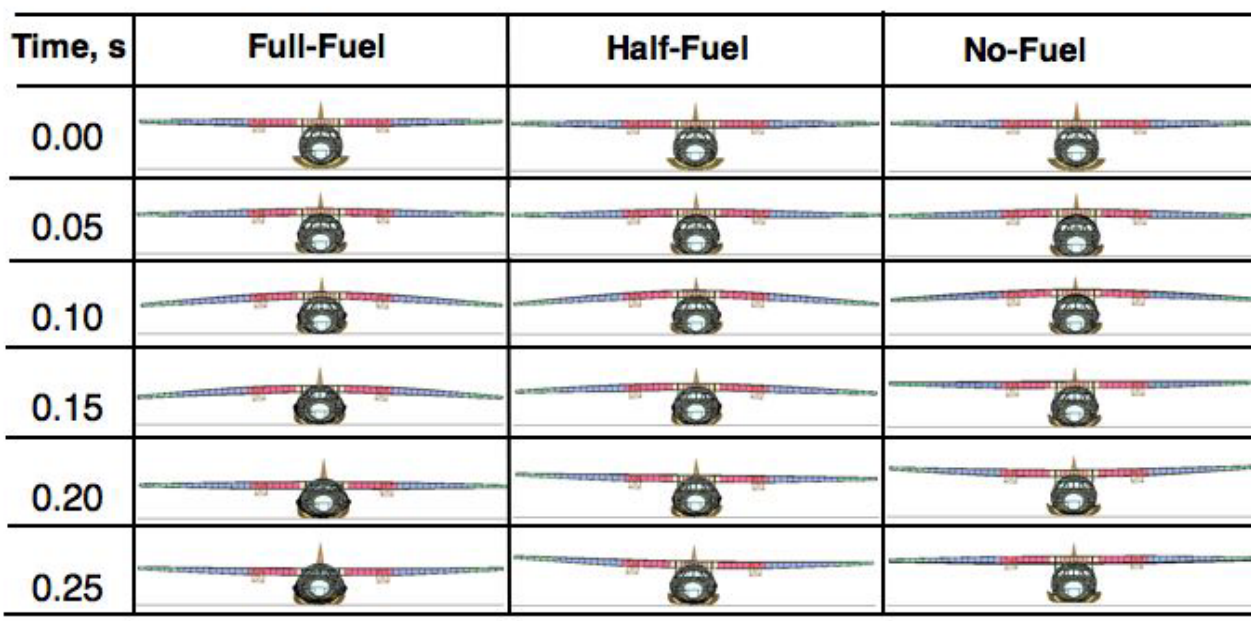

Figure 20. Wing Structural Deformations for Fuel-Loading Models

Figure 21 shows an isolated view of the fuselage frames at FS 25 and FS 27 at the end of the simulation (t = 0.25 sec) for the three fuel-loading models. For the full-fuel case, the fuselage frames exhibit plastic deformation, buckling, and multiple failures. Note that in LS-DYNA, when an element fails, it is removed from the simulation. Similar damage is observed for the half-fuel case, but not nearly of the same magnitude. For the no-fuel case, some elements in the model failed; however, the model did not exhibit global failure of the frame. As an additional comparison, the vertical displacement responses of node 20931, which is located at the bottom center of the wing (ceiling) as shown in figure 22(a), are plotted in figure 22(b). The plot indicates that the wing displaces the maximum amount for the full-fuel case, approximately 35 in. In comparison, the no-fuel case has a maximum displacement of about 12 in. It is also interesting to note that the time to reach maximum displacement is much greater for the full-fuel case.

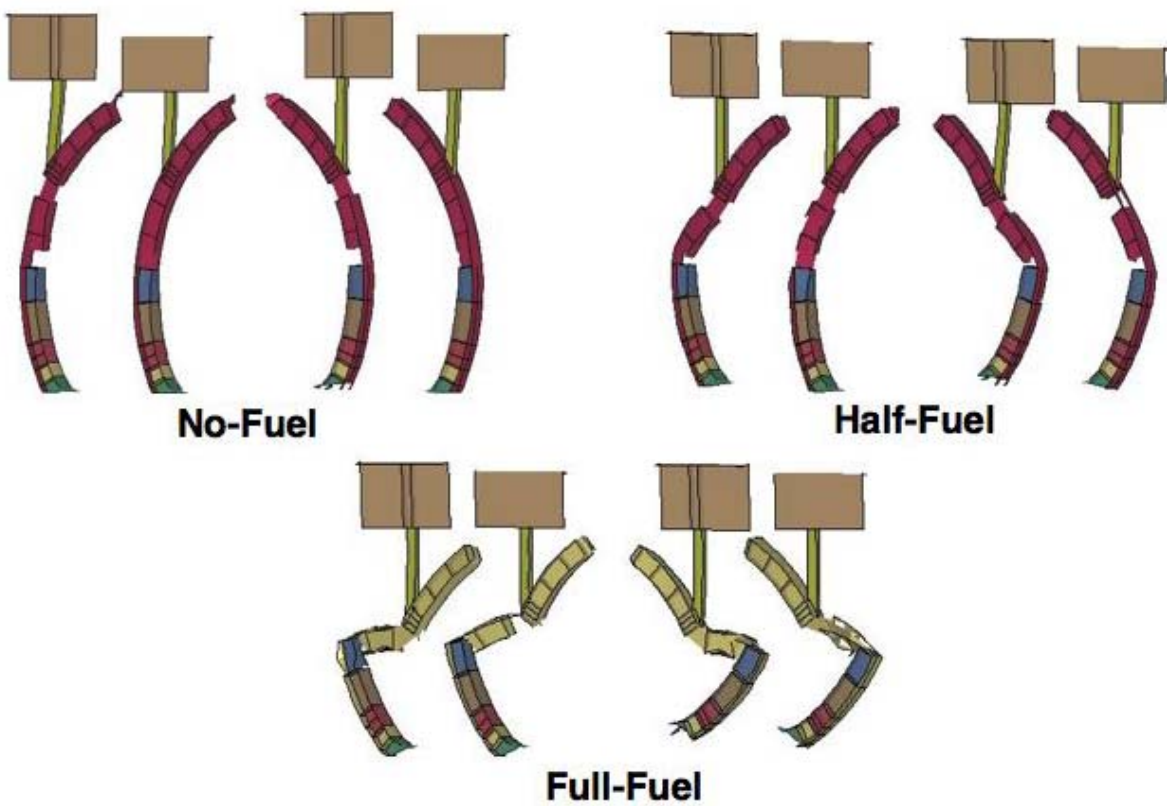

Figure 21. Deformation of FS 25 and FS 27 for Fuel-Loading Models

Selected acceleration and velocity time history comparisons are presented to demonstrate the influence of varying fuel loading on the dynamic structural response of the airframe. For example, the acceleration and velocity responses of the left and right outer floor tracks at FS 20 and FS 18 are shown in figures 23 and 24, respectively, for the three fuel loading cases. These plots indicate that fuel level makes little difference in the acceleration and velocity responses for channels located in the forward floor region.

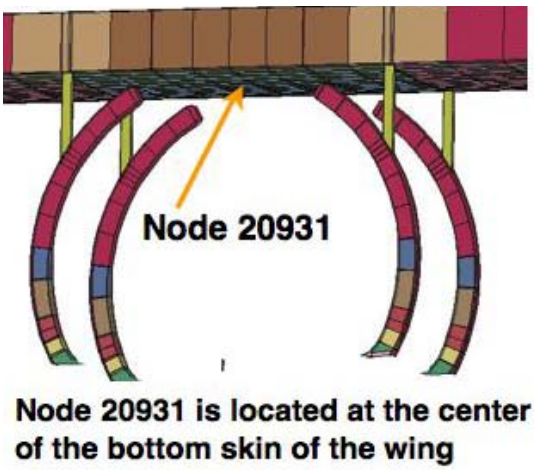

(a) Node location

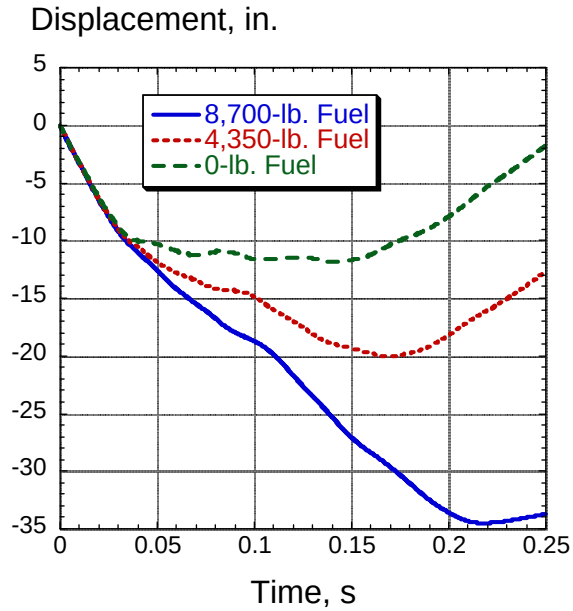

(b) Displacement comparison

Figure 22. Displacement Time History Responses for Node 20931

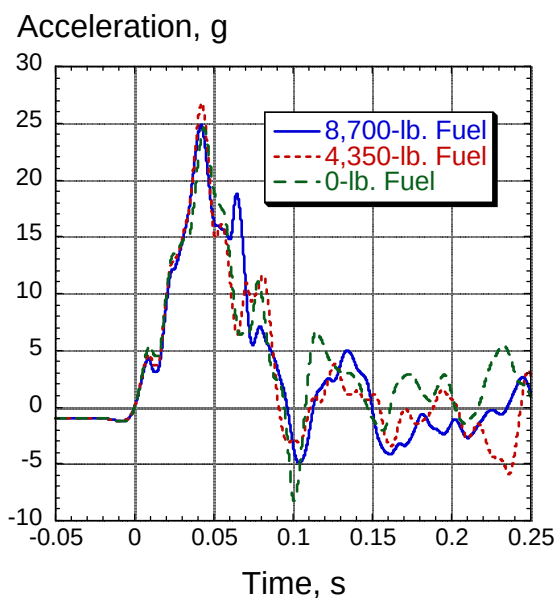

(a) Acceleration responses

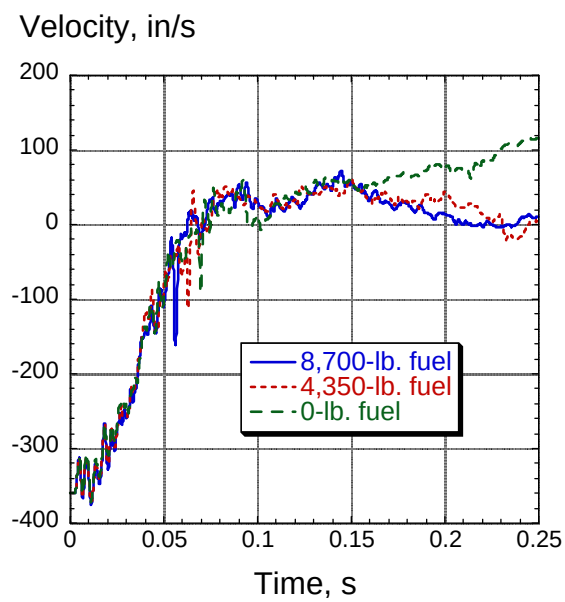

(b) Velocity responses

Figure 23. Predicted Responses for the Left Outer Floor Track at FS 20 for Fuel-Loading Models

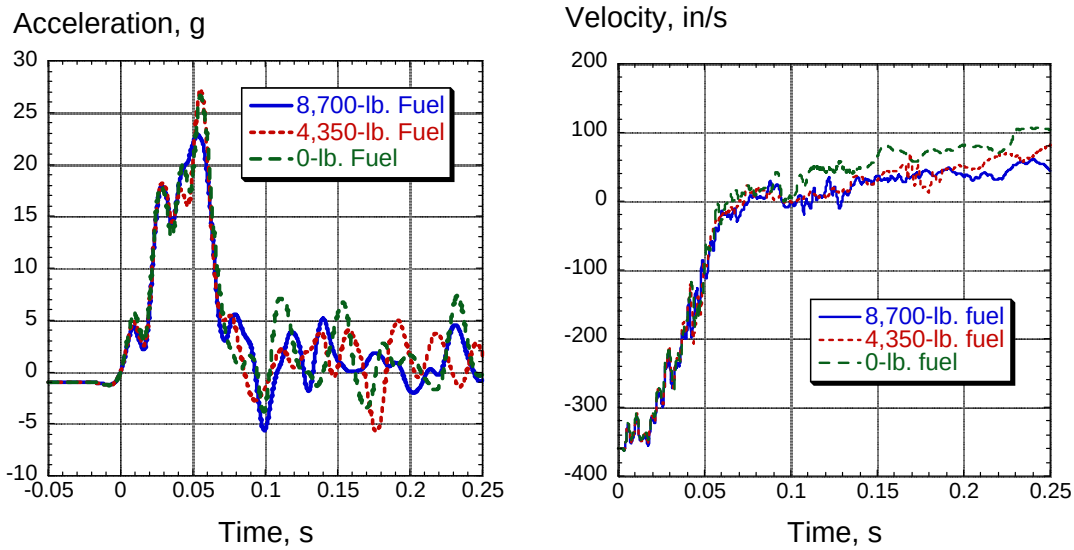

(a) Acceleration responses (b) Velocity responses

Figure 24. Predicted Responses for the Right Outer Floor Track at FS 18 for Fuel-Loading Models

Acceleration and velocity responses of the aft floor region are plotted in figures 25 and 26, specifically the left inner floor track at FS 29 and the right inner floor track at FS 35. Some differences are observed in the acceleration and velocity responses of the left inner floor track at FS 29, which is located on the floor just aft of the longitudinal position of the wing, as a function of fuel loading. For example, peak accelerations range from 26 to 38 g's. However, the responses at the right inner floor track at FS 35, which is located near the rear of the airplane, are similar with almost no differences attributed to fuel loading, except that the no-fuel model exhibits a more oscillatory response.

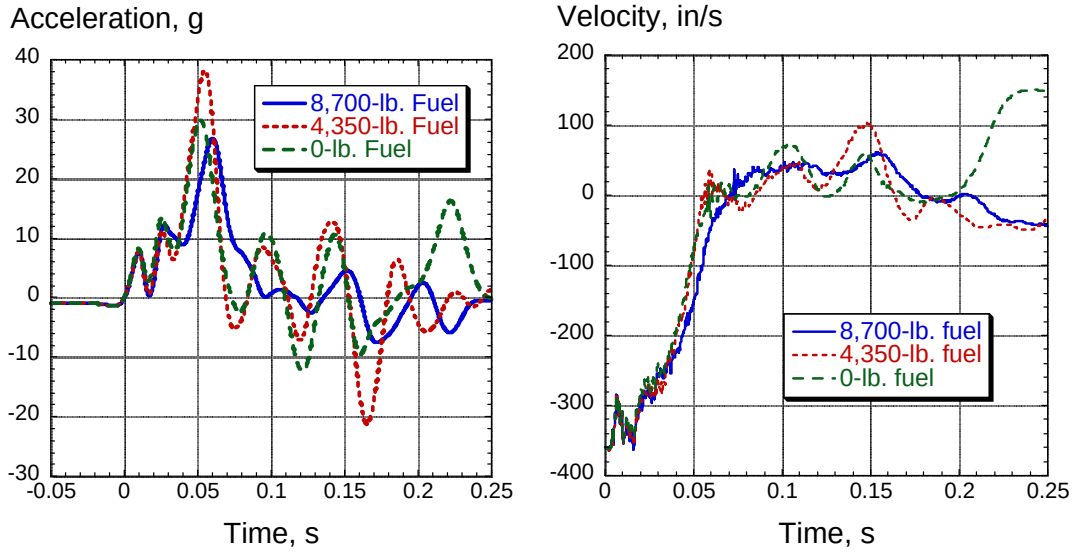

(a) Acceleration responses (b) Velocity responses

Figure 25. Predicted Responses for the Left Inner Floor Track at FS 29 for Fuel-Loading Models

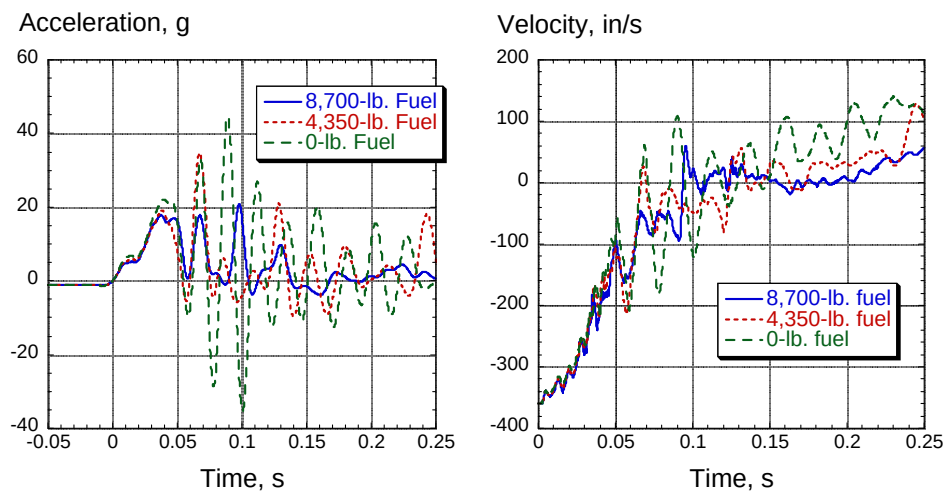

(a) Acceleration responses (b) Velocity responses

Figure 26. Predicted Responses for the Right Inner Floor Track at FS 35 for Fuel-Loading Models

The acceleration and velocity responses for the ceiling at FS 26 and the tail section at FS 47 are shown in figures 27 and 28, respectively, for the three fuel loading cases. For these two locations, some dramatic differences were observed based on fuel loading. At the bottom center of the wing at FS 26, the acceleration peaks were a function of fuel loading, with the trend that the higher the mass, the lower the acceleration peak. A similar trend was observed at the center of the tail section at FS 47. Generally, for the floor-level acceleration responses, only minor differences in acceleration and velocity responses were observed for locations away from the wing. Yet, the tail section at FS 47 shows some variations in responses. This behavior can be attributed to the fact that the tail section response was greatly influenced by the c.g. location. As shown in table 2, the longitudinal position of the c.g. is approximately 4 in. forward of its original location for the no-fuel scenario.

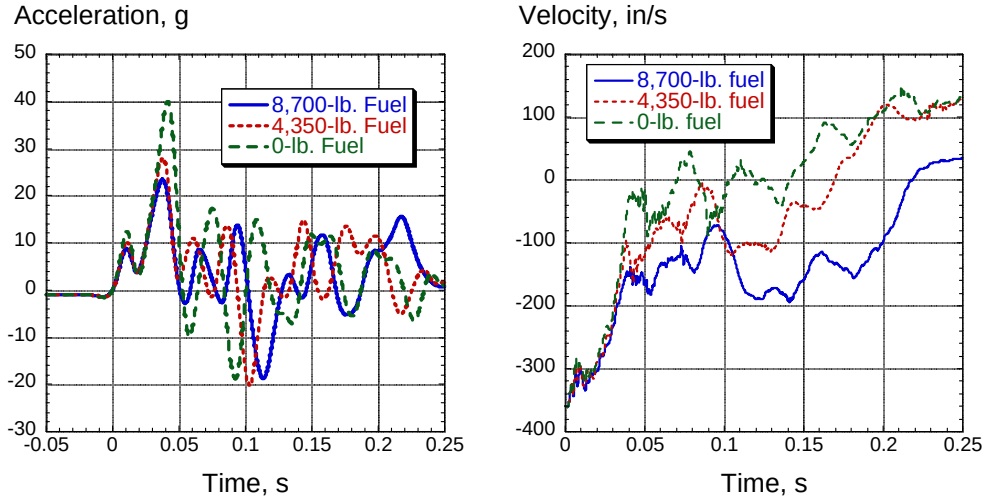

(a) Acceleration responses (b) Velocity responses

Figure 27. Predicted Responses for the Ceiling at FS 26 for Fuel-Loading Models

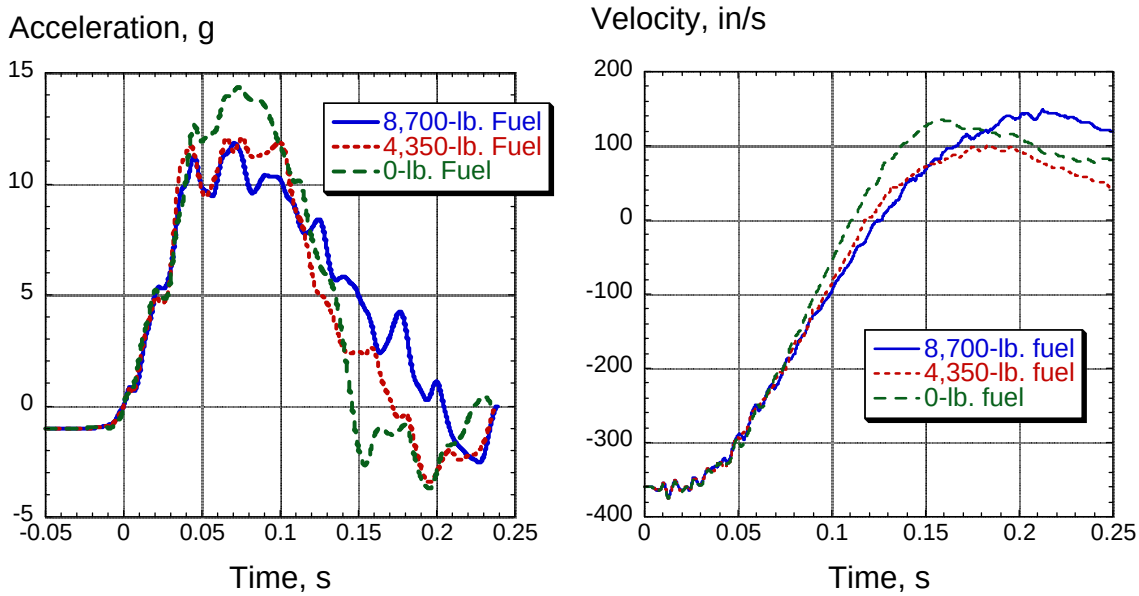

(a) Acceleration responses (b) Velocity responses

Figure 28. Predicted Responses for the Tail at FS 47 for Fuel-Loading Models

6. MODIFIED ATR 42 MODEL.

Following the initial test analysis correlation, several modifications to the model were implemented to improve the level of correlation. One modification was to remove the large number of nodal discontinuities in the initial mesh. In most cases, these discontinuities were an artifact of the way in which the model was initially developed. The corrected mesh model was executed and analytical predictions were compared with the experimental data, as well as predictions from the original model. Another modification involved updating the material properties of the heavy fuselage frames at FS 25 and FS 27. Coupons were cut from pieces of the fuselage frames, and tensile tests were performed to determine accurate material properties, including strain-rate effects. Since the most highly stressed region in the airframe are the two heavy fuselage frames at FS 25 and FS 27, an independent static and dynamic loads analysis was performed on a separate two-frame model. The two-frame model was also executed with the original baseline material properties and with the updated as-tested material properties to determine the influence on structural response. Finally, a refined mesh model of the ATR 42 was developed and executed. This model included a mesh refinement of the wing support structure that was coarsely meshed in the original model. A comparison of analytical predictions from the refined mesh model with experimental data and the original model predictions were made. Each model improvement was implemented independently of one another. The results of each modification are discussed in the following sections.

6.1 CORRECTED MESH MODEL.

6.1.1 Development of the Corrected Mesh Model.

The original ATR 42 finite element model contained more than 5400 nodal discontinuities or disconnects, which were discovered as a result of initial penetration warnings when the model was initially executed. An example of nodal discontinuities is shown in figure 29. In most cases, they represent intersections of surfaces where the meshes do not match up. The large number of nodal discontinuities in the model was the result of the size and complexity of the model. Also, the method in which the model was developed (incrementally detailed) contributed to the problem. The discontinuities did not prevent the model from executing; however, they could have caused problems with the contact definitions. For example, if a node has already penetrated a surface at the beginning of the simulation, the code has several options. It can ignore the initial penetration, or it can fix the initial penetration by moving the node to the correct location on the other side of the contact surface. For the contact definition used in the model (*CONTACT_AUTOMATIC_SINGLE_SURFACE), the default setting is for no checking to be performed. However, for this model, the default was changed to permit initial penetration checking.

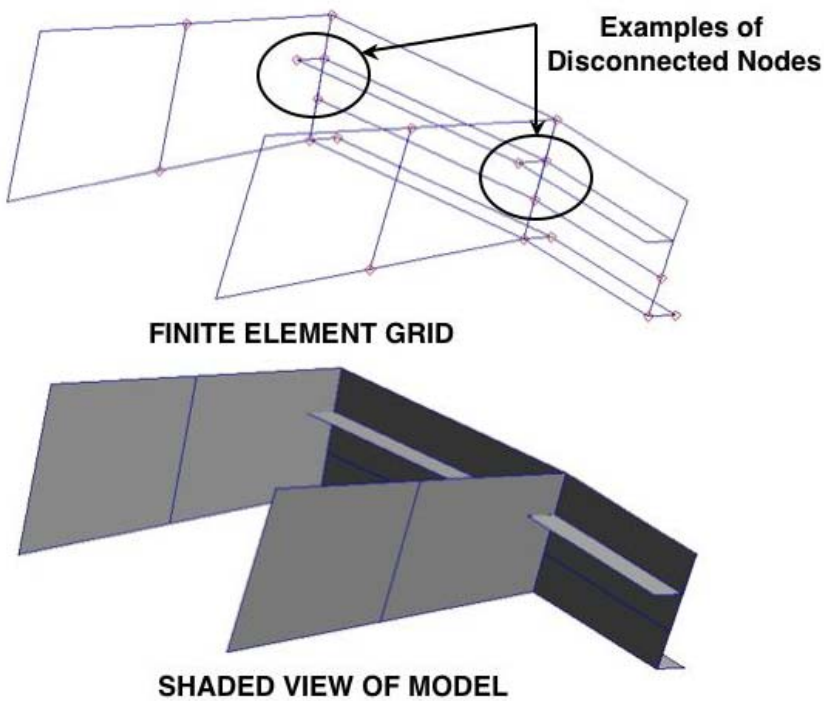

Figure 29. Portion of a Finite Element Mesh Showing Several Nodal Discontinuities

The process of eliminating the nodal discontinuities was initiated by tracking down each node listed in the initial penetration warning messages given in the LS-DYNA d3hsp output file. The mesh corrections were made using the preprocessing software package, MSC.Patran [8]. An example of a corrected mesh is shown in figure 30. Often, the process of correcting the mesh required the use of triangular elements, which are generally not as efficient or robust as quadrilateral elements. The correction process required several months of fairly tedious work.

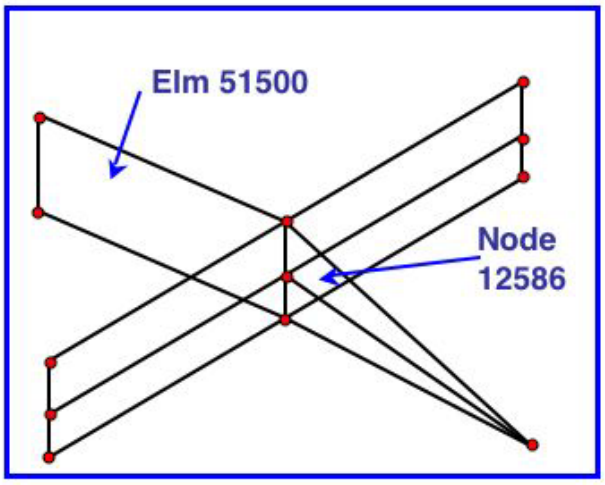

(a) Initial penetration warning: Node 12586 has penetrated Element 5150

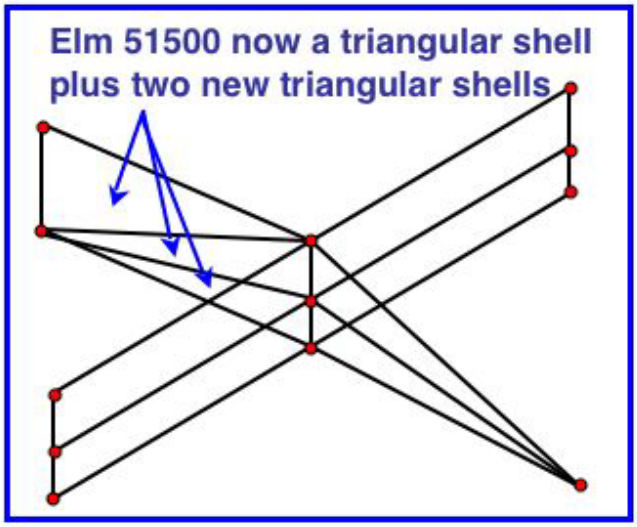

(b) Element connectivity fixed and two triangular elements added

Figure 30. Corrected Nodal Discontinuities

The completed corrected mesh model is shown in figure 31. This model contains 56,647 nodes, 67,653 elements, 55 parts, 11 unique materials, and 1 contact definition. Comparisons of the properties of the corrected mesh model with the original model are provided in table 3. For reference, the inertial properties of the test article are also shown. As indicated in table 3, the number of nodes was reduced by approximately 1000, while the number of elements was increased by about 4700. In the example shown in figure 30, one quadrilateral shell element (51500) was replaced by three triangular shell elements. Thus, some mesh refinement occurs as a by-product of correcting the nodal discontinuities in the model.

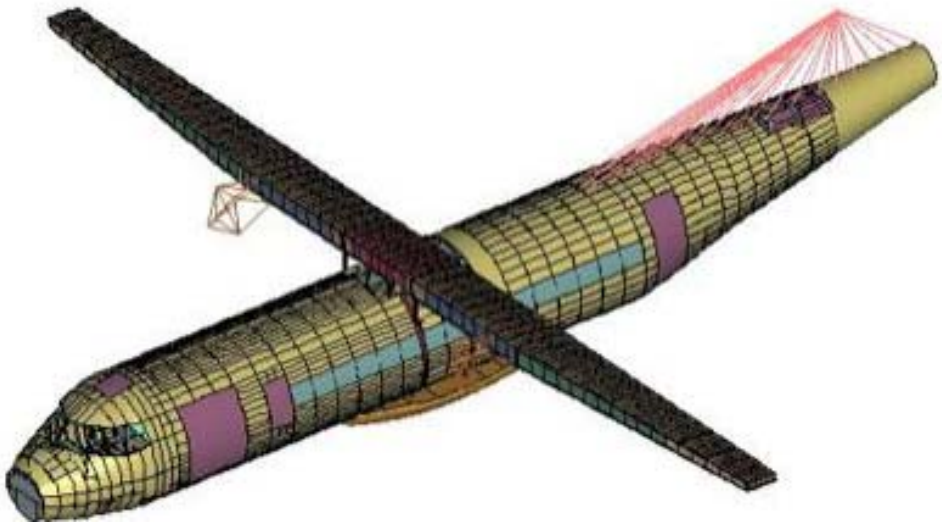

Figure 31. Picture of the Corrected Mesh Model

Table 3. Comparison of the Original and Corrected Mesh Models With the ATR 42

	Original Model	Corrected Mesh Model	Test Article
Nodes	57,635	56,647	
Elements	62,989 elements - 60,193 quadrilaterals - 566 triangular shells - 526 beams - 1,704 points	67,652 elements - 61,157 quadrilaterals - 4,267 triangular shells - 525 beams - 1,703 points	
Parts	54	55	
Materials	11	11	
Weight (lb)	33,120	32,950	33,200
c.g. longitudinal position (in.)	471.5	473.8	469.2

6.1.2 Results of the Corrected Mesh Model.

Plots of acceleration and velocity time histories for the original model, the corrected mesh model, and the experiment at the left outer floor track at FS 20 are shown in figure 32(a) and (b), respectively. The comparisons are shown in time, up to 0.15 sec, since the major acceleration pulse is over by that time. Some differences are noted. For example, the peak acceleration for the corrected mesh model is lower than the original model and the experiment, but the peak occurs closer in time to the experiment. However, as shown in figure 32(b), these differences are minimized when the velocity responses are compared. A similar comparison is shown in figure 33 for the acceleration and velocity responses at the right outer floor track at FS 18. Again, minor differences between the original and corrected mesh models are observed in the acceleration responses, but these differences are reduced when the velocity responses are compared.

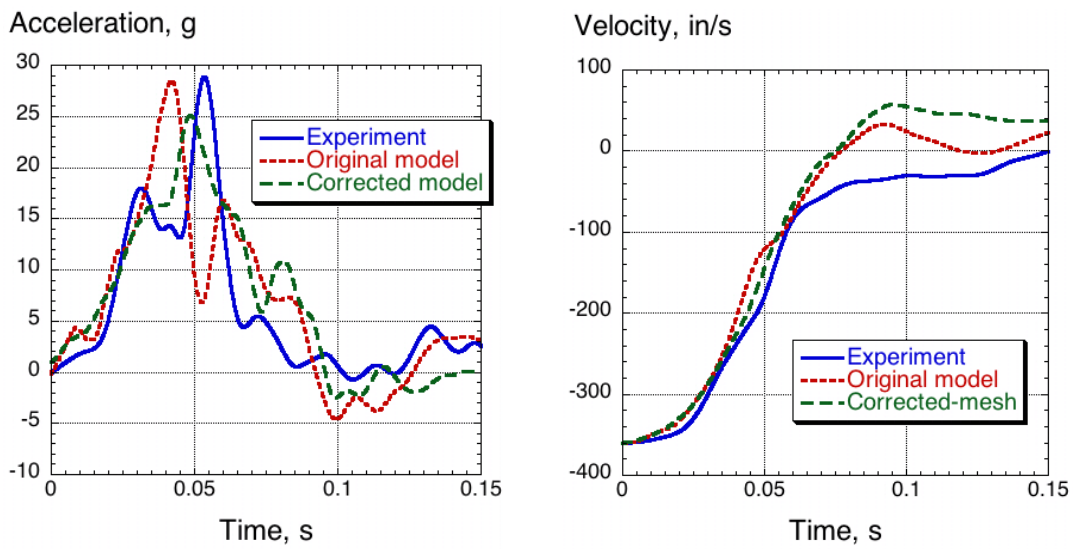

(a) Acceleration responses (b) Velocity responses

Figure 32. Acceleration and Velocity Responses at the Left Outer Floor Track at FS 20

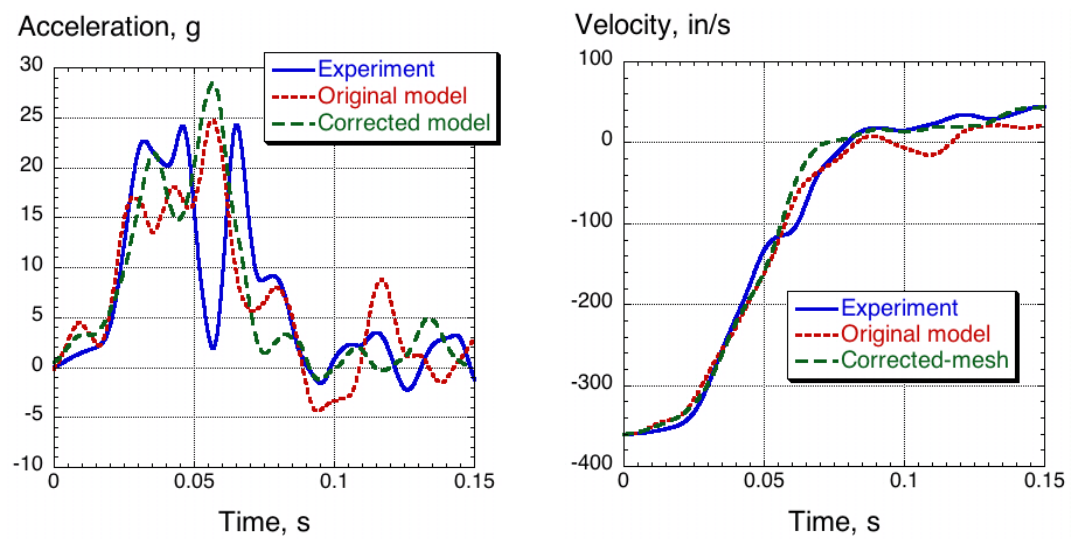

(a) Acceleration responses (b) Velocity responses

Figure 33. Acceleration and Velocity Responses for the Right Outer Floor Track at FS 18

Plots of acceleration and velocity time histories of the original model, the corrected mesh model, and the experiment are plotted in figures 34 and 35 for the left inner floor track at FS 29 and the right inner floor track at FS 35. At the left inner floor track location, the peak acceleration of the corrected mesh model matches that of the original model; however, the shape of the pulses is quite different. The differences in the acceleration responses are also observed in the velocity responses. For example, the velocity response of the corrected mesh model crossed zero velocity by 0.065 sec, which is much earlier than either the original model or experiment, as shown in figure 34(b). These results indicate that the corrected mesh model is too stiff in this region.

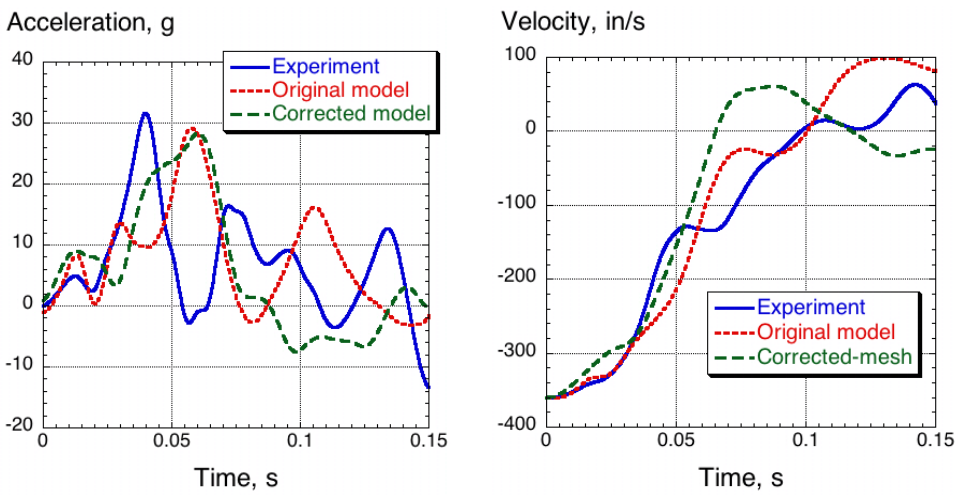

(a) Acceleration responses (b) Velocity responses

Figure 34. Acceleration and Velocity Responses for the Left Inner Floor Track at FS 29

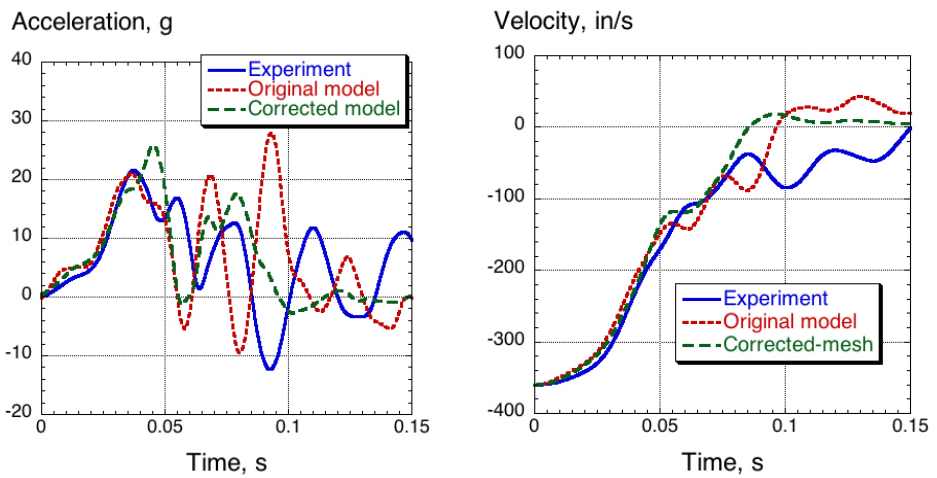

(a) Acceleration responses (b) Velocity responses

Figure 35. Acceleration and Velocity Responses for the Right Inner Floor Track at FS 35

Near the rear floor area of the airplane, the acceleration responses are lower in magnitude, as shown in figure 35(a). The initial acceleration peaks are approximately 20-25 g's. The velocity responses at the right inner floor track at FS 35 are shown in figure 35(b). This plot indicates that all three curves correlate very well up to 0.075 sec, at which time the experimental velocity response flattens out and does not cross zero until 0.15 sec. However, the velocity responses of the corrected-mesh and the original model do not flatten out and cross zero at 0.085 and 0.095 sec, respectively.

The acceleration and velocity responses for the ceiling at FS 26 and the tail section at FS 47 are plotted in figures 36 and 37, respectively, for the original and corrected mesh models and the experiment. At the wing location, the correlation did not improved, but got worse with the corrected mesh model. The peak acceleration of the corrected mesh model (25 g's) is higher

even than the original model (20 g's). At this location, the peak experimental acceleration was 10 g's. These differences indicate that the model was too stiff at this location, and that the corrected mesh model was stiffer than the original model. Also, the velocity was removed much more quickly for the corrected mesh model than for either the original model or the experiment.

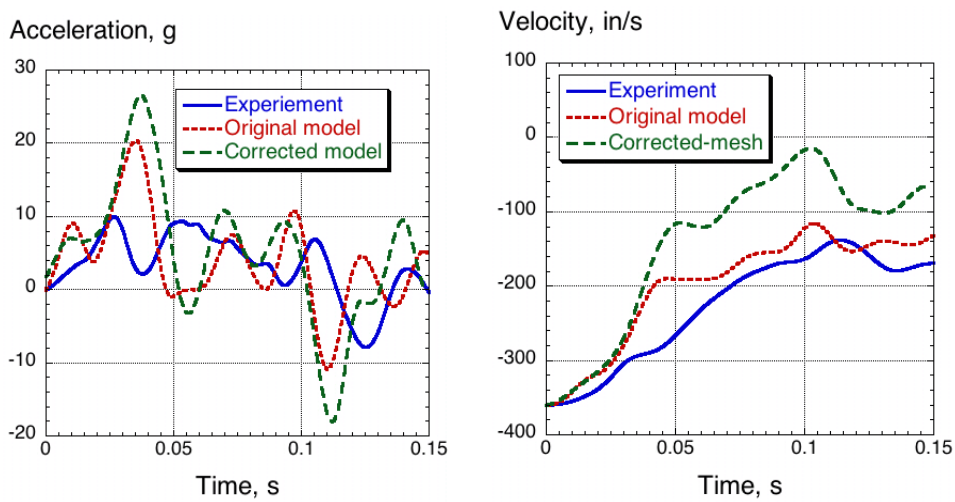

(a) Acceleration responses (b) Velocity responses

Figure 36. Acceleration and Velocity Responses for the Ceiling at FS 26

Finally, the acceleration and velocity responses of the tail section at FS 47 are plotted in figure 37 for the original and corrected mesh models and the experiment. The original model showed excellent correlation with the accelerometer data at this location, with the analysis correctly predicting the shape, magnitude, and duration of the experimental acceleration response almost exactly. Likewise, a high level of agreement was obtained between the velocity responses of the original model and the experiment. However, the correlation of the corrected mesh model was worse. The acceleration response of the corrected mesh model did not match the onset rate of the acceleration response and the peak acceleration was higher than the experiment.

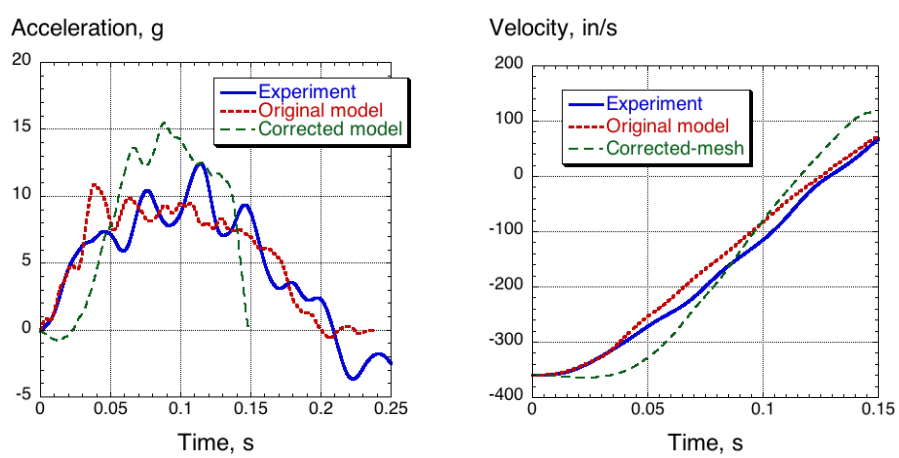

(a) Acceleration responses (b) Velocity responses

Figure 37. Acceleration and Velocity Responses for the Tail at FS 47

6.1.3 Assessment of the Corrected Mesh Model.

A considerable amount of work went into creating the corrected mesh model, and the completed model was quite different in many respects from the original model. The correlations shown in the previous section indicate that, in general, the corrected mesh model did not correlate as well with the experimental data as did the original model. Two explanations were proposed. The first explanation for the poor correlation was the large increase in the number of triangular elements in the corrected mesh model. As indicated in table 3, the original model had a relatively small number of triangular elements (566), whereas the corrected mesh model had a total of 4267 triangular elements. This difference is depicted in figure 38, which shows the triangular elements in the original and corrected mesh models. As illustrated in figure 30, triangular elements were used as a convenient method to eliminate the large number of nodal discontinuities in the model. Unfortunately, the use of triangular elements is not recommended. These elements are historically too stiff for dynamic simulations. Thus, increasing the number of triangular elements in the model will increase the overall stiffness of the model. As the stiffness of the model increases, higher peak accelerations and shorter pulse durations are expected. One example, cited in reference 15 states:

> "Conversion of an entire frontal car assembly from 4-node into 3-node elements caused all results (rigid wall force, energy absorption, accelerations…) to rise by roughly 30%. This is not acceptable."

The second explanation for poor correlation, as shown in table 3, was the inertial properties of the corrected mesh model did not match the experimental data, and the difference was greater than for the original model. These results indicate that the overall mass distribution in the model changed, which may alter the influence of inertial forces within the model under dynamic loading.

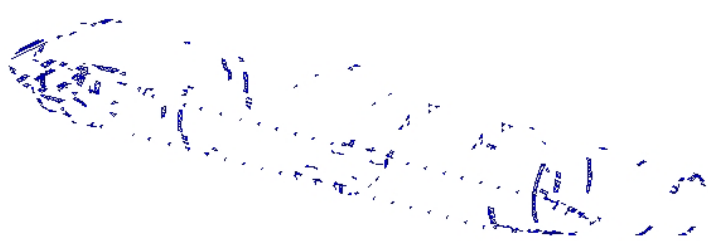

(a) Triangular elements in the original model

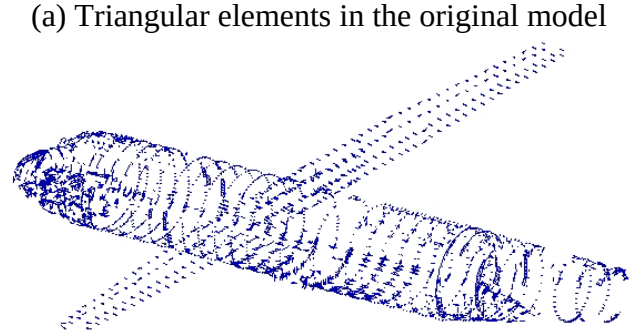

(b) Triangular elements in the corrected mesh model

Figure 38. Triangular Elements in the Original and Corrected Mesh Models

6.2 MATERIALS TESTING.

The FAA sent several pieces of the two heavy fuselage frames that support the wing of the ATR 42 airplane to National Aeronautics and Space Administration Langley. One of the pieces from the right side of FS 25 is shown in figure 39. The parts were requested to get accurate dimensions for input into the refined mesh finite element model. Once the measurements were taken, it was decided that the frames could be cut into coupons for quasi-static and dynamic materials testing. A photograph showing potential coupons to be cut from a piece of FS 25 is shown in figure 40. According to the manufacturer's handbook, the fuselage frames were fabricated of Al 7050-T7452 die forging. Several coupons were cut from the fuselage frames, the coupons were instrumented with strain gauges, and eight tensile tests to failure were performed. A photograph of the strain-gauged coupons is shown in figure 41 and photographs of the test setup are shown in figure 42.

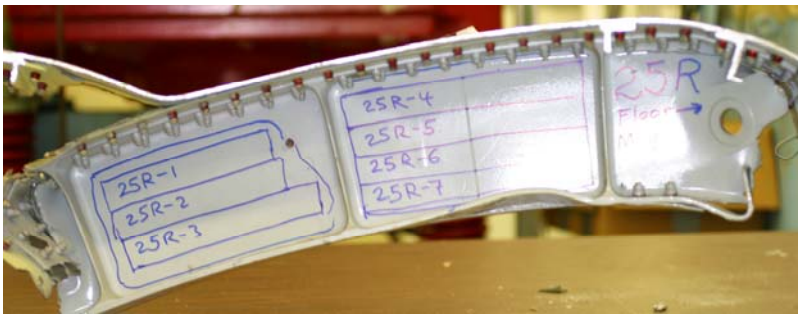

Figure 39. Location of Potential Coupons to be Cut From Frame 25

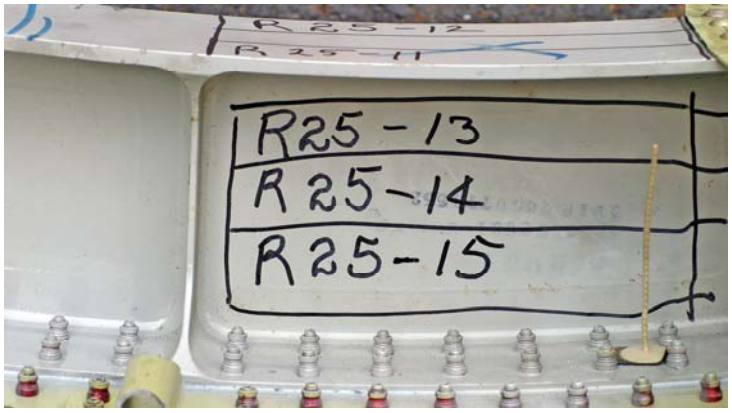

Figure 40. Location of Potential Coupons to be Cut From the Web of Frame 25

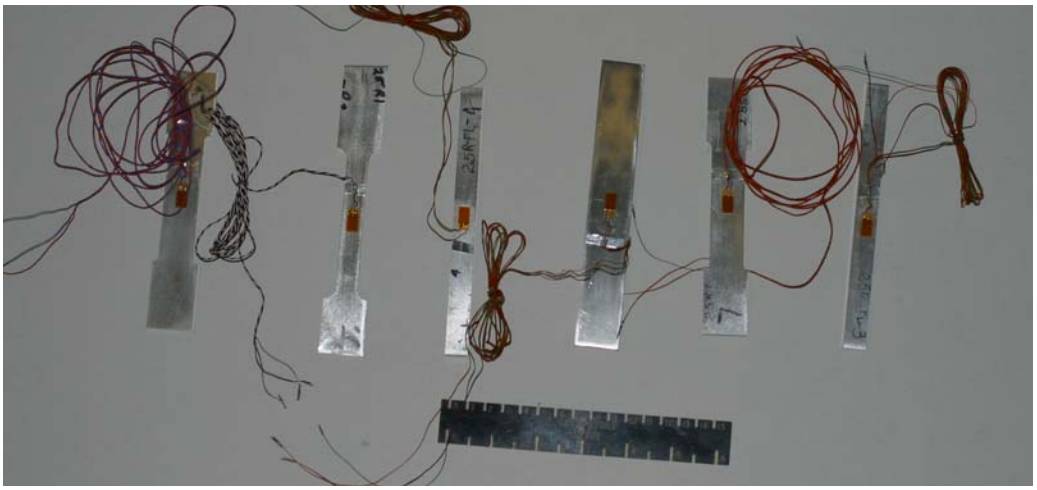

Figure 41. Tensile Coupons Cut From Fuselage Frames 25 and 27

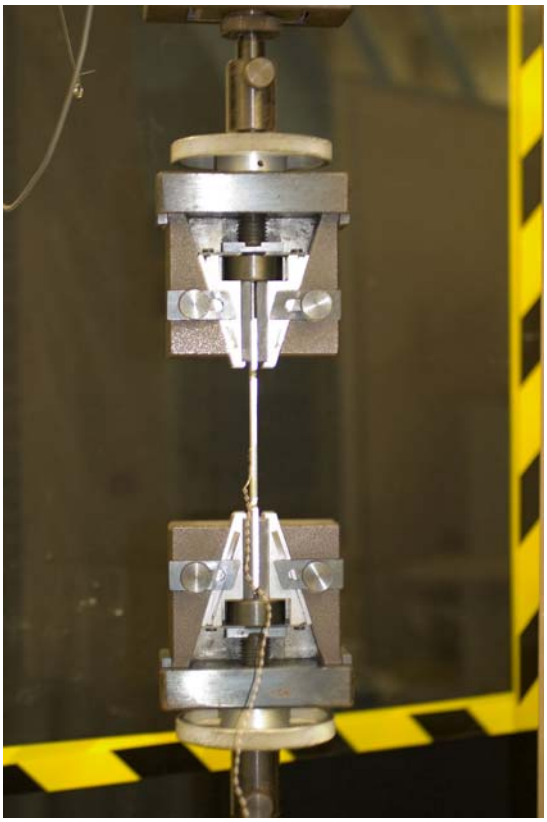

(a) Tensile test coupon mounted in grips

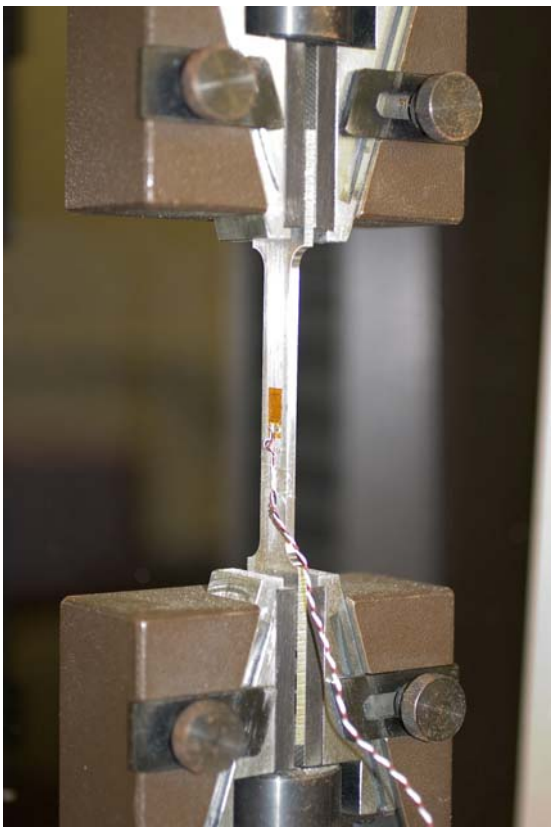

(b) Coupon instrumented with strain gauges

Figure 42. Tensile Test Setup

The tensile tests were conducted at rates of 0.1, 1.0, and 20 in. per minute. As indicated in the stress-strain plot of figure 43, no strain-rate effects were observed. Consistent material properties were obtained, including Young's modulus = 10.8e06 pounds per square inch (psi), yield stress = 65,000 psi, hardening modulus = 177,000 psi, and an ultimate strain-to-failure of

6.5%. The tests were performed on a Tinius Olsen bench-top load test machine, and displacement measurements were made using an extensometer. A comparison of the material properties of Al 7050-T7452 used in the original ATR 42 model and the as tested values is shown in table 4. A static NAsa STRuctural ANalysis (NASTRAN) [16] model of the heavy fuselage frames located at FS 25 and FS 27 was executed with the original baseline material properties and with the updated as-tested material properties. The influence of varying material properties is discussed in section 6.3.

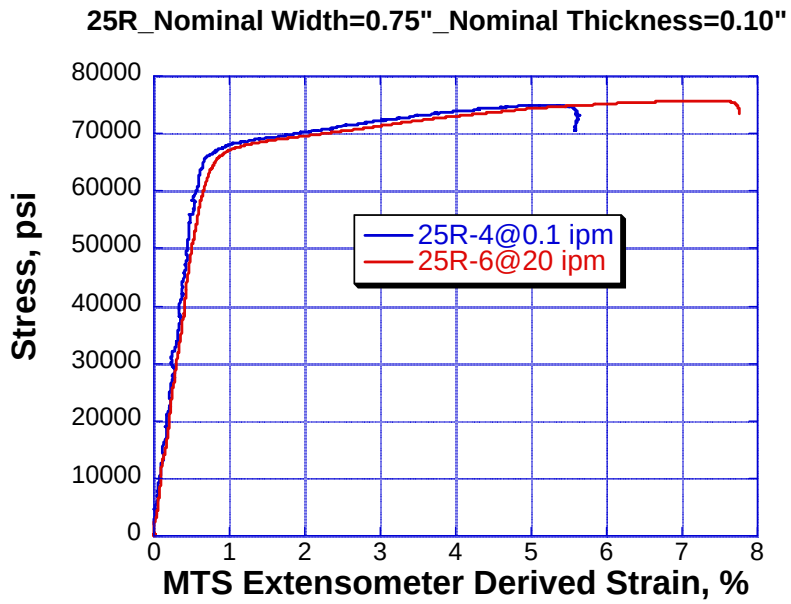

Figure 43. Stress Versus Strain Data for Aluminum Tensile Coupons

Table 4. Materials Characterization

Al 7050-T7452	Original Properties (based on handbook)	Updated Properties (based on test data)
Young's Modulus (psi)	10.4E06	10.8E06
Yield Stress (psi)	60,000	66,000
Hardening Modulus (psi)	145,335	177,000
Failure Strain (%)	3.5	6.5

6.3 STATIC AND DYNAMIC LOADS ANALYSES OF THE WING SUPPORT STRUCTURE.

6.3.1 Development of a NASTRAN Model.

The heavy fuselage frames at FS 25 and FS 27, shown in figure 3, are the primary load-bearing structure for the high wing and fuel. In the original model, these fuselage frames were meshed coarsely and the wing attachments were not represented accurately. Consequently, a separate model was developed, which contained a refined mesh of the fuselage frames at FS 25 and FS 27 and a detailed physical representation of the wing attachments and dog bones. The model was

executed using NASTRAN [16], and static loads analyses were performed to evaluate the structural response and failure of the fuselage frames.

A front view of the original frame model is shown in figure 44. Obviously, the mesh discretization of the frame is fairly crude. The figure also includes a close-up of the dog bone and upper bracket assembly. In the original model, the dog bone was represented using shell elements arranged to form an I-cross section geometry. One end of the dog bone was attached directly to the mesh of the frame and the other was attached directly to the mesh of the wing, i.e., the attachment brackets were not physically modeled. Since the brackets were not included, the rotational degrees of freedom that the actual dog bones possess were not represented in the original model. To maintain vertical alignment, the nodes forming the dog bones were constrained to allow only translational motion in the vertical direction. Also note, the upper bracket assembly was modeled simply by adding beam elements to attach the upper frame to the wing. Again, without the bracket, the correct rotational degree of freedom could not be captured by the model. Also, the original model of the frames at FS 25 and FS 27 were represented using four different section properties representing four different thicknesses. In the test article, the actual thicknesses of the web and flange varied continuously from the top to the bottom of the frame.

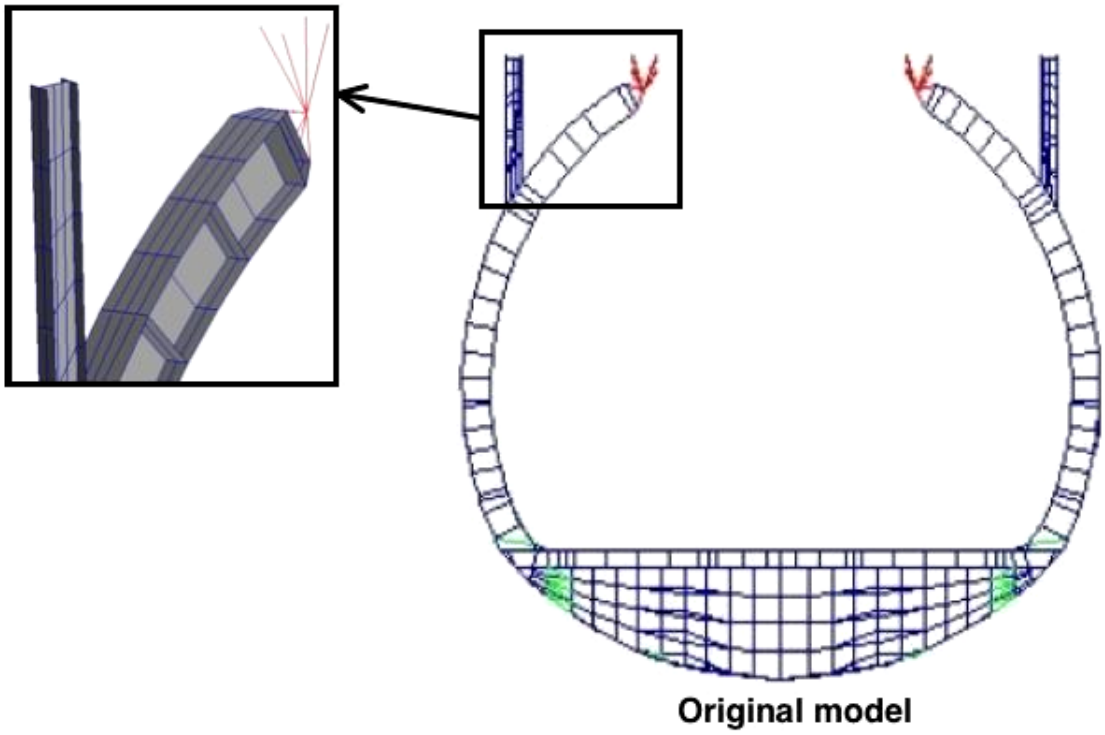

Figure 44. Front View of the Original Frame Model

A front view of the refined mesh NASTRAN model is shown in figure 45. This model was initially developed by extracting the frames from the original finite element model of the ATR 42. The new mesh is two to four times as dense as the original mesh. The refined two-frame model contains 16,064 nodes, 34,751 elements, 362 section properties, and 6 material property cards. The properties of the model were updated based on direct measurements of the frame

pieces, shown in figures 39 and 40, that were removed from the test airplane. In particular, the lower portion of the upper frame was updated with actual measured thickness values. Also updated from the original model was the addition of a stiffener in the lower portion of the frame that was absent from the original model and from the available drawings. Properties for the lower frames, floor beams, and gearbox walls were based solely on drawings and data from the original finite element model.

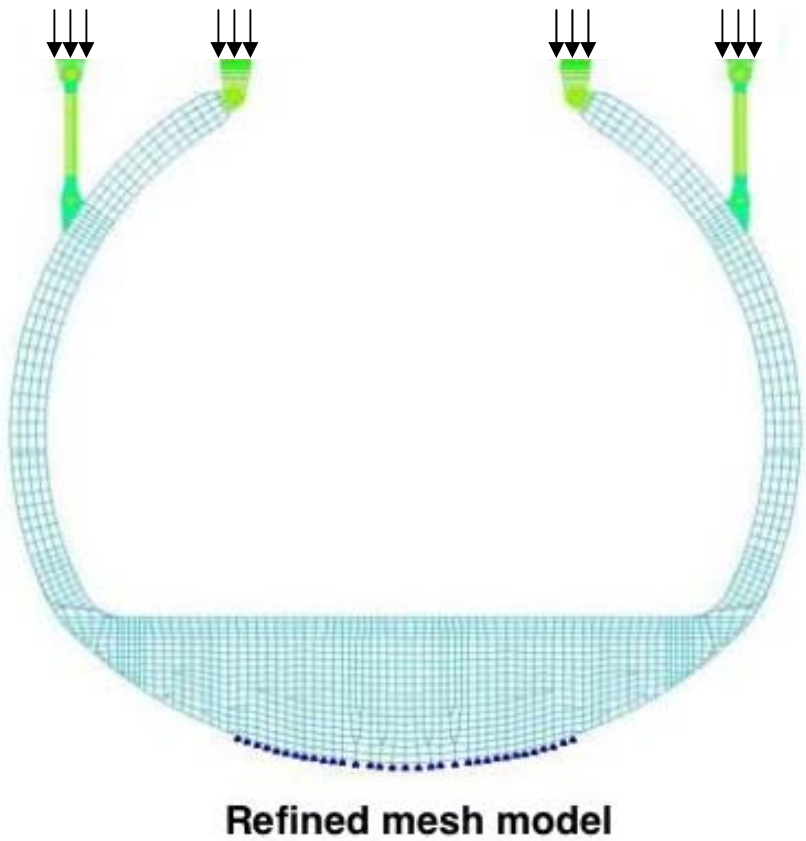

Figure 45. Front View of the Refined Frame Model

As shown in figure 46, the attachments between the frames and the wing are physically modeled, including the dog bones. The method of connecting the brackets and fittings attempts as much realism as possible while being practical. All fittings have a ball roller on the single flange side and simple holes on the double flange side. To model the ball roller portion of the attachment, a series of bar elements are attached to all nodes on the circumference of the holes and brought to a single central point. The elements can only take translational forces and, thus, allow rotations about their ends creating a socket effect. To model the holes on the two-flange side of the attachment, all circumferential nodes are projected to a line through the center of the hole. Nodes on the inside and the outside of the flange are attached to different points. This procedure allows a transfer of moment while allowing rotation about the axis of the bolt. All of the central points are then connected with a series of beam elements. This central beam has properties based on the actual bolt used to connect the fittings and brackets. The bracket and fitting attachment methods are illustrated in figure 47.

The models of the dog bones were based on actual measurements. The dog bones at FS 25 are slightly longer than those at FS 27. Since no geometry or actual fitting was available for where the dog bone mates with the wing, a bracket was created to allow some compliance and provide the pivot-rotational joint. The bracket connecting the dog bone to the wing was based on the actual bracket attached to the frame section. The dog bones and their attachments are shown in figure 46.

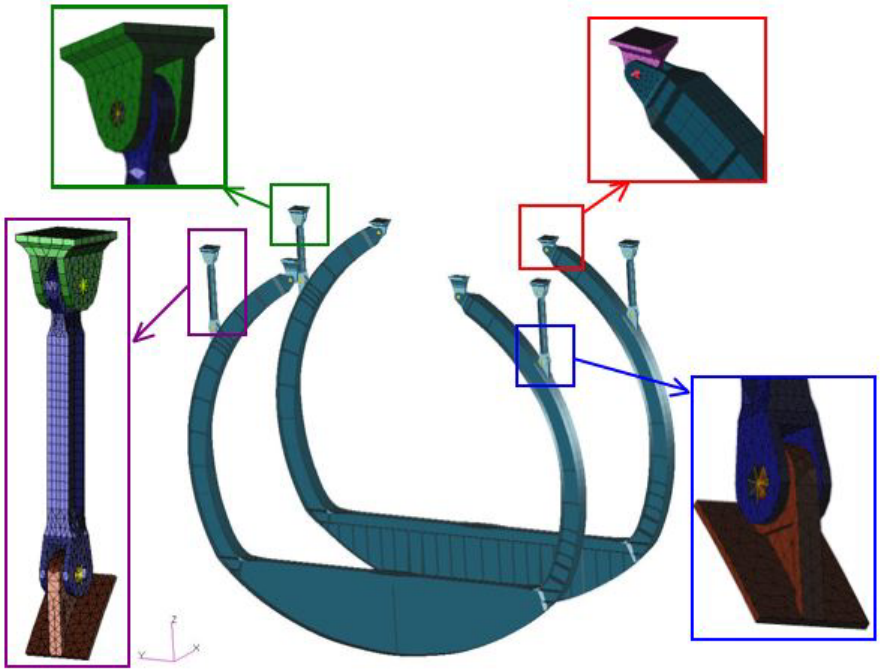

Figure 46. Two-Frame Model Showing Attachments

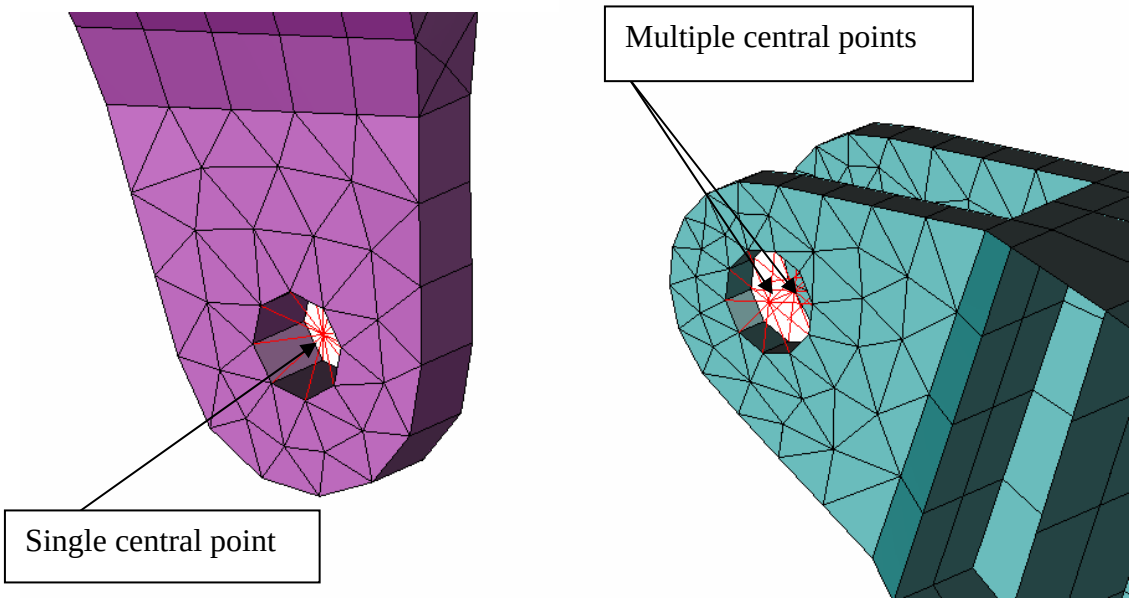

Figure 47. Bracket and Fitting Attachment Method

Once the mesh refinements were completed, loading was applied to the model. For this simulation, an enforced displacement was applied to the wing fittings. The loading configuration used for the analysis is illustrated in figure 45. The triangles represent where the model was held in the vertical direction, and the arrows indicate where the enforced displacements were applied. Additionally, the enforced displacement points were constrained to move only in the vertical direction. The model was executed to a maximum displacement of 2.0 in. in 0.1-in. increments, which was well past the point where the structure became nonlinear due to buckling and plasticity effects. Additionally, the frames were constrained in the fore-aft direction along the outside of the frames and along the floor beams to reflect the stiffening effects of the skins and flooring, which were not present in the model. These nodal constraints are illustrated in figure 48.

Two analyses of the model were performed. The first simulation was executed with the original baseline material properties. After material testing was performed on coupons cut from the test frames, the modulus, yield stress, hardening modulus, and ultimate failure strain were found to be higher in the test coupons. Consequently, the model was executed a second time with the updated as-tested material properties listed in table 4. Note that only the properties for Al 7050-T7452 were actually changed.

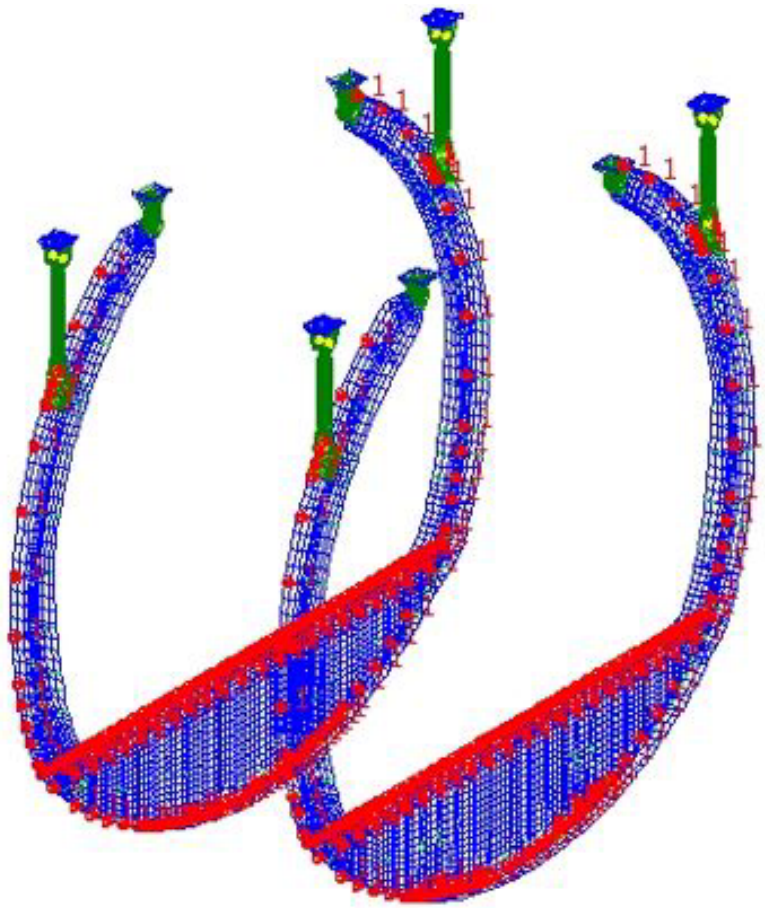

Figure 48. Nodal Constraints in the Fore-Aft Direction

6.3.2 Results of the NASTRAN Static Loads Analysis.

The results of the two NASTRAN simulations are shown in figures 49 and 50, which contains curves of the dog bone reaction force, the reaction force of the upper frame attachment (labeled frame in the plot), and the combined force (dog bone plus frame) versus displacement for FS 25 and FS 27, respectively. Note that the displacement values represent the enforced displacements applied to the model. The compressive forces are positive and tensile forces are negative. Also, the curves with the open markers represent the simulation results from the baseline material model, while the filled markers represent the results from the simulation with as-tested material properties. Overall, the behaviors of the two models are very similar with the primary difference being the point where structural nonlinearity occurs. The initial slopes of the baseline model and the as-tested model are nearly identical, but the baseline model becomes nonlinear earlier and has a lower peak load. It is also interesting to note that the force in the dog bones is compressive (the reaction force is tensile, thus the force in the dog bone is compressive), whereas the force at the frame attachment is tensile. Finally, even though equivalent enforced displacements are applied, the magnitude of the force is much higher in the dog bones than in the frame attachments.

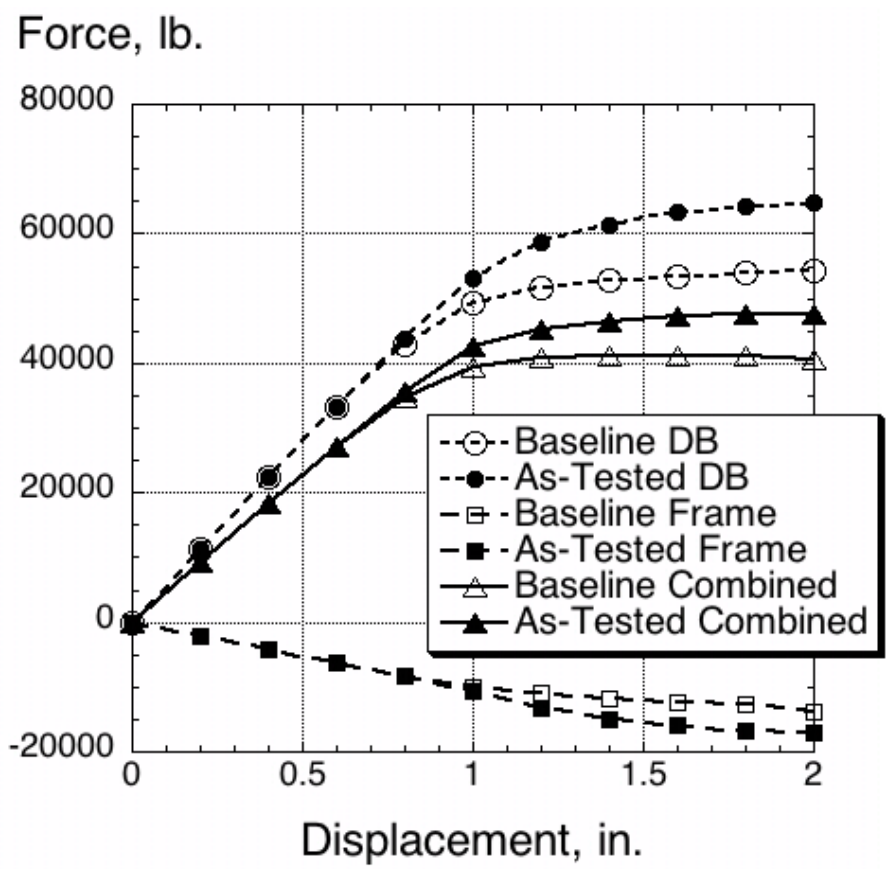

DB = Dog bone
Note: Compressive forces are positive and tensile forces are negative.

Figure 49. Predicted Force Responses for the Fuselage Frame at FS 25

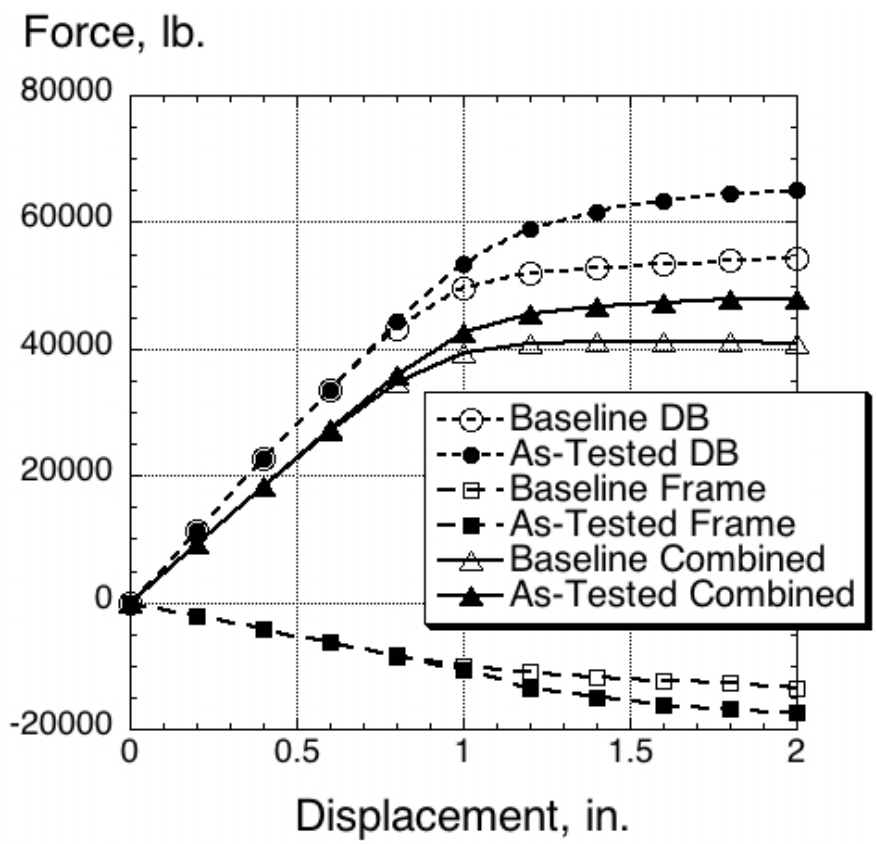

DB = Dog bone

Figure 50. Predicted Force Responses for the Fuselage Frame at FS 27

In the baseline model, when the structure had an enforced displacement of greater than 1.5 in., the frame began to unload overall. For the as-tested model, the unloading began at 1.9 in. of displacement. When the unloading of the frame began, the dog bone load was still increasing, but at a very slow rate, while the frame continued to show negative loading.

As shown in figure 51, the locations where initial plasticity occurs for the two models are the same, occurring on the inner flange just above the outermost point. The baseline model shows plastic deformation at a displacement of 0.6 in. with a total load per frame per side of 27,000 lb. Using the as-tested material properties, the frame did not exhibit plasticity until 0.8 in. of enforced displacement and a total load per frame, per side of over 35,500 lb. The overall deflections in the frames in figure 51 are exaggerated by a factor of 10 to show that the inner flange was exhibiting some localized buckling.

At the point of maximum loading, the plastic region extended to include the web and outer flange of the frame above the original region of plasticity. The areas of plastic strain are shown in figure 52, and reflect the deformation of the structures at maximum total loading, just before unloading began. The frame deflections in the figure are actual scale and show clear deformations, particularly twisting of the inner flange of the frames, but also, an outward kinking of the structure below the dog bone. The amount of deformation observed is greater in the baseline model.

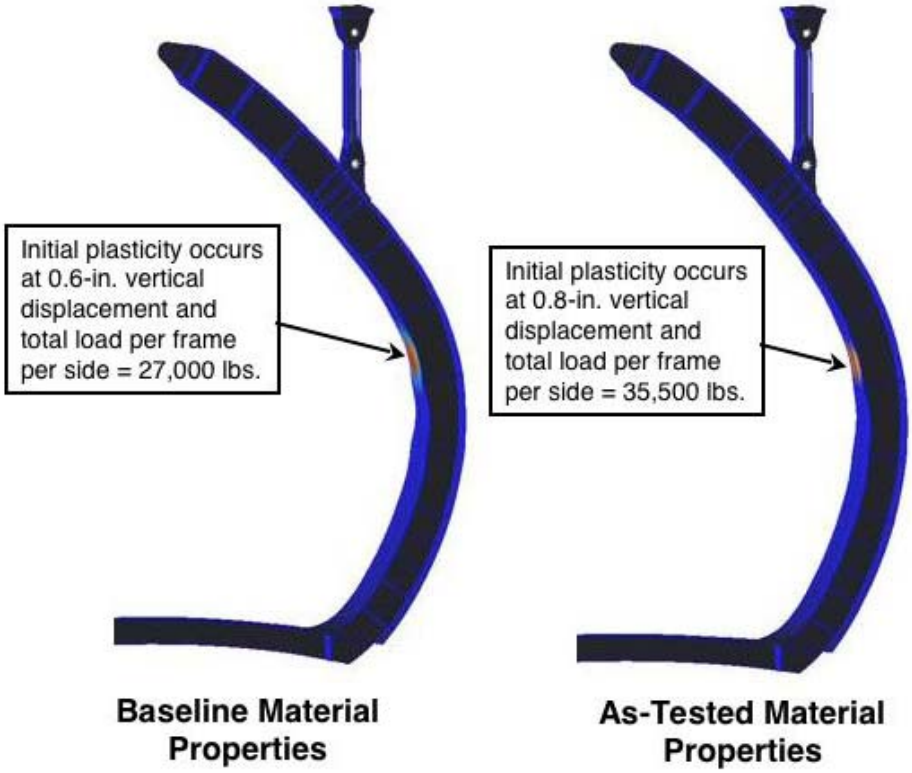

Figure 51. Initial Plasticity Locations in Upper Frames

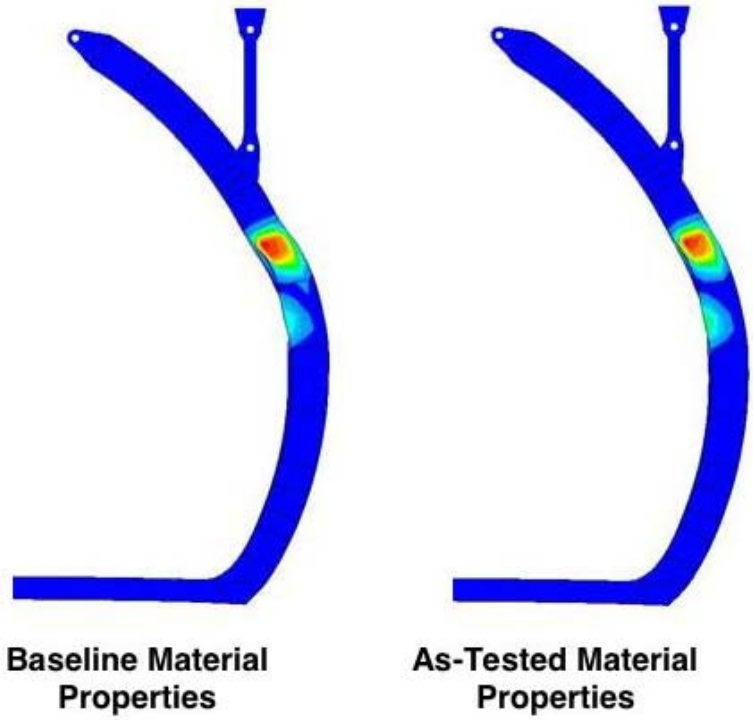

Figure 52. Plastic Strain at the Point of Maximum Loading

The progressive deformation and plasticity in the model with increasing enforced displacement, is shown in figures 53 and 54 for the baseline and as-tested models, respectively. The baseline model shows a significant kink in the frame below the dog bone attachment when the enforced displacement reaches 2.0 in. Note that in both figures the black line represents the outline of the frame model in its original position at 0.0 sec. The red region indicates areas where the maximum strain exceeded 10%. The model with as-tested material properties does not show such a dramatic kink as less of the frame is yielded, and it is yielded to a lesser degree, having a maximum strain of only 7.3%.

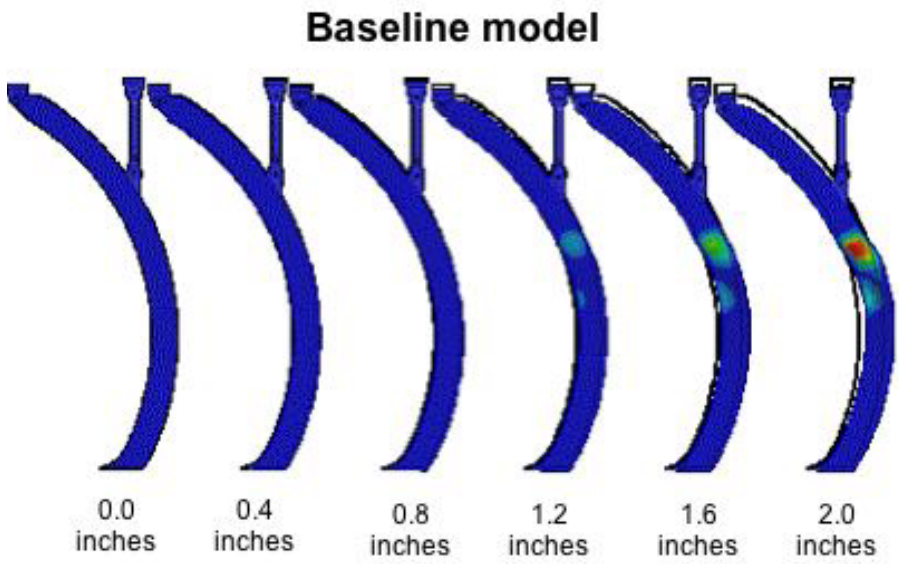

Figure 53. Deformations and Plastic Strain in the Fuselage Frame for the Baseline Model

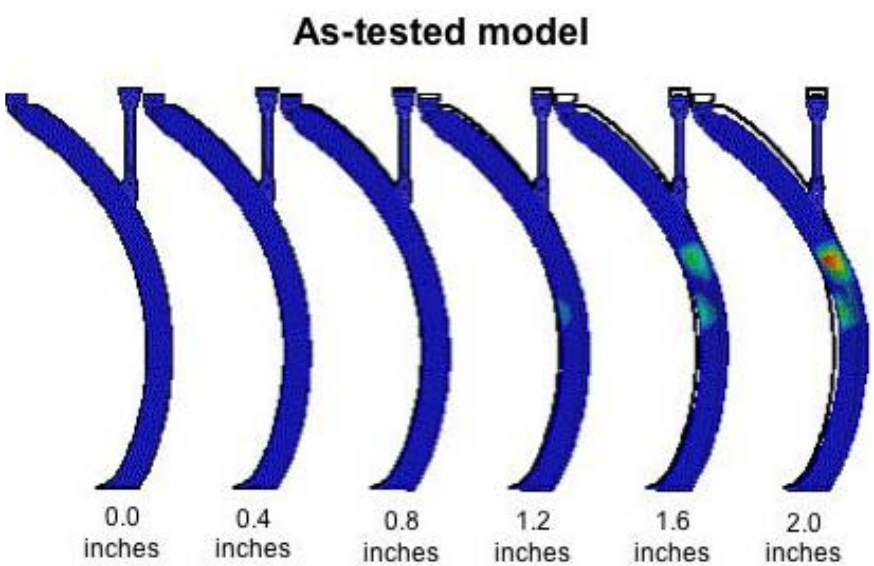

Figure 54. Progressive Deformations and Plastic Strains in the Fuselage Frame for the As-Tested Model

The von Mises stress distribution for the entire modeled structure (FS 25 frame is in front) is shown in figures 55 and 56 for the baseline and as-tested models, respectively. There is very little difference in the stress distribution of the FS 27 frame and the FS 25 frame since the differences between them lie in the length of the dog bones and the length of the fitting at the top of the frame. The areas of highest stress are the portions of the frame directly below the dog bones before the frames thicken at their base. The stress distribution in the lower frames, floor beams, and gearbox walls are not going to be as accurate as the upper frames because of the artificial boundary conditions applied to the model in those locations. In general, the stresses are lower in the baseline frames due to the greater amount of plastic deformation, which can also be seen in the increased amount of kinking in the frame.

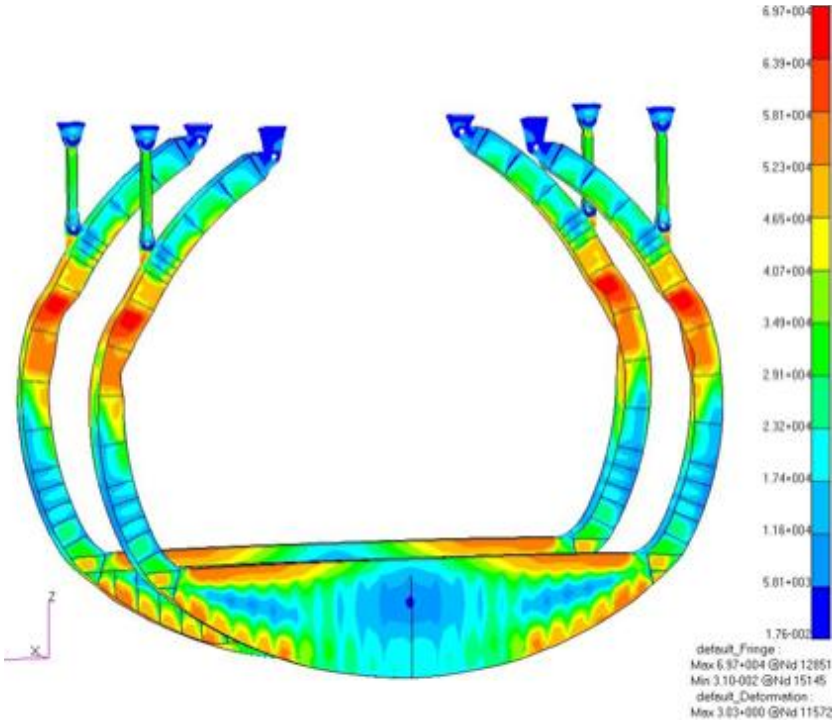

Figure 55. von Mises Stress Distribution of the Baseline Model at 2.0-in. Displacement

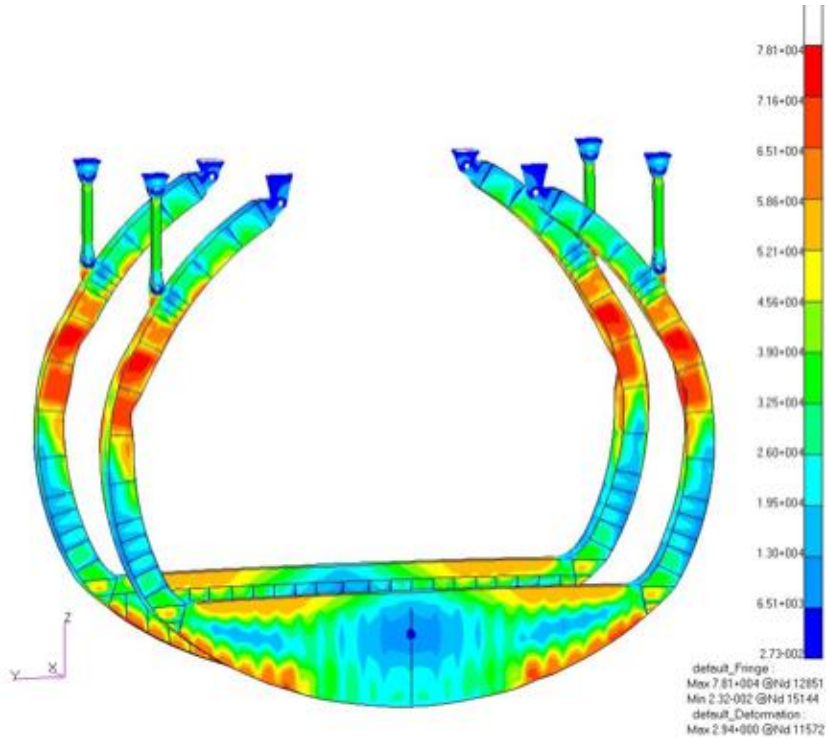

Figure 56. von Mises Stress Distribution of the As-Tested Model at 2.0-in. Displacement

6.3.3 Assessment of the NASTRAN Static Loads Analysis.

The development of the refined mesh, two-frame model of the wing support structure and the NASTRAN static loads analyses were performed for several reasons. The heavy fuselage frames at FS 25 and FS 27 were the primary load-bearing structure supporting the wing. During a vertical impact, these frames must react the dynamic loads imposed by the wing and fuel. Obviously, for this 30-ft/sec vertical drop test, the frames failed allowing the wing to displace vertically through the fuselage cabin. The NASTRAN two-frame model was much more refined than the original model. The mesh was two to four times more dense, and 362 section properties were used to define the changing thickness of the web and flanges of the frame. In addition, physical models of the frame and dog bone attachments to the wing were included. As shown in the force-displacement plots of figures 49 and 50, both NASTRAN models exhibited initial plasticity at an enforced vertical displacement between 0.6 and 0.8 in. with corresponding loading of between 27,000 and 35,500 lb. Note that the load values are given per frame per side. Thus, the total load required to deform the complete two-frame model is between 108,000 and 142,000 lb.

The NASTRAN model was executed with baseline material properties and with as-tested material properties. The properties are listed in table 4. Note that the ultimate failure strains were not input into the NASTRAN model. For the as-tested properties, the Young's modulus is about 4% higher, 10.8e06 psi compared with 10.4e06 psi. As shown in the plots in figures 49 and 50, the differences in elastic modulii did not influence the initial linear response. However, the differences in yield stress are more pronounced. The baseline model has a lower yield stress

and, consequently, will develop more plastic strain than the as-tested model for a given enforced vertical displacement. This behavior is shown in figures 53 and 54.

6.3.4 Development of an LS-DYNA Two-Frame Model.

An LS-DYNA dynamic loads analysis was performed for comparison with the NASTRAN static loads analysis. To perform this comparison, a comparable LS-DYNA model of the two-frame model had to be developed based on the original NASTRAN model. The LS-DYNA model was created by reading the NASTRAN model into MSC.Patran. The analysis preference within MSC.Patran was changed to LS-DYNA. Next, an upper block was added, along with an interface region between the upper block and the top of the frame and dog bone attachments. Two curved impact surfaces were added beneath each frame. The impact surfaces were curved to better match the constraints applied to the NASTRAN model. Next, the contact and initial velocity conditions were defined. For the LS-DYNA model, the initial velocity was set at 360 in./sec vertical velocity. Finally, the same nodal constraints used in the NASTRAN model to prevent fore-aft motion were applied to the LS-DYNA model. The as-tested material properties were used for the Al 7050-T7452. With these steps completed, an input deck was written and the model was executed using the SMP version of LS-DYNA 970. A three-quarter view of the LS-DYNA model is shown in figure 57(a), and a front view is shown in figure 57(b).

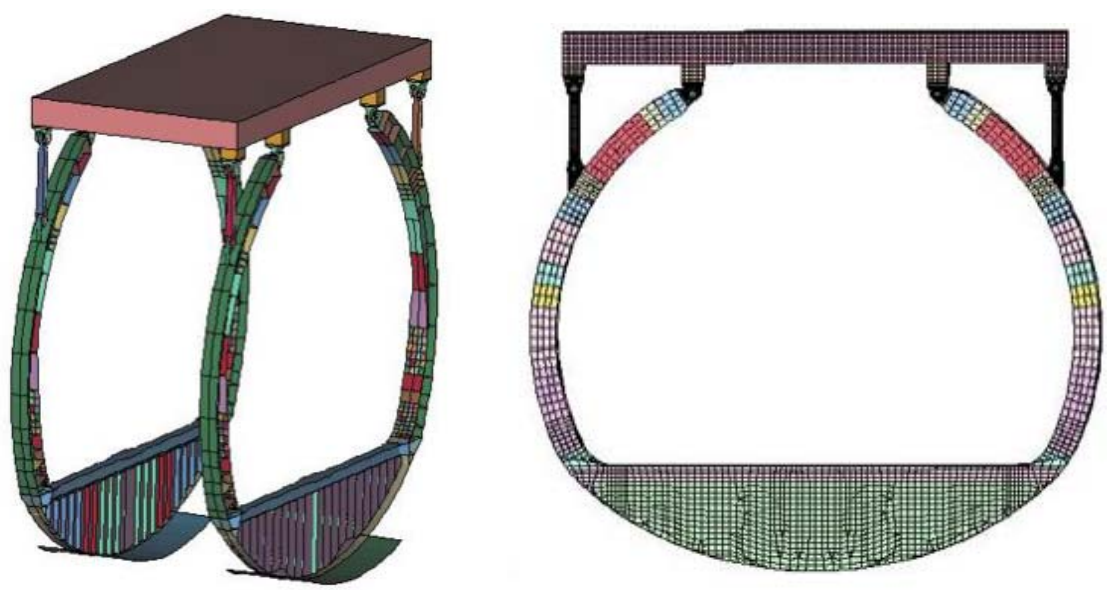

(a) Three-quarter view of model (b) Front view of model

Figure 57. Views of the LS-DYNA Two-Frame Model

The LS-DYNA two-frame model contained: 80,145 nodes, 88,976 elements, including 704 beam elements, 19,816 shell elements, and 68,456 solid elements. A total of 347 different parts were defined, the majority of which were used to represent the changing thicknesses of the frame web and flanges. Single-point constraints (SPC) were defined at 436 nodes in the model to represent the constraints used in the NASTRAN model to prevent fore-aft motion of the frames. A picture of the model with the constrained nodes (red dots) is shown in figure 58. The model was executed for 0.006 sec. The initial vertical velocity was 360 in./sec. Finally, the upper

block weighed 15,015 lb, which represented 8,700 lb of fuel and 6,315 lb for the wings and engines. Note that the longitudinal c.g. location of the upper mass is located exactly halfway between the frames. However, the measured c.g. location of the airplane is actually located halfway between FS 25 and FS 26, which is forward of the two-frame model c.g. by several inches. Finally, the LS-DYNA two-frame model was executed using the as-tested material properties, thus, only correlation with the as-tested NASTRAN model results is presented in the next section.

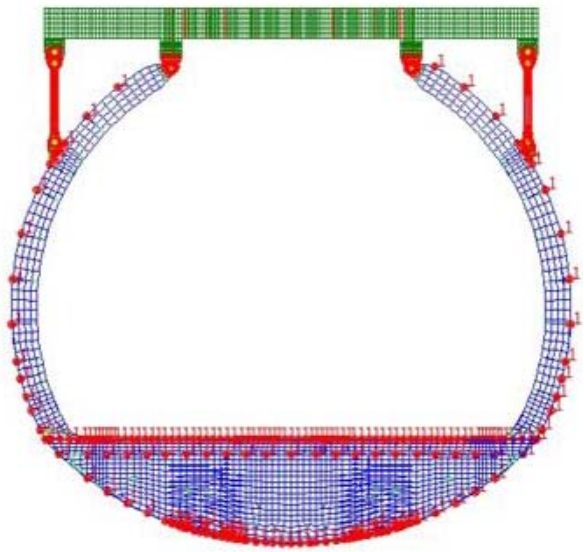

Figure 58. LS-DYNA Two-Frame Model Showing the Locations of Nodal Constraints

6.3.5 Results of the Dynamic Load Analyses.

The LS-DYNA two-frame model was initially executed for the same amount of time as the full airplane model (0.25 sec). However, since the primary purpose of the dynamic simulations was comparison with the static results, it was not necessary to execute the model for that length of time. A plot of vertical displacement versus time for a node located at the center of the bottom surface of the upper mass is shown in figure 59. The curve is linear up to 0.006 sec. Also, note that the upper block displaced 2 in. vertically, by 0.0056 sec. Since the maximum enforced deformation of the static model is 2 in., it is not necessary to execute the dynamic model for longer than 0.006 sec. Also, due to the linear relationship between displacement and time, it is possible to cross-plot various parameters to obtain plots of force versus displacement, etc.

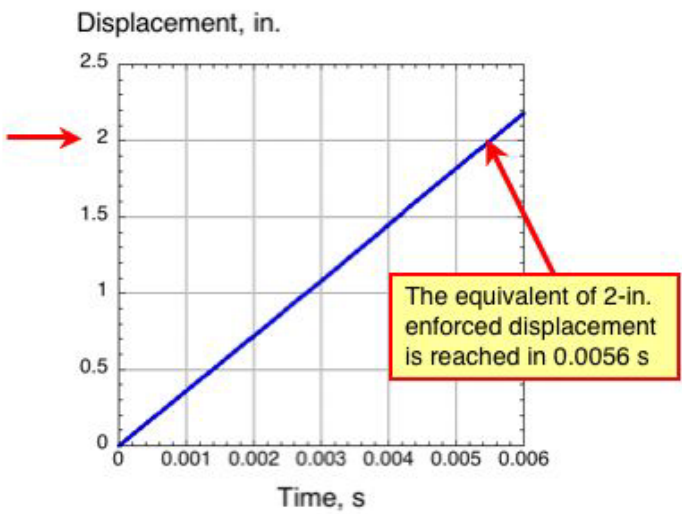

Figure 59. Displacement Time History of a Node Located at the Bottom Center of the Upper Mass

The results for initial and progressive plastic strain are presented next. The locations on the frames where initial plasticity, or yielding, occur are shown in figure 60. For both frames, initial plasticity occurs on the inner flange of the frame at a location approximately halfway between the top and bottom of the frame. For the LS-DYNA simulation, initial yielding occurred at 0.0025 sec, which corresponds to a vertical displacement of 0.9 in. In the NASTRAN model, initial yielding occurs at the same location, but at a vertical displacement of 0.8 in. Fringe plots of effective plastic strain are shown in figure 61. These plots show that plastic strain develops initially in the inner flange and web of the frames at a location just below the dog bone attachments. In addition, there is some indication of plastic strain at the location where the frame and floor intersects. These results match reasonably well with the plastic strain distributions shown in figures 53 and 54 for the NASTRAN static loads analysis.

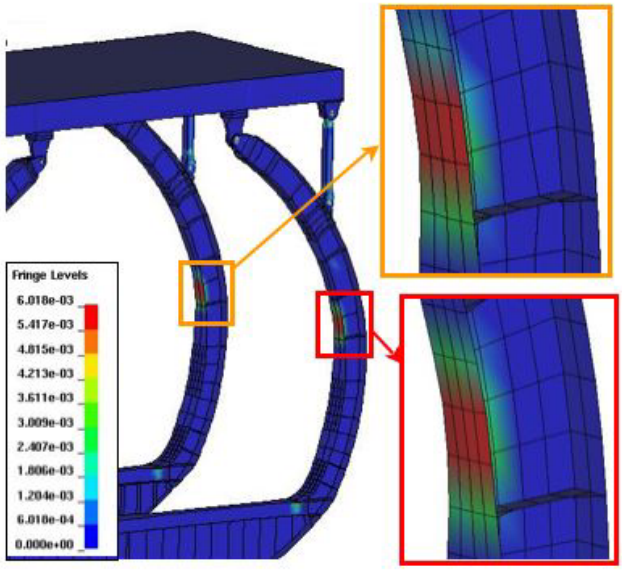

Figure 60. Location of Initial Plasticity in the LS-DYNA Two-Frame Model

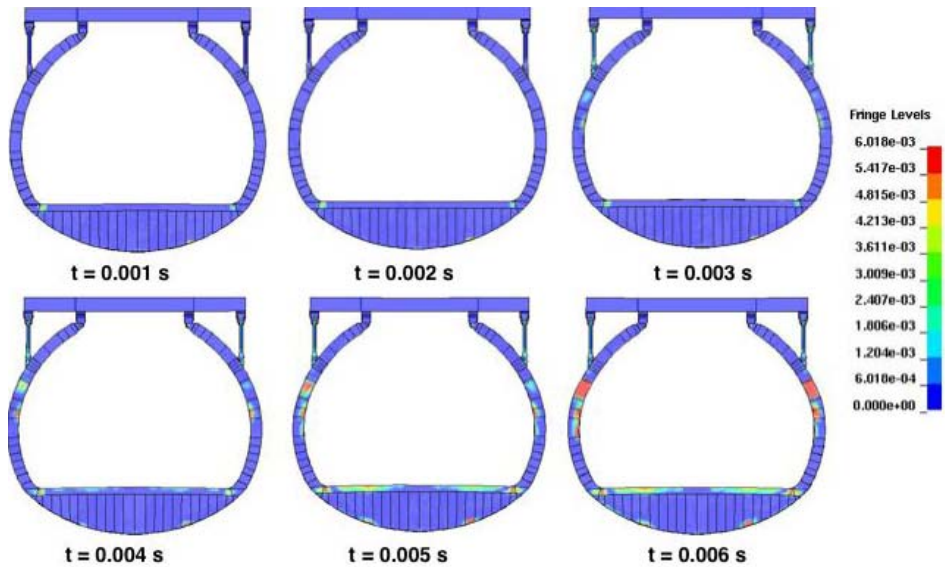

Figure 61. Fringe Plots of Effective Plastic Strain in the LS-DYNA Two-Frame Model

A comparison of the contact force time histories is presented next. A plot of contact forces at FS 25, FS 27, and a combined force (FS 25 plus FS 27) is shown in figure 62, along with another view of the model showing the location of the contact surfaces. The contact responses show a high initial peak force, then the force goes through zero, indicating a rebound. A second peak force comes next, though it is not as high in magnitude as the initial peak. Again, the force goes through zero, only to build up to a quasi-steady state level of the same magnitude as the second peak. The force responses at FS 25 and FS 27 are nearly identical, as expected, and the total force is essentially doubled the magnitude of the individual responses.

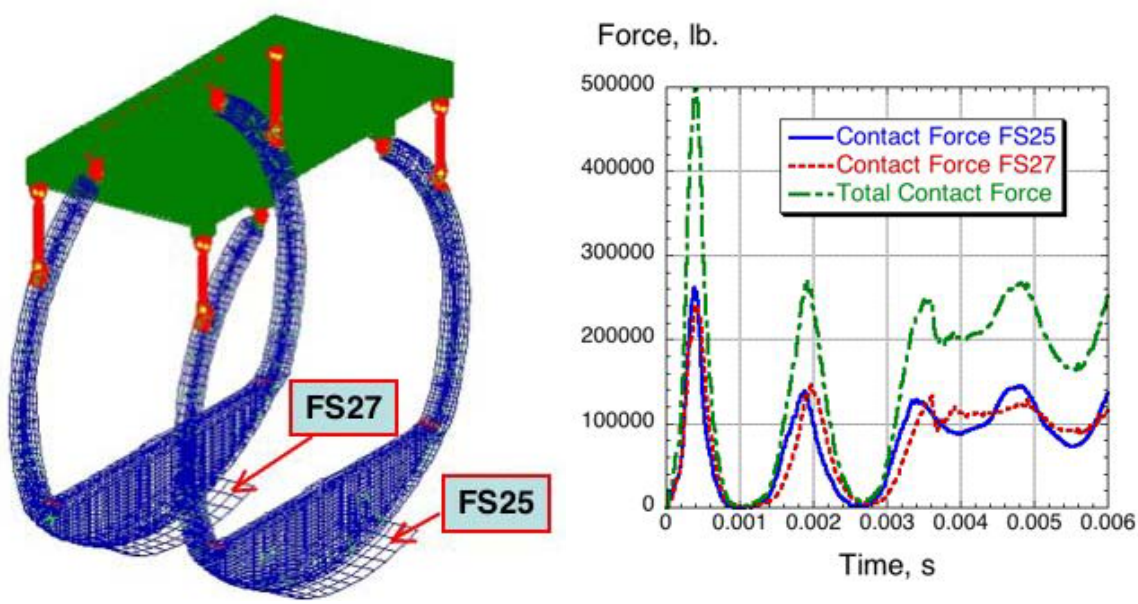

(a) Three-quarter view of the model (b) Predicted contact force time histories

Figure 62. Model Picture and Predicted Contact Force Time Histories at FS 25 and FS 27

A comparison of the predicted force responses in the dog bone and frame attachments is presented next. The forces for the LS-DYNA model were obtained in LS-PRE/POST using the S-plane feature. The frame and dog bone attachments were posted to the screen and, using the S-plane feature, a cutting plane was located at the base of the attachments. The force data was collected as a function of time, and a file containing the data was created by LS-PRE/POST. Comparisons of the LS-DYNA and NASTRAN force responses for FS 25 and FS 27 are shown in figure 63. The drawbacks of the method used to generate the force responses in LS-DYNA are that only as many points are generated as d3plot files are created. Generally, for a model of this size, between 50 and 100 d3plot files might be created. Also, the force data exhibits a sudden drop to zero when the model displaces completely through the cutting plane, as shown in figure 63(a).

The comparisons shown in figure 63 indicate an oscillatory response for the dynamic model, and a steady response for the static simulation. The attachments at FS 25 passed through the cutting plane by 0.003 sec, which accounts for the sudden drop in force. However, in general, the oscillatory response of the dynamic model bounds the static response. This finding was also true for the force response at FS 27, except that after 0.0035 sec, the dynamic response increased dramatically.

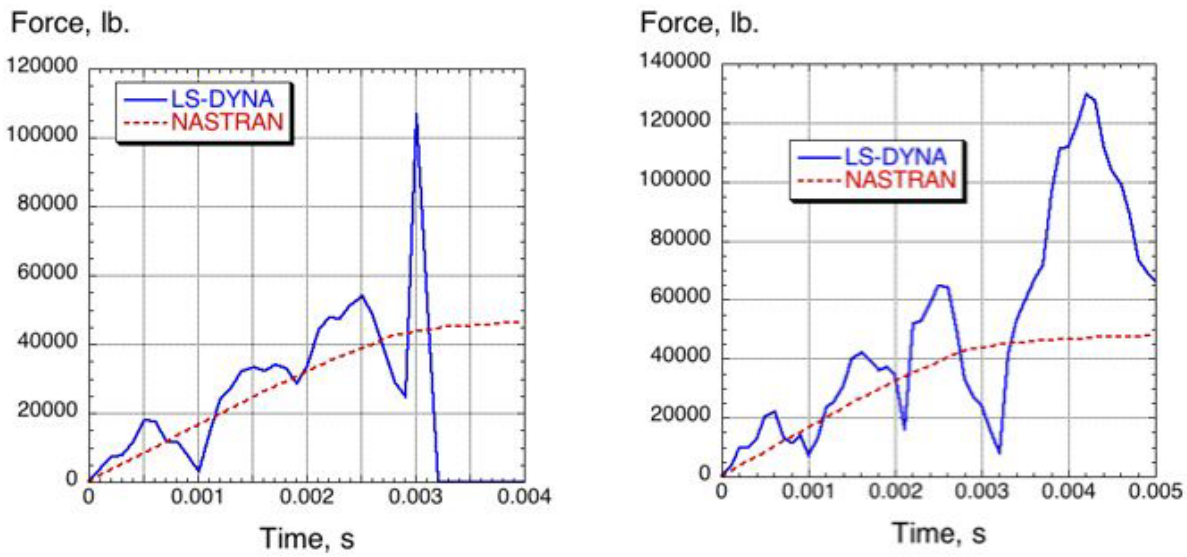

(a) Total vertical force response at FS 25 (b) Total vertical force response at FS 27

Figure 63. Total Vertical Force Responses of the Dog Bone and Frame Attachments at FS 25 and FS 27

Comparisons of the plastic strain states for equivalent vertical displacements of the NASTRAN and LS-DYNA models are shown in figure 64. The fringe plots are shown for a vertical displacement of 1.9 in. and the two figures are plotted for the same fringe range, i.e., dark red represents a strain level of 0.00121-in./in. The fringe plots are nearly identical, showing that the areas of highest plastic strain are just below the dog bone attachment. The LS-DYNA model does, however, show higher strain distributions in the floor region.

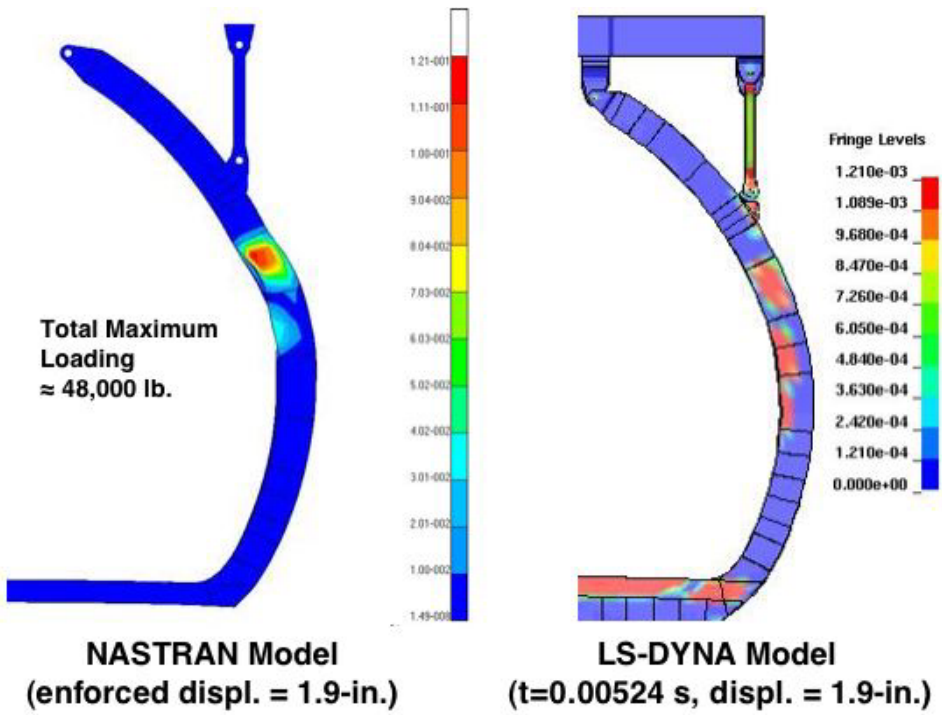

Figure 64. Comparison of Plastic Strain at Equivalent Vertical Displacement

As a final comparison between the static and dynamic simulations, fringe plots of the von Mises stress distributions in the two-frame models are shown in figure 65. The stress plots are shown at a vertical displacement of 2.0 in.. For the LS-DYNA model, a vertical displacement of 2.0 in. occurs at 0.0056 sec. The same fringe levels are used for both plots, with a maximum stress limit of approximately 78,000 psi. The colors of the NASTRAN plot are more vivid than those of the LS-DYNA plot; however, the stress distribution is similar. Note that the stress distribution in the floor, subfloor, gearbox, and lower fuselage frames will not be accurate due to the large number of constraints used in those areas. Both plots shown a large area of high stress located below the dog bone attachment.

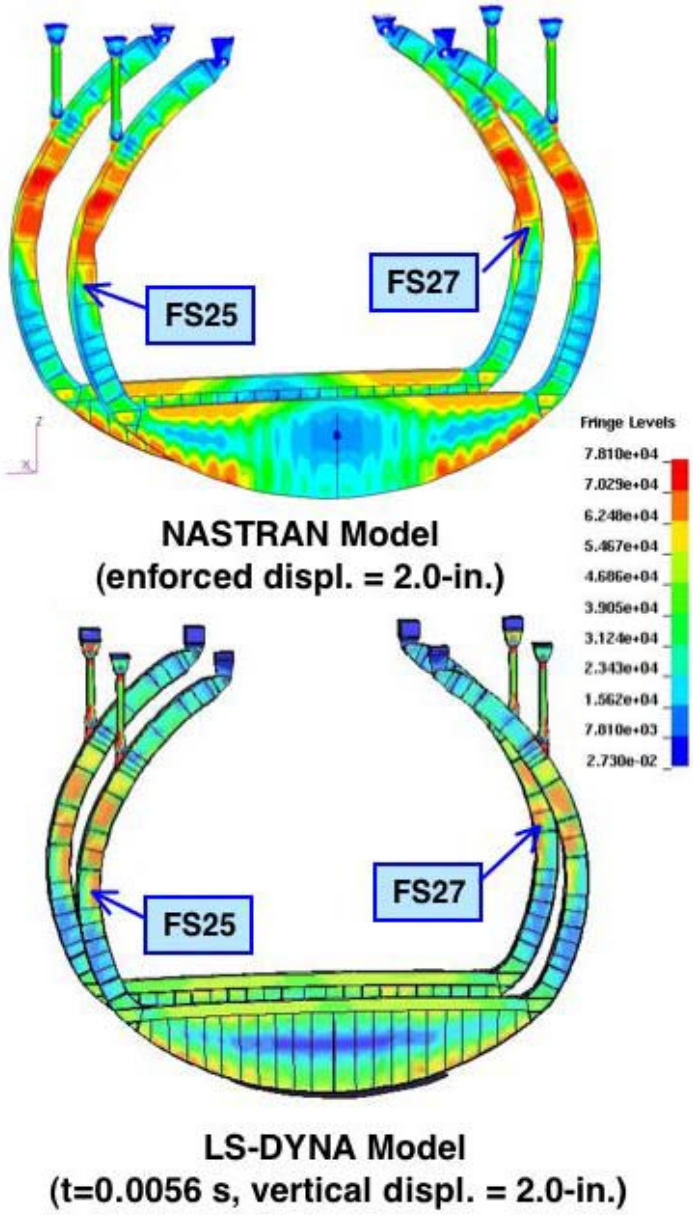

Figure 65. von Mises Stress Distributions in the NASTRAN and LS-DYNA Two-Frame Models

6.3.6 Parametric Study Using the LS-DYNA Two-Frame Model.

As an interesting parametric study, the initial impact velocity of the LS-DYNA two-frame model was halved from 360 in./sec to 180 in./sec and then halved again to 90 in./sec. Results of the reduced impact velocity simulations were compared with the results from the 360-in./sec model. The run times for the two models with reduced velocity were increased to achieve equivalent vertical displacement as the model. A plot of displacement versus time for the three models is shown in figure 66(a). These responses were obtained from a node located at the center of the bottom surface of the upper block. The data shown for the 360-in./sec model is the same as plotted in figure 59. The response is completely linear up to 0.006 sec, which is the termination

time of the model. The 360-in./sec model crosses 2 in. of vertical displacement at 0.0056 sec. The displacement response for the model in which the velocity is halved to 180 in./sec is slightly nonlinear and crosses 2.0 in. at 0.012 sec. Finally, for the model in which the velocity was reduced to 90 in./sec, the response curve is highly nonlinear and does not achieve 2.0 in. of vertical displacement, but instead, reaches a maximum displacement value of 1.61 in. by 0.03 sec, the termination time of the model.

A plot of the total contact force (FS 25 force plus FS 27 force) for the three impact velocity scenarios is shown in figure 66(b). As expected, the higher the impact velocity, the larger the initial spike in the contact force. As the velocity is decreased to 180 in./sec, the large spike is reduced substantially. For the simulation at 90 in./sec, no spike is evident. Also, the number and magnitude of the oscillations in the response is reduced. For the 90 in./sec scenario, the oscillations are almost entirely alleviated, and the response is relatively smooth. The explanation for this trend is that the inertial forces are reduced as the velocity is lowered. Obviously, for correlation with a static simulation, the dynamic simulation performed at a lower-impact velocity would give more accurate results.

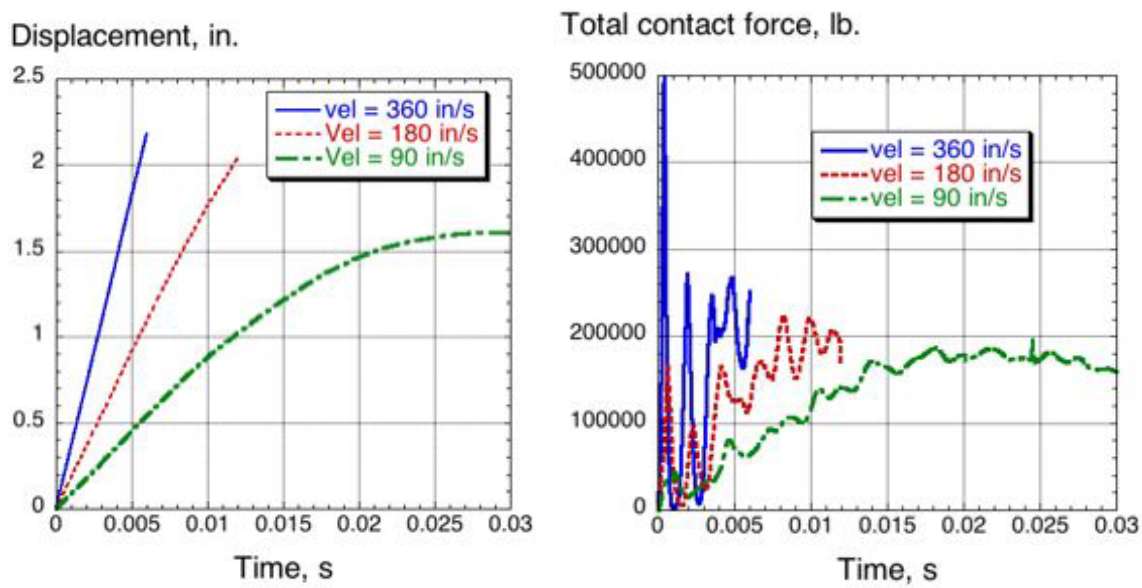

(a) Displacement versus time results (b) Total contact force versus time results

Figure 66. Results of the LS-DYNA Simulations at Three Impact Velocities

6.3.7 Assessment of the LS-DYNA Two-Frame Model.

The NASTRAN refined mesh model of the frame sections located at FS 25 and FS 27 was uploaded into MSC.Patran and converted into an LS-DYNA model. Curved impact surfaces were added, along with contact definitions. An upper mass representing the weight of the wing, fuel, and engines was added and nodal constraints were applied to prevent fore-aft motion of the frames. The model was assigned the as-tested material properties and an initial velocity of 360 in./sec. Since the NASTRAN model was executed for a maximum enforced vertical displacement of 2.0 in., the LS-DYNA model was executed for only 0.006 sec, given that the vertical displacement of the upper block reached 2.0 in. by 0.0056 sec. For perspective, it is

interesting to note that the vertical displacement of node 20931, located at the bottom center of the wing reached a maximum vertical displacement of 39 in. at 0.22 sec, as indicated in figure 22.

In general, the LS-DYNA model compared well with the static results. For example, initial yielding occurs at 0.0025 sec in the LS-DYNA model, which corresponds to a vertical displacement of 0.9 in. In the NASTRAN model, initial yielding occurs at the same location, but at a vertical displacement of 0.8 in. This slight discrepancy may be attributed to the gap between the model and the impact surfaces (1/8 in.). This gap was used to prevent initial penetration of the model and the impact surface, but it meant that the model has to travel the gap distance in the vertical direction before contact was recognized. This dynamic simulation demonstrates the usefulness of performing a static analysis to quantify areas of high stress and likely failure in the model. It is also useful to note that the NASTRAN model executed in a few minutes, whereas the LS-DYNA model required 4.5 hours of execution time.

One recommendation for future work is to exercise the implicit solver available in LS-DYNA to execute a quasi-static simulation of the two-frame model. Unlike explicit time integration, which requires many small time steps, the implicit time integrator permits a few large time steps. For a quasi-static analysis, time represents a monotonically increasing parameter, which characterizes the evolution of the loading.

6.4 MESH REFINEMENT STUDY.

As a final model improvement, the refined mesh model of the heavy fuselage frames at FS 25 and FS 27, including physically accurate models of the dog bone and upper attachments, was incorporated into the full airplane finite element model and a mesh refinement study was conducted. Combining the two models required considerable editing and remeshing. For example, in the full airplane model, all elements and nodes in the section of the model between FS 24 and FS 28 were removed, including the outer skin, stringers, floor beams, gear box, and fuselage frames. Only the wing was excluded. Then, the refined mesh models of FS 25 and FS 27 were imported into the airplane model. The fuselage frame at FS 26 was recreated by transforming the appropriate elements in FS 25 to the correct location. Thus, the fuselage frame at FS 26 had the same mesh density as the frames at FS 25 and FS 27. The refined mesh model of these three fuselage frames, along with the dog bone and upper attachments, are shown in figure 67. Next, a transition mesh was created to connect the refined mesh region with the coarser mesh at FS 24 and FS 28. Finally, an interface mesh, consisting of mostly solid elements, was created to connect the dog bone and upper attachments to the bottom skin of the wing. This region of the model is shown in figure 68. The material properties used in this simulation were the same as those used in the original model, as specified in table 1. All other parameters within the model were unchanged from the original simulation.

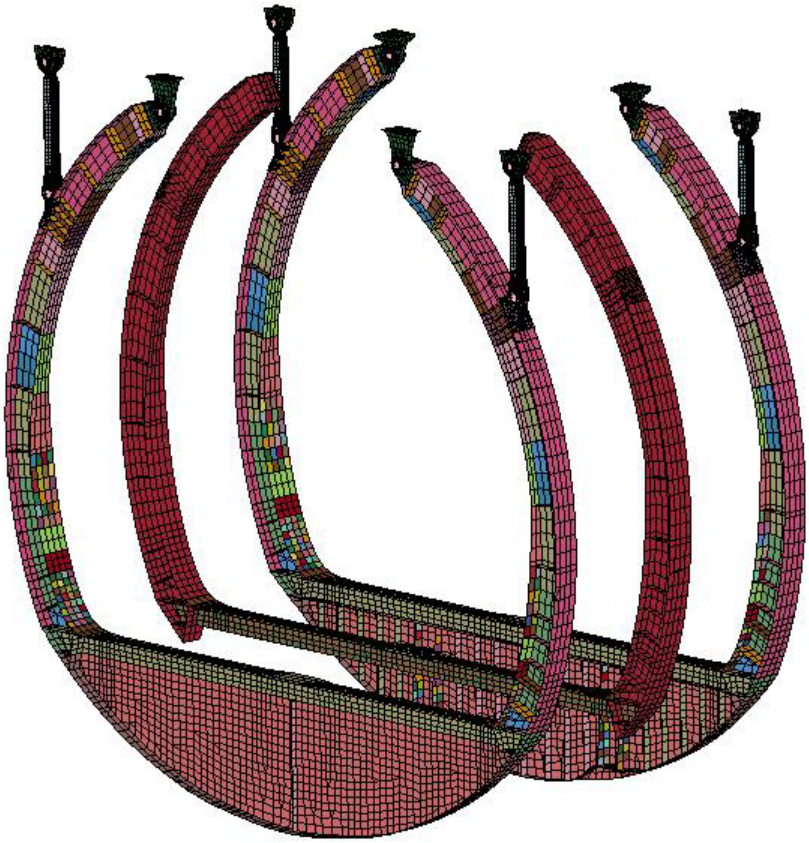

Figure 67. Refined Mesh Model of Fuselage Frames at FS 25, FS 26, and FS 27 With Attachments

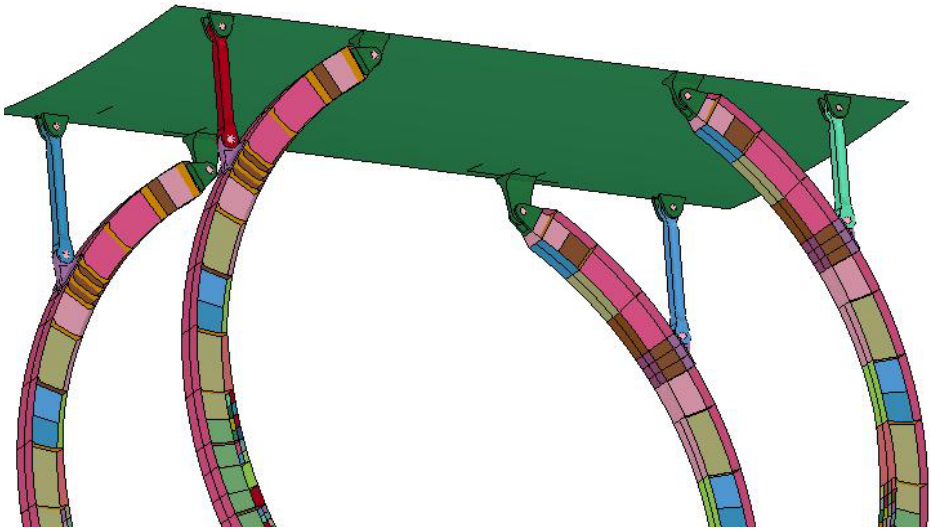

Figure 68. Frame Attachments to the Bottom Skin of the Wing

The final, refined mesh model of the ATR 42 airplane is depicted in figure 69. The model consisted of 77,318 nodes, 102,788 elements including 85,600 shell elements, 14,319 solid elements, 1,190 beam and/or rod elements, and 1,679 point-mass elements. The elements were

grouped into 391 different part definitions, most of which were used to define different thicknesses in the heavy fuselage frames located at FS 25 and FS 27. A comparison of the inertial properties of the test article, the original model, and the refined mesh model is provided in table 5. The model was executed using the SMP version of LS-DYNA v. 971 for 0.3 sec of simulation time on an HP workstation xp8200 and required 367 hours of CPU.

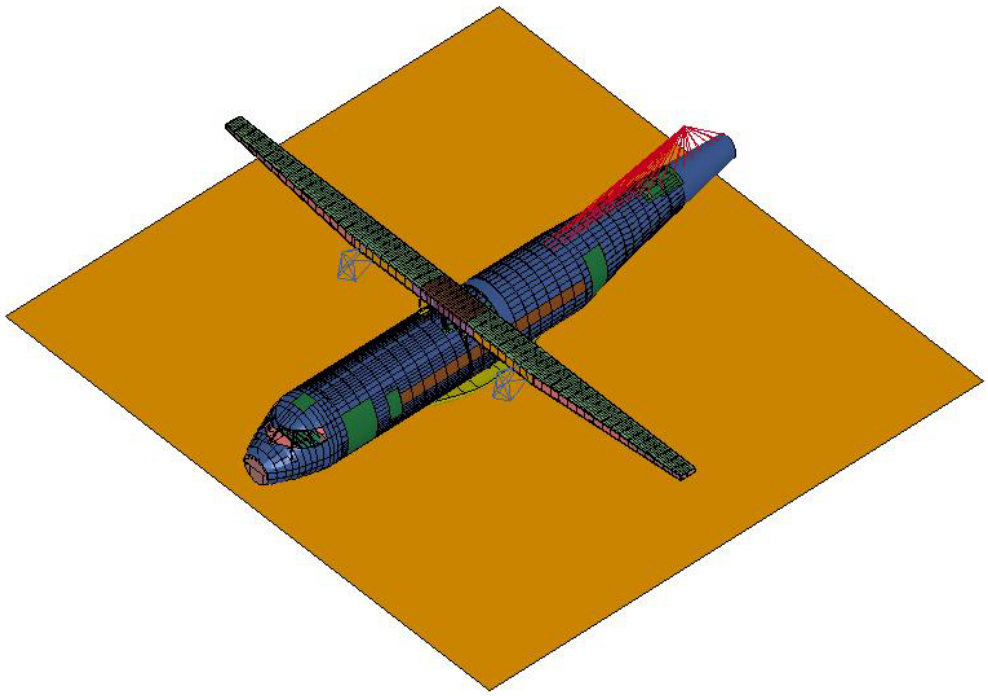

Figure 69. Refined Mesh Model of the ATR 42 Airplane

Table 5. Comparison of Inertial Properties

c.g. location	Test Article (33,200 lb)	Original Model (33,120 lb)	Refined Mesh Model (33,814 lb)
x (in.)	469.2	471.7	469.5
y (in.)	-	0.24	0.34
z (in.)	-	142.6	143.3

The results of the refined mesh simulation are discussed in sections 6.4.1 and 6.4.2.

6.4.1 Structural Deformation.

A comparison of structural deformation of the test article and the refined mesh model for five discrete time steps is shown in figure 70. For comparison with the original model, see figure 9. The deformation of the refined mesh model more closely matches that of the test article than does the original model. Specifically, the refined mesh model exhibits greater intrusion of the wing into the fuselage cabin area, and the wing exhibits a forward (pitching) rotation that is observed in the test article. This forward rotation of the wing was not seen in the original model, partly because SPCs were used to ensure vertical alignment of the wing attachment structure.

Thus, the wing was partially constrained as well. No nodal constraints were used in the refined mesh model.

Time (sec)	Test Article	Refined Mesh Simulation
0.05		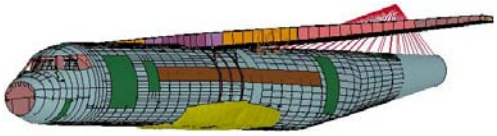
0.10		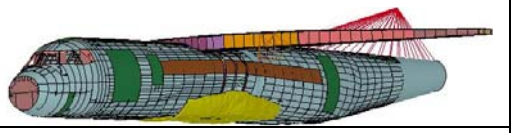
0.15		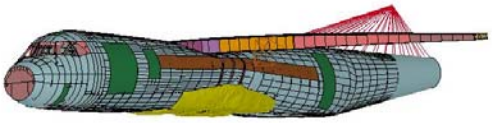
0.20		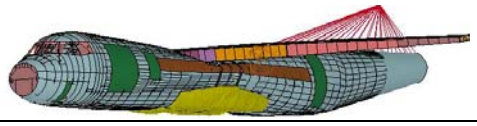
0.25		

Figure 70. Structural Deformation of ATR 42 and Refined Mesh LS-DYNA Model

The influence of the nodal constraints is evident in figure 71, which shows the wing support structure and fuselage frames at FS 25 and FS 27 at times equal to 0.0 and 0.25 sec for the original and refined mesh models. For the original model, the orientation of the dog bone attachments is maintained in the vertical direction by nodal constraints. Dynamic loading is transferred from the wing into the fuselage frames and produces multiple failures of the frames. The fuselage frame failure patterns at FS 25 and FS 27 are similar. In comparison, the dog bone attachments in the refined mesh model are not constrained and are free to move as forces dictate. For this model, much greater vertical deformation is observed. The dog bone attachments remain attached; however, they are essentially pushed aside, most likely due to the defined contact as the wing deforms and crushes the fuselage frames underneath. Also shown in figure 71, the damage to the fuselage frame at FS 25 is considerably more severe than that exhibited by the fuselage frame at FS 27. One explanation is that the wing is now free to rotate forward about its transverse axis. As it does so, greater loading is applied to the forward fuselage frame, resulting in more damage and greater deformation of that frame. Although it is difficult to discern in the deformed picture of figure 71, the fuselage frame at FS 25 has displaced vertically by 10 in. more that the fuselage frame at FS 27 for the refined mesh model.

Another indication that the refined mesh model is providing a more accurate simulation of structural deformation is to examine the displacement of the wing. As mentioned earlier, an accelerometer was located at the center of the bottom skin of the wing. This location in the model is shown in figure 22(a). The accelerometer data were integrated twice to obtain the vertical displacement time history response of the wing, as plotted in figure 72. Also, the displacement time history response of Node 20931 was output from the original and refined mesh models, and these curves are plotted versus the test data in figure 72. Obviously, the refined mesh model shows much better agreement with the experimental response than does the original model. In fact, the model exactly predicts that the wing displaces 50 in. at 0.25 sec. The model also predicts that the maximum displacement of the wing (51.2 in.) occurs shortly afterward at 0.29 sec.

.

Model	Time = 0.0 s	Time = 0.25 s
Original Model	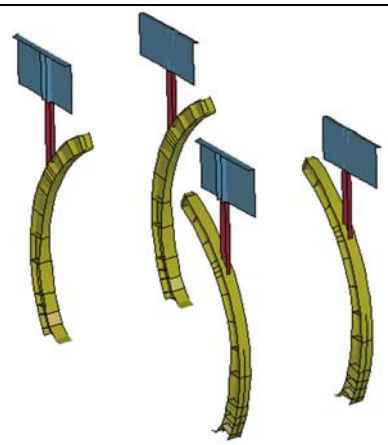	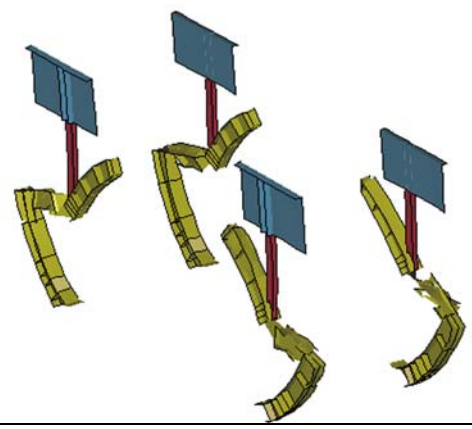
Refined Mesh Model	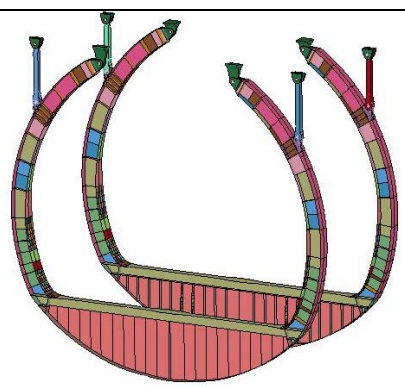	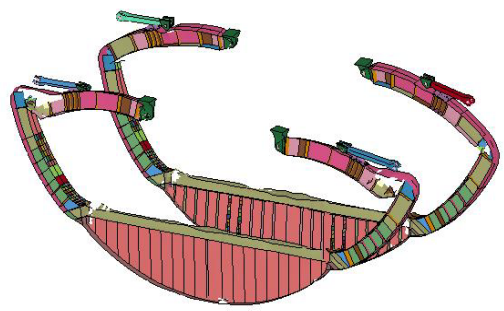

Figure 71. Predicted Structural Deformation of the Original and Refined Mesh LS-DYNA Models

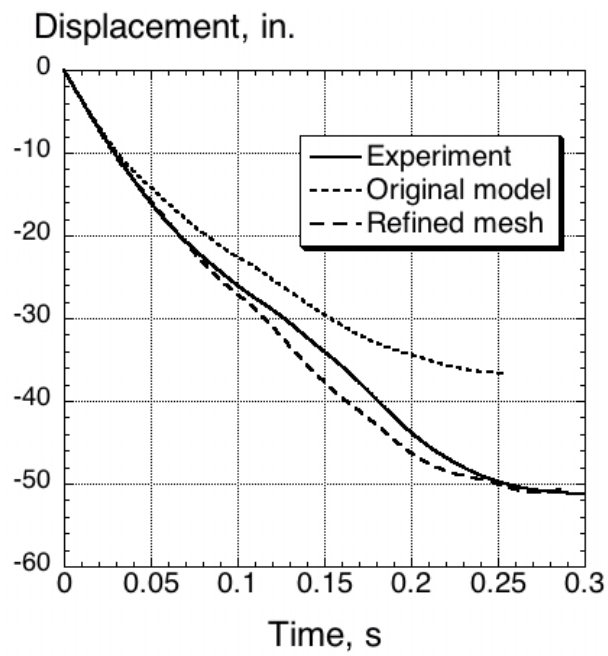

Figure 72. Test and Analysis Displacement Time History Responses of the Bottom Center of the Wing

6.4.2 Test and Analysis Correlation.

The experimental acceleration and velocity responses for the left outer floor track at FS 20 are plotted versus the predicted responses from the original and the refined mesh models, as shown in figure 73(a) and (b), respectively. Note that the experimental and analytical accelerations were filtered using a low-pass digital filter with a cut-off frequency of 33.2 Hz. This filter is equivalent to CFC20. The experimental velocity was obtained by integrating the filtered acceleration data, and the analytical responses were output directly from the LS-DYNA simulation. For this location, very little difference in the acceleration or velocity responses was observed between the original and the refined mesh models. This finding was not surprising since few, if any, changes were made in this region of the model.

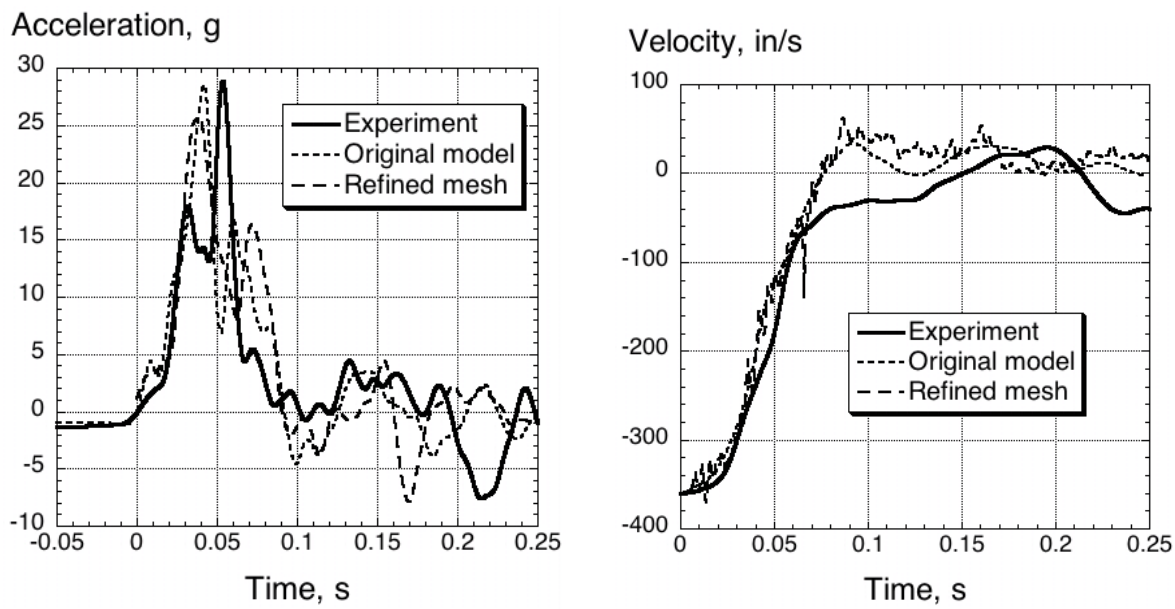

(a) Acceleration responses (b) Velocity responses

Figure 73. Test Analysis Correlation Responses for the Left Outer Floor Track at FS 20

The experimental acceleration and velocity responses for the right outer floor track at FS 18 are plotted versus the predicted responses from the original and the refined mesh models, as shown in figure 74(a) and (b), respectively. At this location, the refined mesh model slightly overpredicts the peak acceleration, i.e., 27 versus 24 g's. However, almost no differences are seen in the velocity responses.

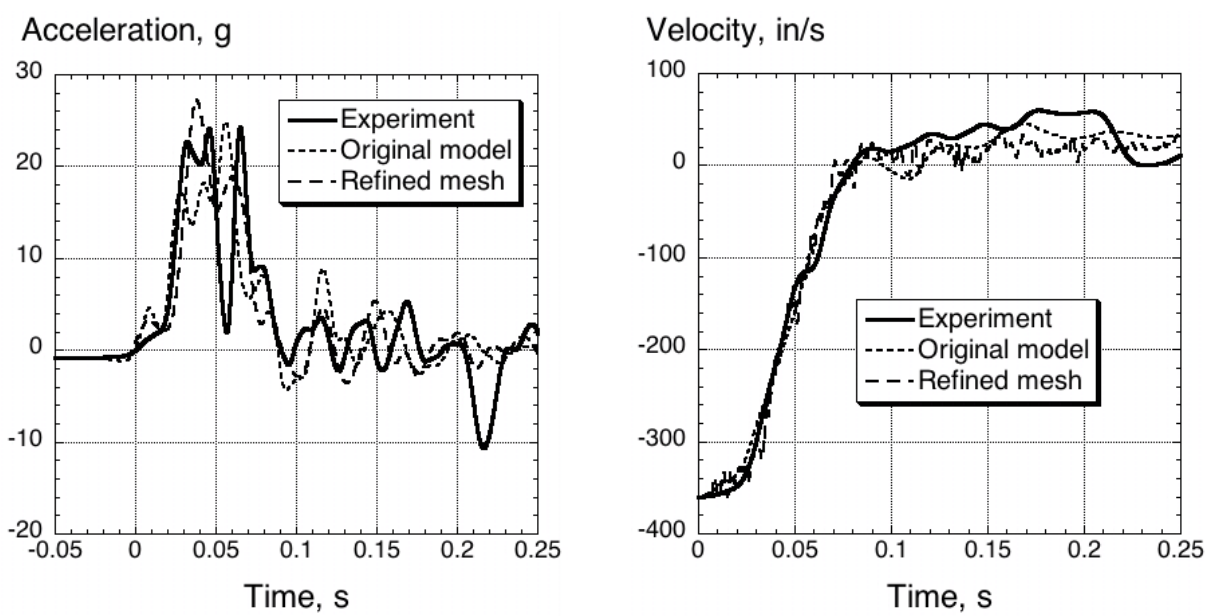

(a) Acceleration responses (b) Velocity responses

Figure 74. Test Analysis Correlation Responses for the Right Outer Floor Track at FS 18

The experimental acceleration and velocity responses for the right side of the cockpit floor are plotted versus the predicted responses from the original and the refined mesh models, as shown in figure 75(a) and (b), respectively. At this location, the refined mesh model did a better job of predicting the peak acceleration (34 g's for the test and 32 g's for the refined mesh model compared with 26 g's for the original model). However, the onset rate of the acceleration response was not well predicted. The refined mesh model did a better job at predicting the time when the experimental velocity response crossed zero. In general, both models predicted the amount of rebound velocity accurately.

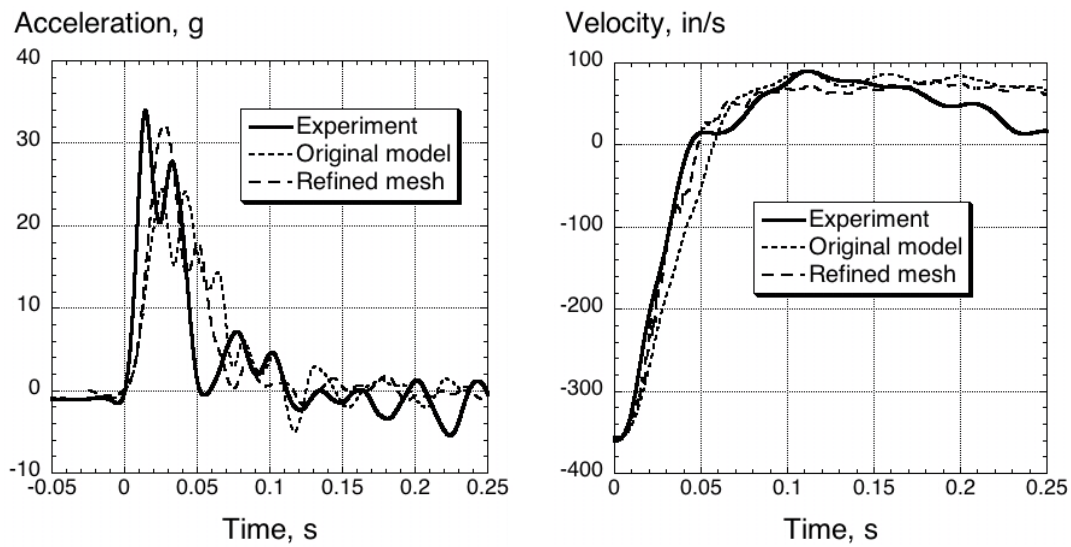

(a) Acceleration responses (b) Velocity responses

Figure 75. Test Analysis Correlation Responses for the Right Side of the Cockpit Floor

The experimental acceleration and velocity responses for the left inner floor track at FS 29 are plotted versus the predicted responses from the original and the refined mesh models, as shown in figure 76(a) and (b), respectively. In general, at this location, the refined mesh model did not improve the correlation level. The refined mesh model overpredicted the peak acceleration. Also, the time when the model crossed zero velocity was much earlier than for the test or the original model, and the refined mesh model exhibited a higher rebound velocity.

The experimental acceleration and velocity responses for the right inner floor track at FS 35 are plotted versus the predicted responses from the original and the refined mesh models, as shown in figure 77(a) and (b), respectively. At this location, the acceleration response of the refined mesh model exhibits a highly oscillatory response and generally overpredicts the magnitude of both the experimental and original model responses. The velocity response is, however, much smoother and allows some assessment of correlation. As indicated in figure 77(b), the velocity responses of both the original and refined mesh models are quite similar. Both responses cross zero velocity much earlier than does the experimental response. It is unclear why the refined mesh model would exhibit the oscillatory acceleration response at this location, especially since few changes were made to the model at this location.

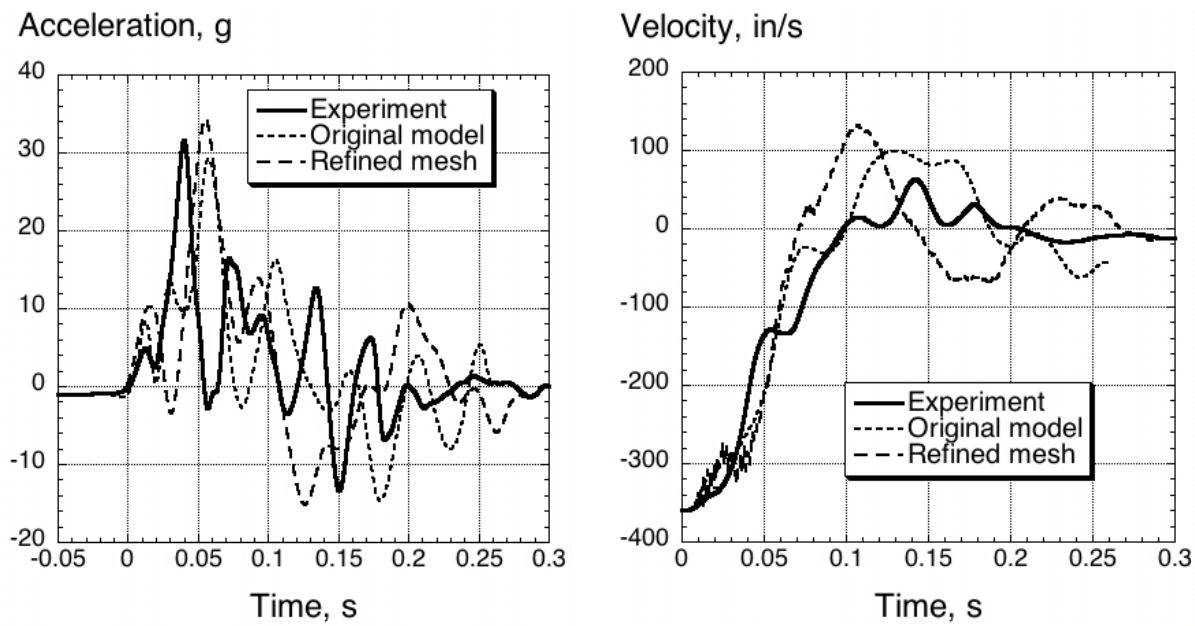

(a) Acceleration responses (b) Velocity responses

Figure 76. Test Analysis Correlation Responses for the Left Inner Floor Track at FS 29

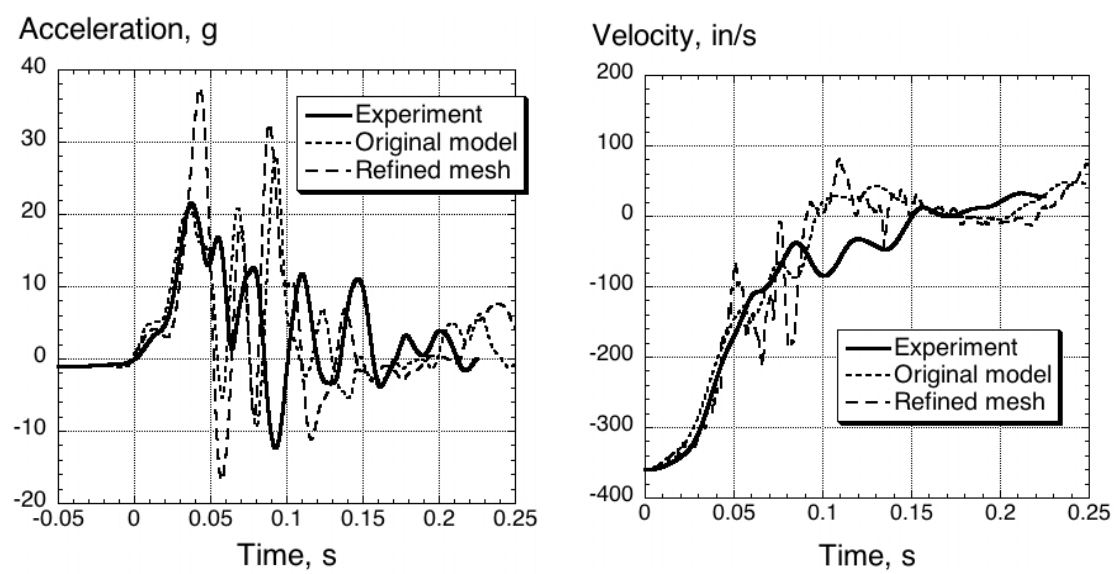

(a) Acceleration responses (b) Velocity responses

Figure 77. Test Analysis Correlation Responses for the Right Inner Floor Track at FS 35

The experimental acceleration and velocity responses for the center tail section at FS 47 are plotted versus the predicted responses from the original and the refined mesh models, as shown in figure 78(a) and (b), respectively. Both analytical models predict the experimental acceleration and velocity responses accurately at this location. The refined mesh model shows a higher rebound velocity than predicted by the original model or exhibited by the test data. Again, few changes were made to the model in this region.

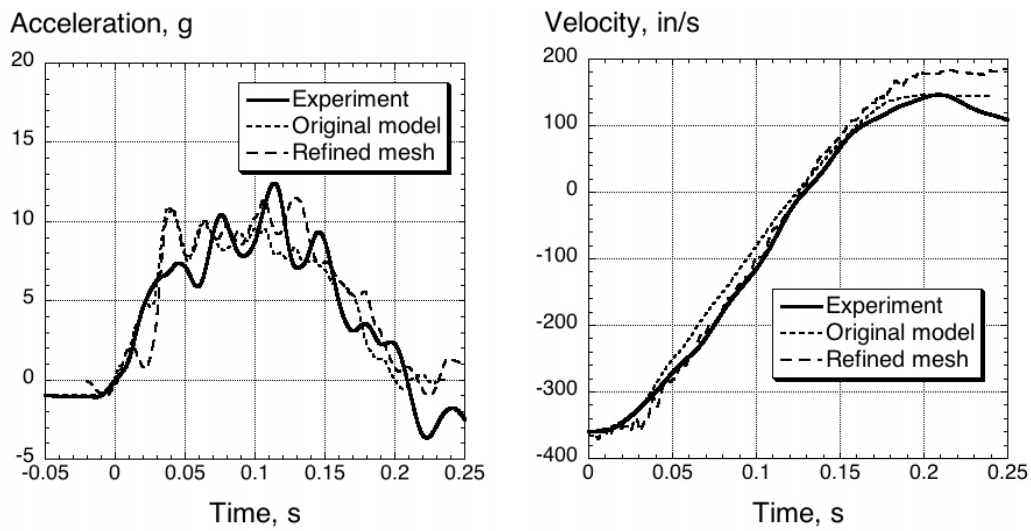

(a) Acceleration responses (b) Velocity responses

Figure 78. Test Analysis Correlation Responses for the Center Tail Section at FS 47

The experimental acceleration and velocity responses for the left sidewall at FS 18 are plotted versus the predicted responses from the original and the refined mesh models, as shown in figure 79(a) and (b), respectively. Both predicted acceleration and velocity responses match the experimental data quite well. In general, the refined mesh model overpredicts the peak acceleration and exhibits a more oscillatory response than seen in the original model or the test data. Both analytical curves match the initial velocity response well, up to the time at which the experimental response crosses zero velocity. The predicted responses cross zero velocity earlier than the experimental response.

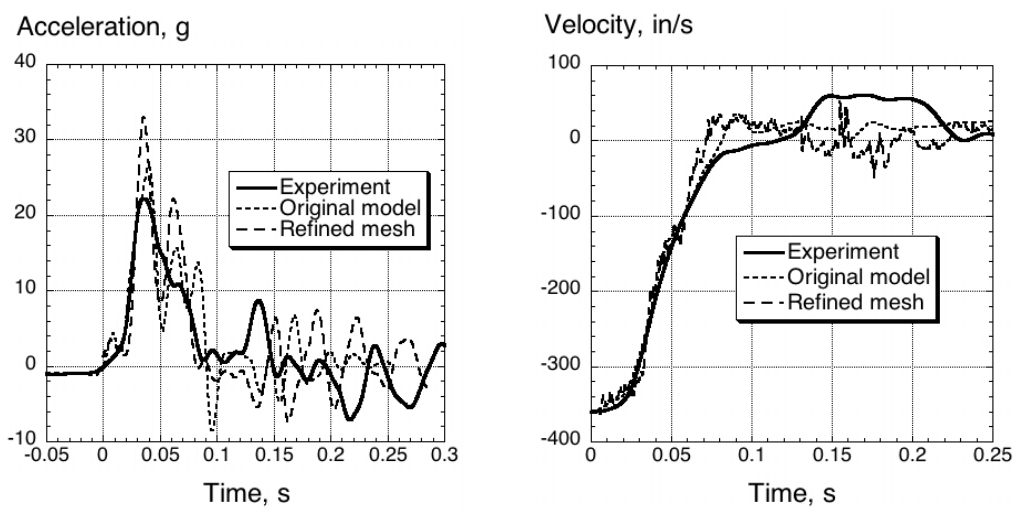

(a) Acceleration responses (b) Velocity responses

Figure 79. Test Analysis Correlation Responses for the Left Sidewall at FS 18

The final time history comparison is shown in figure 80, where the experimental acceleration and velocity responses for the center of the bottom skin of the wing at FS 26 are plotted versus the

predicted responses from the original and the refined mesh models. At this location, the refined mesh model shows better correlation with the experimental acceleration and velocity responses. A lower peak acceleration is predicted and the stairstep appearance of the experimental velocity curve is well predicted, as shown in figure 80(b).

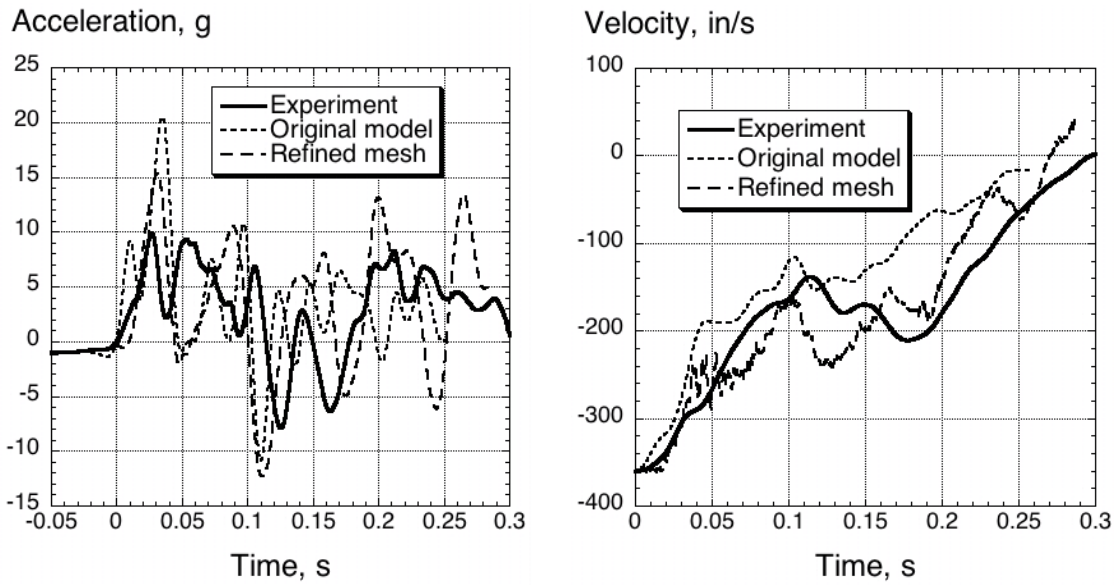

(a) Acceleration responses (b) Velocity responses

Figure 80. Test Analysis Correlation Responses for the Bottom Center of the Wing at FS 26

6.4.3 Assessment of the Refined Mesh Model.

The work that went into refining the mesh of the original airplane model was rewarded with improvements in test analysis correlation. The refined mesh model included not only a more detailed and physically accurate model of the heavy wing support frames, but also included an accurate physical model of the wing attachment hardware. By removing the nodal constraints, the model was able to predict the forward (pitching) rotation of the wing. Also, as shown in figures 72 and 80, improved correlations with the acceleration, velocity, and displacement responses of the wing were achieved.

Unfortunately, the improved correlation came at a large computational expense. The refined mesh model was executed for 0.3 sec, which required 367 hours (approximately 15 days) of CPU. The original model was executed for a termination time of 0.25 sec. The reason for the longer run time was to fully capture the wing displacement response. Note from figure 72 that the wing did not reach maximum vertical displacement until 0.29 sec.

7. DISCUSSION OF RESULTS.

This report describes the results of a multiyear research project to develop a finite element model of the ATR 42 airplane, to perform transient dynamic simulations using LS-DYNA, to validate the model through test analysis correlation, and to implement several changes to the model to improve the correlation. The original model was created from six different Patran database files

that contained overall dimensions and some details of the interior structure. These six database files were generated from hand measurements of the airframe. As the database files were received from the FAA, a master geometry database file was created, and new information was added as-received. This method of creating the original model was not ideal, and resulted in several problems, including a large number (5400 +) of nodal discontinuities in the model, a relatively coarse mesh of the airplane overall, and the lack of structural details in certain areas of the model. A better method of model development would have been converting a pre-existing model, such as a NASTRAN structural or modal analysis model, into a dynamic impact model. Other possibilities are to create the LS-DYNA model from existing computer-aided design (CAD) models. Unfortunately, no pre-existing NASTRAN or CAD models were available.

Despite the problems with the original model, the level of test analysis correlation was good. In table 6, the percentage differences in peak acceleration between the test and the analysis (original model) are shown. All values fall within ±25%, with one exception. Of course, this data only examines the peak value and does not consider the time when the peak occurs. At three of the eight locations, perfect agreement between the peak acceleration of the test and analysis was obtained. The one channel that showed poor agreement was the accelerometer located at the center of the bottom skin of the wing at FS 26. This result was not surprising, given the coarse mesh of the fuselage frames at FS 25 and FS 27, the fact that the wing attachment hardware was not accurately represented including the rotational degrees of freedom, and the fact that the nodes used in the elements forming the simulated dog bones were constrained to move in the vertical direction only. All these factors made the model too stiff, causing the analytical acceleration response to overpredict the test response. The main focus of the mesh refinement study was to rediscretize the model of the fuselage frames at FS 25 and FS 27, to include a more refined and accurate representation of the wing attachments and to eliminate nodal constraints allowing the wing to move as forces dictated. The influence of these changes was to lower the percentage difference in peak acceleration from -100% to -50% at the bottom center of the wing. Even though this margin of error for peak acceleration was still too high, it was also important to note that the refined mesh model exactly predicted the displacement response of the wing.

Table 6. Percentage Difference in Test and Analysis Peak Accelerations

Channel Description	Difference (%)
Left outer FT at FS 20	0
Right outer FT at FS 18	0
Right side cockpit floor	23.5
Left inner FT at FS 29	9.4
Right inner FT at FS 35	0
Tail section at FS 47	12
Left sidewall at FS 18	-22.7
Bottom center of the wing at FS 26	-100

FT = Floor track

A new approach for quantifying test analysis correlation needs to be developed and used. In this report, test analysis correlation is presented as a comparison of structural deformation and plots of filtered acceleration and velocity time histories. For the ATR 42 simulation, the refined mesh

model accurately predicted the maximum amount of wing vertical displacement. This example represented good correlation. For filtered acceleration time histories, the level of agreement is determined by comparing the magnitude and timing of the peak acceleration, and the pulse duration. The analyst will rarely observe good correlation between test and analysis in the sense of an absolute match for these three parameters. In general, the level of correlation is deemed good or reasonable if these parameters are within close proximity. The need to re-evaluate the current crash data analysis and correlation methodologies for use with detailed finite element model simulations is identified in reference 17. Recently, a project was initiated at NASA Langley to better quantify the accuracy of crash simulation results. The motivation for the project, as stated in reference 17 was:

> "to document modeling improvements, to evaluate design configurations analytically, and to enable certification or qualification by analysis."

Several important findings are repeated from reference 17, as follows.

> "It is necessary to quantify and understand experimental variations, channel-to-channel, for symmetric locations, as well as test-analysis variations. Future crash finite element model development could be expedited by correlation with experimental modal analysis results, especially since the modal correlation will depend on the accuracy of the global stiffness and mass distribution of the finite element model. Also, this approach provides a second set of data for correlation, which is important given that most test articles are destroyed during crash testing."

Continued work is needed to automate rigorous test analysis correlation methodologies to assess and improve the level of accuracy.

Reference 18 provides an excellent summary of a panel discussion on issues and directions of research in the areas of model updating, predictive quality of computer simulations, model validation, and uncertainty quantification. This reference raised some pertinent questions, such as what model is appropriate for what purpose, and what does it take to be predictive? The authors of reference 18 question the validity of calling a model predictive when it has been validated through comparison with a single set of test data. Such a model does not guarantee accuracy of predictions for scenarios not represented by the test data. The authors of reference 17 state:

> "It is our opinion that the focus of the research in model validation should be shifted from validating deterministic models to validating statistically accurate models."

Such an approach would account for variability in the operational and testing environments and uncertainties related to manufacturing and fabrication tolerances. Thus, model validation should be strongly coupled with uncertainty quantification. Finally, the authors of reference 18 propose five topic areas that are:

> "critical to the success of model updating, uncertainty quantification, and model validation for linear and nonlinear dynamics."

These five topic areas are (1) uncertainty quantification, (2) sampling and fast probability integration, (3) generating fast-running meta models, (4) feature extraction, and (5) statistical hypothesis testing.

8. CONCLUSIONS.

This report describes a multiyear research project to develop and validate a numerical model of a vertical drop test of a regional transport airplane, the ATR 42-300. The research project contained three major tasks: (1) perform a vertical drop test of the ATR 42 airplane to generate test data for correlation with the analytical simulation, (2) develop a finite element model of the airplane and perform an initial test analysis correlation, and (3) perform parametric assessments using the original model and evaluate model improvements, such as incorporating updated material properties and performing a mesh refinement study. The objective of the project was to validate a numerical simulation of the impact response of a regional transport airplane subjected to crash loading using a commercially available, nonlinear, explicit transient, dynamic finite element code, LS-DYNA.

On July 30, 2003, a 30-foot per second vertical drop test of the airplane was conducted using the Dynamic Drop Test Facility at the Federal Aviation Administration (FAA) William J. Hughes Technical Center, Atlantic City International Airport, New Jersey. For the test, the airplane was configured with seats, anthropomorphic test dummies, mannequins, luggage in the forward and aft compartments, and 8700 pounds (lb) of water in the wings to represent the fuel load. Total weight of the test article was 33,200 lb. A dominant feature of the airplane is the high wing, which is attached directly to two heavy fuselage frames at eight different locations, including four dog bone attachments. The airplane was instrumented with accelerometers, strain gages, load cells, pressure transducers, and string potentiometers. Data were collected at 10,000 samples per second (sec). Of the channels available, eight were chosen for correlation with the model. During the test, the wing support frames failed, allowing the wing to displace vertically into the fuselage cabin. In addition, the floor buckled and several of the seats failed.

The finite element model of the airplane was developed from direct measurements of the airframe geometry. The initial model contained 57,643 nodes and 62,979 elements, including 60,197 quadrilateral shell elements, 551 triangular shell elements, 526 beam elements, and 1,705 point elements. The point elements were used to apply concentrated mass to the model to represent ballast weight. Material properties were obtained from material handbooks. An edge-constrained contact surface was added, and an automatic contact definition was used. All nodes within the airplane model were assigned an initial velocity of 360 in. per second in the negative vertical direction. The model was executed in LS-DYNA (version 970) for a termination time of 0.25 sec, which required 130 hours of central processing unit (CPU) on a single processor

Hewlett Packard workstation. The initial analytical predictions correctly simulated the major damage mode observed during the test, which was the collapse and failure of the fuselage structure beneath the wing. These structural failures allowed the wing to displace vertically through the fuselage cabin. In general, a high level of agreement was obtained between the experimental and analytical data, especially when considering the complexity of the test article. It was particularly important to obtain accurate prediction of the floor-level acceleration responses, since these pulses are transmitted to the seat and occupants. These data will be useful in evaluating the FAA's proposed dynamic seat standards for commuter-class airplane.

Following the initial model development and test analysis correlation, a parametric study was performed to evaluate the influence of varying fuel weight on the response of the heavy fuselage frames. Three cases were executed with full-fuel loading, half-fuel loading, and no-fuel loading. Each simulation was executed for 0.25 sec. As expected, the full-fuel model exhibited the most deformation and damage of the fuselage frames and the no-fuel model showed very little deformation and damage. The maximum vertical displacement of the wing ranged from 35 in. for the full-fuel model to 12 in. for the no-fuel model. However, relatively small differences were observed in the floor-level acceleration responses for the three fuel cases.

Following the parametric study, a model improvement effort was initiated that included developing a corrected mesh model, incorporating experimentally determined material properties, performing a static and dynamic loads analyses of the wing support structure, and conducting a mesh refinement study. The development of the corrected mesh model was focused on eliminating nodal discontinuities in the model. These nodal disconnects were discovered as a result of the large number of initial penetration warnings issued by the automatic contact definition used in the model. Unfortunately, correcting these problems in the mesh created a large number of triangular elements, which are generally not recommended for explicit models because they are too stiff. As the stiffness of the model increases, higher peak accelerations and shorter pulse durations occur. Consequently, the overall level of correlation was not improved.

Another model improvement was to use experimentally determined material properties instead of handbook values. The FAA provided several pieces of the airframe structure and coupons were cut from them. Quasi-static and dynamic tests were performed to examine strain-rate effects on the material properties. Essentially, no strain-rate effects were found. In general, the Young's modulus, yield stress, hardening modulus, and failure strain were higher than handbook values used in the original model. Based on results from a National Aeronautics and Space Administration Structural Analysis (NASTRAN) of a two-fuselage frame model, changes in Young's modulus had no discernable effect. However, changes in response, due to yield stress and hardening modulus, were more pronounced.

NASTRAN and LS-DYNA simulations were performed using a refined mesh model of the two heavy fuselage frames located at frame station (FS) 25 and FS 27, including a physically accurate representation of the frame and wing attachments. This structure is the primary load-bearing structure for the high wing and fuel. The correct physical mechanisms were included in the model to allow for rotation of the wing. The NASTRAN model was executed with enforced displacements applied at the wing attachment locations. The results of this analysis showed that

the reaction forces at the dog bone attachments were considerably higher than those at the frame attachments. The NASTRAN model of the two heavy fuselage frames was converted to an LS-DYNA model. For the dynamic simulations, a rectangular block representing the wing loading was attached to the frames. Also, curved impact surfaces were added beneath the frame models at FS 25 and FS 27. The dynamic simulation showed the same location of initial plasticity as the static simulation. Also, the dynamic model accurately predicted the reaction force response generated by the static model.

As a final model improvement, the refined mesh model of the heavy fuselage frames at FS 25 and FS 27, including the physical models of the dog bone and upper attachments, was incorporated into the full airplane finite element model and a mesh refinement study was conducted. Combining the two models required considerable editing and remeshing. The final model contained 77,318 nodes, 102,788 elements, including 85,600 shell elements, 14,319 solid elements, 1,190 beam and/or rod elements, and 1,679 point-mass elements. The elements were grouped into 391 different part definitions, most of which were used to define different thicknesses in the heavy fuselage frames located at FS 25 and FS 27. The work that went into generating the final, refined mesh model of the ATR 42 airplane was rewarded with improvements in test analysis correlation. The model accurately predicted the forward rotation of the wing. Also, improved correlations with the acceleration, velocity, and displacement responses of the wing were achieved. Unfortunately, the improved correlation came at a large computational expense. The refined mesh model was executed for 0.3 sec, which required 367 hours (approximately 15 days) of CPU. The original model was executed for a termination time of 0.25 sec. The reason for the longer run time was to capture the wing displacement response. The model exactly predicted the maximum vertical displacement of the wing of 51 in. at 0.29 sec.

9. REFERENCES.

1. Noor, A. and Carden H.C., editors, “Computational Methods for Crashworthiness,” NASA Conference Publication 3223, October 1993.

2. Abramowitz, A., Smith, T.G, and Vu, T., “Vertical Drop Test of a Narrow-Body Transport Fuselage Section With a Conformable Auxiliary Fuel Tank Onboard,” FAA report DOT/FAA/AR-00/56, September 2000.

3. Abramowitz, A., Smith, T.G., Vu, T., and Zvanya, J.R., “Vertical Drop Test of a Narrow-Body Transport Fuselage Section With Overhead Stowage Bins,” FAA report DOT/FAA/AR-01/100, September 2002.

4. Anon., “MSC.Dytran User’s Manual Version 4.7,” The MacNeal-Schwendler Corporation, Los Angeles, CA, 1999.

5. Jackson, K.E. and Fasanella, E.L., “Crash Simulation of a Vertical Drop Test of a B-737 Fuselage Section with Overhead Bins and Luggage,” *Proceedings of the Third Triennial Aircraft Fire and Cabin Safety Conference*, Atlantic City, NJ, October 22-25, 2001.

6. Fasanella, E.L. and Jackson, K.E., "Crash Simulation of a Vertical Drop Test of a B-737 Fuselage Section with an Auxiliary Fuel Tank," *Proceedings of the Third Triennial Aircraft Fire and Cabin Safety Conference*, Atlantic City, NJ, October 22-25, 2001.

7. Jackson, Karen E. and Fasanella, E.L., "Crash Simulation of Vertical Drop Tests of Two Boeing 737 Fuselage Sections," FAA report DOT/FAA/AR-02/62, August 2002.

8. Anon., "MSC.PATRAN," Publication No. 903077, Version 6, The MacNeal-Schwendler Corporation, 1996.

9. Anon., "LS-DYNA Keyword User's Manual Volume I and II," Livermore Software Technology Company, Livermore, CA, March 2001.

10. Anon., "Weight and Balance Manual," Avions de Transport Regional, Service Bulletin No. ATR 42-34-0114, issued March 1992.

11. Abramowitz, A., Smith, T. G., Vu, T., and Zvanya, J. R., "Vertical Drop Test of an ATR 42-300 Airplane," FAA report DOT/FAA/AR-05/56, March 2006.

12. Jackson, K.E. and Fasanella, E.L., "Development of an LS-DYNA Model of an ATR 42-300 Aircraft for Crash Simulation," *Proceedings of the Eighth International LS-DYNA Users Conference*, Dearborn, MI, May 2-4, 2004.

13. Military Handbook 5H, U.S. Department of Defense, 1 December 1998.

14. Anon., LS-PRE/POST v. 1.0 Manual, Livermore Software Technology Company, Livermore, CA, August 27, 2002.

15. Society of Automotive Engineers, Recommended Practice: Instrumentation for Impact Test – Part 1, Electronic Instrumentation, SAE J211/1, March 1995.

16. Anon, "MSC/NASTRAN Quick Reference Guide," Version 70.5, The MacNeal-Schwendler Corporation, Los Angeles, CA, February 1998.

17. Lyle, K.H., Bark, L.W., and Jackson, K.E., "Evaluation of Test/Analysis Correlation Methods for Crash Applications," *Journal of the American Helicopter Society*, Vol. 47, No. 4, October 2002, pp. 219-232.

18. Hemez, F.M. and Doebling, S.W., "Model Validation and Uncertainty Quantification," *Proceedings of the IMAC-XIX, the 19th International Modal Analysis Conference*, Kissimmee, FL, February 5-8, 2001.